UNIVERSITY OF SOUTHAMPTON

FACULTY OF ENGINEERING AND THE ENVIRONMENT

Aeronautics, Astronautics and Computational Engineering

Aerodynamics and Flight Mechanics Research Group

A Numerical Study of Impulsively Generated Vortices between Non-Deformable Stress-Free Layers

by

Watchapon Rojanaratanangkule

Thesis for the degree of Doctor of Philosophy

May 2013

UNIVERSITY OF SOUTHAMPTON

ABSTRACT

FACULTY OF ENGINEERING AND THE ENVIRONMENT
Aeronautics, Astronautics and Computational Engineering
Aerodynamics and Flight Mechanics Research Group

Doctor of Philosophy

A NUMERICAL STUDY OF IMPULSIVELY GENERATED VORTICES BETWEEN NON-DEFORMABLE STRESS-FREE LAYERS

by Watchapon Rojanaratanangkule

A wake behind an unsteady moving submerged vehicle is of interest and importance in a broad variety of engineering disciplines, ranging from underwater to aeronautical engineering. When the vehicle changes its speed or direction, under certain conditions, it can lead to the appearance of a coherent kilometre-scale quasi-planar counter-rotating vortical structure which persists for the order of days. The aims of this work are to determine the conditions under which such a large coherent vortex can appear and to obtain deeper understanding of its dynamics by investigating the evolution of a turbulent patch created by either an impulsively accelerating axisymmetric self-propelled body or an impulsive jet in the small-scale upper ocean via direct numerical simulation.

A non-conservative body force is applied to the governing equations to represent an impulsive jet, while an accelerating motion of a self-propelled body is emulated by the combination of an immersed boundary method and the body force. Criteria for the occurrence of a vortex dipole are found to depend on a dimensionless parameter, called the confinement number. Once the confinement number is higher than about unity, the vertical growth of an impulsively generated turbulent patch is restricted by the top and bottom layers of the upper ocean leading to the formation of a vortex dipole at the free surface. The contrast and strength of a surface signature increase linearly with increasing confinement number. The late-time dynamical structures, i.e. the propagation velocity, size and the decay rate of maximum vorticity, of the dipolar eddy induced by the presence of vertical confinement can be predicted by scaling laws relevant to a stratified fluid, even though the dipole possesses a Reynolds-number dependence.

Contents

List of Figures

List of Tables

Declaration of Authorship

I, Watchapon Rojanaratanangkule, declare that the thesis entitled "*A Numerical Study of Impulsively Generated Vortices between Non-Deformable Stress-Free Layers*" and the work presented in the thesis are both my own, and have been generated by me as the result of my own original research. I confirm that:

- this work was done wholly or mainly while in candidature for a research degree at this University;
- where any part of this thesis has previously been submitted for a degree or any other qualification at this University or any other institution, this has been clearly stated;
- where I have consulted the published work of others, this is always clearly attributed;
- where I have quoted from the work of others, the source is always given. With the exception of such quotations, this thesis is entirely my own work;
- I have acknowledged all main sources of help;
- where the thesis is based on work done by myself jointly with others, I have made clear exactly what was done by others and what I have contributed myself;
- parts of this work have been published as:
  - Rojanaratanangkule, W., Thomas, T. G. & Coleman, G. N. 2011 Numerical study of turbulent manoeuvring-body wakes: Interaction with a free surface. In *7th International Symposium on Turbulence and Shear Flow Phenomena (TSFP-7)*. Ottawa, Canada.
  - Rojanaratanangkule, W., Thomas, T. G. & Coleman, G. N. 2012 Numerical study of turbulent manoeuvring-body wakes: Interaction with a non-deformable free surface. *J. Turbul.* **13** (N17), 1–22.
  - Rojanaratanangkule, W., Thomas, T. G. & Coleman, G. N. A numerical investigation of impulsively generated vortical structures in deep and shallow fluid layers, In preparation.

Signed: _____

Date: _____

Acknowledgements

First and foremost, I wish to express my sincerest thanks to my thesis supervisors, Professor Gary Coleman and Dr Glyn Thomas, for their invaluable guidance, help and support through the years. Their expertise in theoretical and computational fluid dynamics has improved my own understanding in the fields. In particular, I would like to thank Gary for giving me an opportunity to do a PhD under his supervision. Gary has always been available for consultation and has continually been the source of inspiration and enthusiasm. I would like to thank Glyn particularly for his time, patience and ability to answer and explain my questions no matter how obscure or obvious the questions are.

I would like to gratefully acknowledge Professor Sergey Voropayev of University of Notre Dame, who visited Southampton during the second year of my study, for his careful reading of my journal manuscript and many helpful suggestions. I would also like to thank him for sharing his amazing knowledge and experience of vortical flows.

This work was made possible by the benefit from the UK Engineering and Physical Sciences Research Council (EPSRC) under grant EP/G05035X, as part of the UK Turbulence Consortium (EP/G069581/1), who provided not only the financial support but also the computational time on the HECToR facilities, the UK's national high-performance computing service. I am grateful to the University of Southampton for the access to its high-performance computer, Iridis 3.

Plenty of thanks to my fellow students of vortex dynamics, Shankar Balakrishnan and Daniel Mulvaney. Many timely discussions with them were very enlightening. My office mates Alex Lau and Brian Gruncell were a constant source of humour during the long hours I spent in the office. Special thanks to all friends who made my stay in Southampton more enjoyable, especially Yusik Kim, Patrick Bechlars, Khemapat Tontiwattanakul and Woraluck Wongse-Ek.

Finally, I would like to express my heartfelt gratitude to my parents for their continuous love, support and encouragement throughout the entire period of my study, and to my brother and sister who always stand beside me.

Watchapon Rojanaratanangkule
University of Southampton
May 2013

Nomenclature

Roman Symbols

A	empirical constant for the decay rate of vertical vorticity
$\boldsymbol{B}$	boundary force vector, $\boldsymbol{B} = (B_x, B_y, B_z)$
C	confinement number, $C = J^{1/2}\Delta t_f / h^2$
C_D	drag coefficient
C_L	lateral force coefficient
Cn	contrast number
D_b	diameter of the body
E_n	azimuthal modal energies
f_i	external body force
F_K	net volume-integrated kinetic energy flux
F_M	net volume-integrated momentum flux
Fn	formation number, $Fn = \Delta t_f J^{1/2} / 2R^2 \pi^{1/2}$
f_s	shedding frequency
f_w	window function
$\widehat{G}$	low-pass filter in Fourier space
h	depth of the fluid domain
$\boldsymbol{I}$	impulse vector, $\boldsymbol{I} = (I_x, I_y, I_z)$
$\mathcal{I}$	linear interpolation operator
J	3D forcing intensity (force per unit volume)

$\tilde{J}$	2D forcing intensity (force per unit area)
K	volume-integrated kinetic energy
ℓ_y	lateral length of vortical structure
ℓ_z	vertical length of vortical structure
L_x, L_y, L_z	domain lengths in the x, y and z-directions
$\mathcal{L}$	reference length scale
M_{eff}	sum of the actual and added/virtual mass
n	modal number
N_x, N_y, N_z	number of grid cells in the x, y and z-directions
p	pressure
$\mathcal{P}_x^{\pm}, \mathcal{P}_y^{\pm}, \mathcal{P}_z^{\pm}$	boundaries of the domain in the $\pm x$, $\pm y$ and $\pm z$-directions
Q	second invariant of the velocity gradient tensor, $Q = -\frac{1}{2}\left(u_{i,j}u_{j,i}\right)$
R	radius of the disk-like body force
r	radial coordinate
$r_{1/2}$	jet/wake half-width
Re_b	Reynolds number based on the terminal/free-stream velocity and the diameter of the body, $Re_b = U_{b,t}D_b/\nu = U_\infty D_b/\nu$
Re_j	Reynolds number based on the forcing intensity, $Re_j = J^{1/2}/\nu$
Re_{ref}	reference Reynolds number, $Re_{\text{ref}} = \mathcal{U}\mathcal{L}/\nu$
S_{ij}	rate of strain tensor, $S_{ij} = (u_{i,j} + u_{j,i})/2$
St	Strouhal number
t	time
$\boldsymbol{T}$	thrust force vector, $\boldsymbol{T} = (T_x, 0, 0)$
u, v, w	Cartesian velocity components in the x, y and z-directions
u_x, u_r, u_θ	cylindrical velocity components in the x, r and θ-directions

$\bar{u}, \bar{v}, \bar{w}$	mean velocity components in the x, y and z-directions
u', v', w'	fluctuating velocity components in the x, y and z-directions
u^*	provisional velocity
u_{def}	velocity deficit
$\boldsymbol{u}_{\text{vs}}$	velocity vector at virtual body surface, $\boldsymbol{u}_{\text{vs}} = (u_{\text{vs}}, v_{\text{vs}}, w_{\text{vs}})$
U_b	velocity of the body
$U_{b,\,t}$	terminal velocity of the body
$\boldsymbol{U}_d$	dipole propagation velocity vector, $\boldsymbol{U}_d = (U_d, V_d, W_d)$
U_F	time-dependent reference-frame speed (i.e. uniform inflow velocity)
U_∞	free-stream velocity
$\mathcal{U}$	reference velocity scale
$\boldsymbol{V}_{\text{vs}}$	desired velocity vector at virtual body surface
x, y, z	Cartesian coordinates in streamwise, lateral and vertical directions
x, r, θ	cylindrical coordinates in streamwise, radial and azimuthal directions
$\boldsymbol{x}_{\text{vs}}$	vector location of virtual body surface, $\boldsymbol{x}_{\text{vs}} = (x_{\text{vs}}, y_{\text{vs}}, z_{\text{vs}})$
$\boldsymbol{X}_d$	dipole centroid vector, $\boldsymbol{X}_d = (X_d, Y_d, Z_d)$

Greek Symbols

α_n	growth rate of azimuthal modes
β_f	proportional gain of the feedback forcing
δ	boundary-layer thickness
δ_d	dipole size
δ_h	three-dimensional discrete delta function

ϵ_K	volume-integrated rate of kinetic energy dissipation
κ	wavenumber
κ_c	filter cutoff wavenumber
ν	kinematic viscosity
$\boldsymbol{\omega}$	vorticity vector, $\boldsymbol{\omega} = (\omega_x, \omega_y, \omega_z)$
$\boldsymbol{\psi}$	vector stream function, $\boldsymbol{\psi} = (\psi_x, \psi_y, \psi_z)$
ρ	density
σ	Gaussian semi-width
θ	azimuthal coordinate
φ_f	integral gain of the feedback forcing
ς	perturbation amplitude
Δt	time step
Δt_f	forcing duration
Γ	circulation
Γ_S	strength of surface eddy signature
Ω	volume-integrated enstrophy
Ω_{ij}	rate of rotation tensor, $\Omega_{ij} = (u_{i,j} - u_{j,i})/2$

Subscripts

b	body
cr	critical number
d	dipole
def	velocity deficit
D	drag
i, j, k	tensor indices

jet	jet
max	maximum value
rms	root-mean-square value
T	thrust
vs	virtual body surface

Other Symbols

$\boldsymbol{\nabla}$	gradient operator
$\boldsymbol{\nabla}\cdot$	divergence operator
$\boldsymbol{\nabla}\times$	curl operator
$\boldsymbol{\nabla}^2$	Laplace operator
$\overline{()}$	mean quantity
$\lvert() \rvert$	magnitude
$()^*$	quantity normalised by J and Δt_f
$\widehat{()}$	quantity in Fourier space

Acronyms

2D	two-**D**imensional
3D	three-**D**imensional
CFL	**C**ourant–**F**riedrichs–**L**ewy number
DNS	**D**irect **N**umerical **S**imulation
FFT	**F**ast **F**ourier **T**ransform
IB	**I**mmersed **B**oundary
LES	**L**arge **E**ddy **S**imulation
LHS	**L**eft-**H**and **S**ide
MPI	**M**essage **P**assing **I**nterface

PID	**P**roportional-**I**ntegral-**D**erivative controller
PIV	**P**article **I**mage **V**elocimetry
RHS	**R**ight-**H**and **S**ide
TDMA	**T**ri**d**iagonal **M**atrix **A**lgorithm

Chapter 1

Introduction

1.1 Motivation

Large-scale vortical structures have been a fascinating problem for engineers and physicists since they are the basic features of many turbulent flows. Some well-known examples of coherent structures found in engineering and nature are a chain of vortex rings behind an aircraft (Crow, 1970), a kilometre-scale Kármán vortex street downstream of an island (Cahalan *et al.*, 2001), and a mushroom-like vortex of an atomic bomb (Sigurdson, 1991). These organised vortical structures appear due to the momentum being transported into a fluid. Depending on the type of localised momentum sources (e.g. continuous or impulsive) and backgrounds, different formation and dynamics of coherent structures can be obtained. In this work, we focus on a large-scale turbulent vortical structure generated by a sudden horizontal acceleration of a self-propelled body in the upper ocean. This accelerating motion is frequently idealised as a finite-duration momentum source (impulsive jet) in experiments due to the simplicity of controlling the forcing intensity and forcing duration.

Even though both experimental and numerical studies of turbulent wakes behind bluff bodies have received much attention by many researchers in order to gain better understanding of their dynamics, almost all of the studies have focused on wakes behind towed or self-propelled objects moving at constant velocity. Only few studies were concerned with the physics of turbulent wakes behind manoeuvring self-propelled bodies (e.g. Voropayev *et al.*, 1999, 2007). The constant-velocity wakes can be classified into two categories based on the momentum of the flow: (i) finite-momentum, and (ii) momentumless wakes. A finite-momentum wake occurs behind a towed body that imparts momentum, equal to the drag of the body, to the wake. On the other hand, a zero-momentum wake can be observed behind a self-propelled body moving at constant velocity. A self-propelled body has to

provide enough momentum (thrust) through its jet engine/propeller to balance its drag in order to move, such that no net momentum is produced to the wake. Moreover, a self-propelled wake decays much more rapidly compared with a towed wake (Brucker & Sarkar, 2010).

A wake behind a manoeuvring body can contain the characteristics of both finite- and zero-momentum wakes at the same time. In practice, a submerged vehicle (aircraft or submarine) leaves a finite-momentum wake when it accelerates or changes direction, and a momentumless wake only when it moves at constant speed (Tennekes & Lumley, 1972). A manoeuvring-body wake is of interest because it can introduce dynamics that are absent from the constant-velocity case, especially when the wake is influenced by stable stratification or by the presence of an adjacent free surface. For example, dipolar vortices produced by the interaction of manoeuvring-body wakes with either stable background density stratification or a free surface can be observed in geophysical flows (e.g. Ahlnäs *et al.*, 1987; Sous *et al.*, 2004; Voropayev *et al.*, 1999, 2007). The practical importance of dipolar vortices is that they are very large, compared with the size of the body, and long-lived. Voropayev *et al.* (1999) estimate that a coherent kilometre-scale vortical structure that persists for the order of days can be observed behind a typical submarine manoeuvre in the ocean. Moreover, due to the self-induced motion of the dipole vortex, it can transport mass, momentum and other scalar properties such as heat and salinity.

1.2 Characteristics of a Vortex Dipole

In the past two decades, a lot of meso- and synoptic-scale (i.e. with horizontal scale $10 - 100$ and of $\mathcal{O}(1000)$ km) vortical structures, called mushroom-like currents (dipole vortices), have been observed from the satellite images of the atmosphere and the ocean surface (e.g. Fedorov & Ginsburg, 1989). For example, seventeen dipole vortices were determined in the Alaska Coastal Current by Ahlnäs *et al.* (1987). The main characteristics of a dipolar vortex are that it consists of two closely packed counter-rotating vortices (see Figure 1.1), and that its horizontal length is much larger than the vertical scale due to the vertical motion of a dipole being suppressed by a vertical force. Due to the latter reason, a vortex dipole is usually considered as a quasi-two-dimensional coherent structure.

The formation and evolution of vortex dipoles have been widely studied in a linearly stratified fluid, in which the vertical growth of a dipole is confined by the

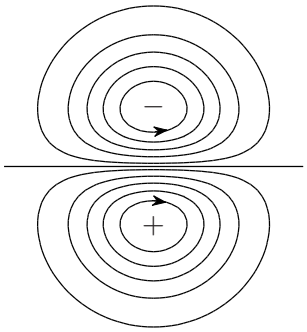

FIGURE 1.1: Schematic of a dipole vortex.

buoyancy force (e.g. van Heijst & Flór, 1989; Voropayev *et al.*, 1991; Flór & van Heijst, 1994). In those experiments, vortex dipoles were generated by injecting momentum into a fluid via an impulsive jet. Generally, when momentum is imparted into a flow, it leads to an isolated region which possesses a high concentration of vorticity and non-zero net linear momentum, often referred to as a turbulent patch (or turbulent blob). The evolution of the patch in a linearly stratified fluid is illustrated in Figure 1.2. It can be seen that, initially, the turbulent patch is fully three-dimensional (Figure 1.2a). At this stage, the patch does not feel the stratification. While the patch is propagating away from its origin, its vertical and horizontal sizes increase due to the entrainment process of the surrounding fluid as in an unbounded homogeneous fluid, where the patch can transform into a toroidal vortical structure (Maxworthy, 1977). When the kinetic energy of the patch balances the potential energy, it starts feeling the effect of stratification. Hence, the vertical growth of the patch is rapidly suppressed by the buoyancy force (Figure 1.2b). In contrast, its horizontal size is still able to expand continuously due to lateral entrainment, which leads to a quasi-planar counter-rotating dipole vortex-structure (Figures 1.2b – 1.2f). Once the formation of the dipole is complete, the dipole still translates along a straight line while preserving its shape because its net linear momentum is being conserved.

During the collapse of the turbulent patch, internal waves were also observed in some experiments. Even though the internal waves can cause the energy to radiate away from the centre of the collapse region, they decay very quickly and are believed to play no significant role in the subsequent evolution of a dipole (Voropayev *et al.*, 1991; Flór & van Heijst, 1994).

The characteristics of a vortex dipole were compared with a theoretical Lamb–Chaplygin dipole (Flór & van Heijst, 1994). It was found that a laminar-jet-induced dipole exhibits a linear relationship between the vorticity (ω) and the

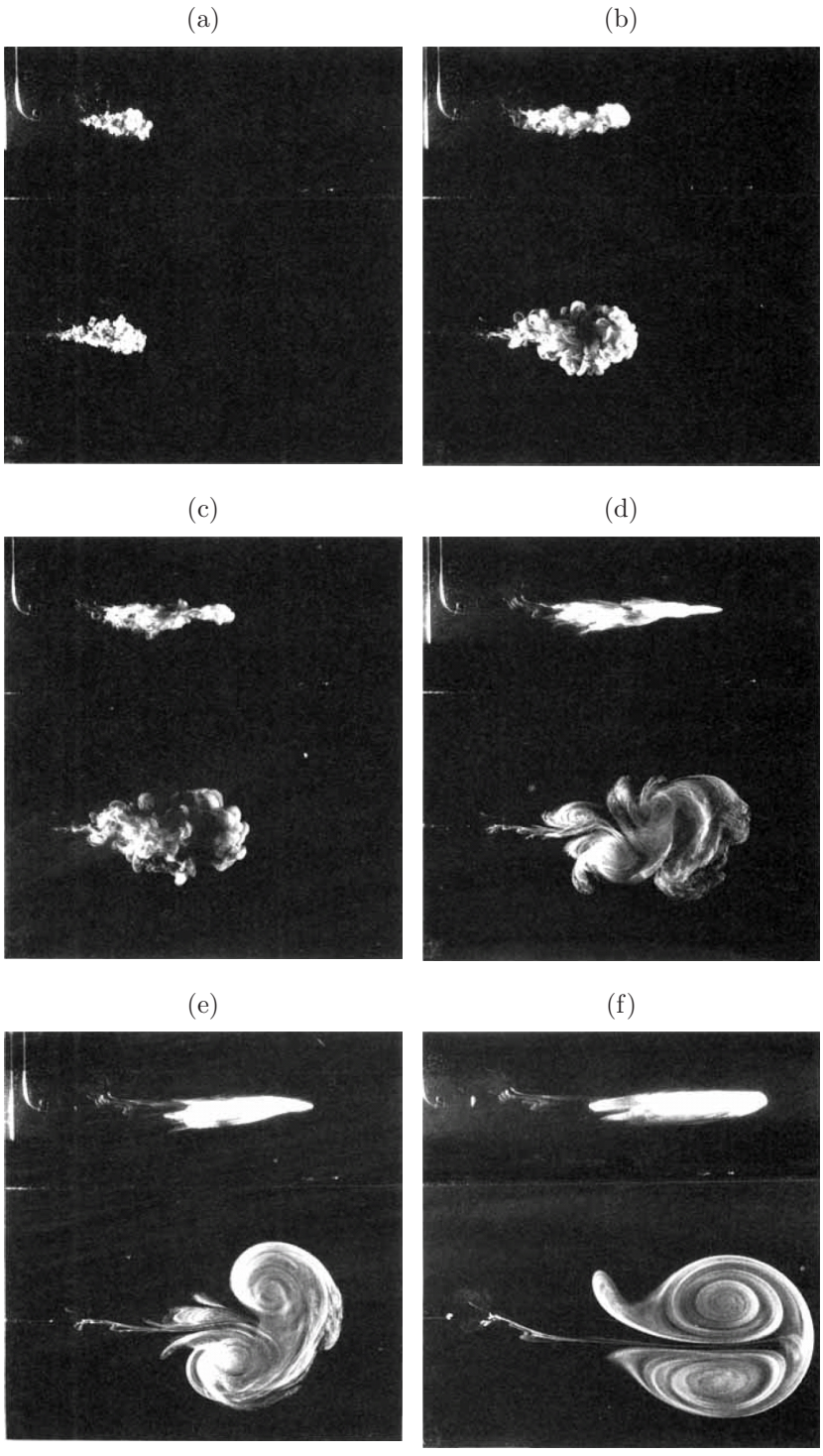

FIGURE 1.2: The evolution of a turbulent patch created by an impulsive jet in a linearly stratified fluid from Flór & van Heijst (1994). Each photograph displays side and top views (upper and lower part of the picture) of the flow.

stream function (ψ), whereas the (ω, ψ)-relationship of a dipole generated by a turbulent jet can be described by a sinh-like profile. In spite of the nonlinear (ω, ψ)-relationship, the dynamical structures (i.e. size, position of maximum vorticity, cross-sectional distributions of velocity and vorticity, and translation speed) of both laminar- and turbulent-jet-induced dipoles are in good agreement with a theoretical Lamb–Chaplygin dipole.

In order to investigate the decay of a dipole, Flór & van Heijst (1994) defined the horizontal Reynolds number $Re_h = U_d\delta_d/\nu$, based on the dipole translation velocity U_d and the dipole size δ_d (which was defined as the maximum horizontal size of the dyed fluid in the literature), and the vertical Reynolds number $Re_v = U_d H_d/\nu$ (where H_d is the dipole thickness). Soon after the dipole formation is complete, the values of these Reynolds numbers were initially $Re_h = 1000$ and $Re_v = 300$ and then decreased to $Re_h = \mathcal{O}(100)$ and $Re_v = \mathcal{O}(10)$ while the dipole was propagating along a straight line. This suggests that the vertical diffusion of vorticity and the horizontal entrainment of the surrounding fluid are the most important factors in the decay of a dipolar vortex because both physical phenomena increase the size of a dipole, whilst its translation velocity has to decrease to conserve the momentum. Flór *et al.* (1995) extended this study by comparing their experimental results with two simple theoretical models based on a viscous decaying Lamb–Chaplygin vortex. The difference between these two theoretical models is that the thickness and radius of a dipole were assumed to be constant in the first model, whilst the growth in a dipole thickness was considered in the second model. The comparisons between the experimental results and both models showed reasonable agreement although both models neglect the effect of horizontal entrainment and the decay is modelled only by the vertical diffusion of vorticity. Flór *et al.* (1995) concluded that slightly better results would be achieved by adding the effect of horizontal entrainment and that the most dominant factor for the decay of a planar dipolar vortical structure is the diffusion of the vertical vorticity.

The self-similarity of a dipolar vortex was experimentally studied by Voropayev *et al.* (1991, 2008). Using dimensional analysis with the assumption that the impulse per unit dipole thickness $P = I/H_d$ is conserved, the propagation velocity U_d and size δ_d of a dipole induced by an impulsive jet can be written in terms of t and P as $U_d \sim P^{1/3}t^{-2/3}$ and $\delta_d \sim P^{1/3}t^{1/3}$. It was noted by Voropayev *et al.* (2008) that these estimated power laws would be changed within only $\pm 10\%$, when a change in a dipole thickness is about 2 times. The evolution of the vertical vorticity can also be approximated using the same arguments. It is found

that the maximum magnitude of the vertical vorticity $\omega_{z,\max}$ is independent of P and decays only with time as $\omega_{z,\max} = At^{-1}$, where A is an empirical constant. Voropayev *et al.* (2008) determined the constant A by performing experiments in a linearly stratified fluid with a range of impulse and found that $\omega_{z,\max}$ from different I collapsed well with $A = 17$.

van Heijst & Flór (1989) performed experiments on colliding vortex dipoles in a stratified fluid in order to study the mass transfer between the vortex dipoles during their mutual interactions. In the first experiment both dipoles were set to have the same size and strength, whereas these characteristics were slightly different in the second experiment. After the dipoles collide with each other, it was observed that the dipoles exchange partners without any mass transfer between the dipoles for both cases.

The effect of background vertical shear on a dipole vortex was experimentally studied by Voropayev *et al.* (2001). Continuous and impulsive body forces were used to create a dipole vortex in a linearly stratified fluid. It was found that if the value of the background vertical shear is higher than the inverse of the forcing duration for the case of impulsive forcing or higher than the inverse of the time when the flow starts feeling the stratification for the case of continuous forcing, the dipole vortex does not form. Moreover, the lifetime of the formed dipole is shorten by the background vertical shear.

In general, it is not only the buoyancy force in a stratified fluid that can suppress the vertical motion of a turbulent patch and transform it into a quasi-two-dimensional vortical structure; it could be any kinds of vertical suppression, e.g. the magnetohydrodynamic force in a thin layer of mercury (Nguyen Duc & Sommeria, 1988), the surface tension force in a thin soap film (Couder & Basdevant, 1986), the Coriolis force in a rotating homogeneous fluid (Flierl *et al.*, 1983), or the suppression from flow geometry as in a shallow fluid (Jirka, 2001; Sous *et al.*, 2004; Voropayev *et al.*, 2007). (The vertical confinement from flow geometry is the subject of this work and will be detailed later in § 1.3.) The most important parameters that govern the characteristics of the flow are the forcing intensity J (kinematic momentum flux) and the forcing duration Δt_f (Voropayev *et al.*, 1991). Moreover, a dipole vortex can form in spite of using different types of momentum sources. For example, pancake-like vortex streets, whose characteristics are very similar to a dipole vortex, have been observed in late-time stratified wakes behind both towed and self-propelled bodies moving at constant speed; see, e.g., a comprehensive review by Lin & Pao (1979).

Voropayev *et al.* (1999) extended the complexity of the wake motion to the case of a turbulent wake created by a sudden horizontal acceleration of a self-propelled body in a stratified fluid. In their experiment, a moving force doublet was used to model the drag and the thrust generated by a manoeuvring submarine. In this method, the drag intensity J_D of a moving body can be approximated as

$$J_D = \frac{C_D S U_b^2}{2}\,, \tag{1.1}$$

where C_d is the drag coefficient, S is the area of the body and U_b is the horizontal velocity of the body. The thrust can be modelled from the jet of the body and its intensity J_T is estimated as

$$J_T = \frac{q\,(q - sU_b)}{s}\,, \tag{1.2}$$

where $q = su_{\text{jet}}$ is the volume flux of the nozzle, u_{jet} is the jet velocity and s is the area of the nozzle.

When the volume flow rate increases, the body thus accelerates resulting in an increase in the horizontal velocity of the body U_b. The Newton's second law of motion can be used to find $U_b(t)$. The balance of momentum can be written as

$$(1+k)M\frac{\mathrm{d}U_b}{\mathrm{d}t} = \rho\,(J_T - J_D)\,, \tag{1.3}$$

where $M = \rho SL$ is the mass of the body, ρ is the fluid density, L is the length of the body, and k is the virtual mass coefficient. Substituting the thrust and drag from Equations (1.1) and (1.2) into Equation (1.3), the balance of momentum becomes

$$(1+k)SL\frac{\mathrm{d}U_b}{\mathrm{d}t} = \frac{q\,(q - sU_b)}{s} - \frac{C_D S U_b^2}{2}\,. \tag{1.4}$$

Once the jet has reached its terminal speed, the volume flux q is presumably constant, thus the solution for U_b is

$$\frac{(U_b - U_1)}{(U_b - U_2)} = \left[\frac{U_0 - U_1}{U_0 - U_2}\right] \exp\left[-\left(\frac{b}{a}\right)(U_1 - U_2)\,t\right], \tag{1.5}$$

where $a = (1+k)SL$, $b = C_D S/2$, U_1 and U_2 are the real roots of the equation

$$b\tilde{U}_b^2 + q\tilde{U}_b - \frac{q^2}{s} = 0\,, \tag{1.6}$$

and U_0 is the initial velocity of the body. Let η be

$$\eta = \left[\frac{U_0 - U_1}{U_0 - U_2}\right] \exp\left[-\left(\frac{b}{a}\right)(U_1 - U_2)\, t\right] , \tag{1.7}$$

the horizontal velocity of the body can be written as

$$U_b(t) = \frac{U_1 - \eta U_2}{1 - \eta} . \tag{1.8}$$

It was observed by Voropayev *et al.* (1999) that a momentumless wake was produced behind the submarine when the submarine moved at constant speed implying that the thrust is equal to the drag. The zero-momentum wake was observed to decay rapidly without any formation of a coherent vortical structure in the late wake. In contrast, when the submarine accelerated, it left behind a finite-momentum wake which eventually transformed to a large vortex dipole.

1.3 Interaction of Momentum Sources with a Free Surface

The study of the formation and evolution of a vortex dipole has recently been extended to the case of shallow water above a solid no-slip surface, for which the vertical size of a turbulent patch is suppressed by the flow geometry (Sous *et al.*, 2004, 2005). The term *shallow layer* is defined as a layer in which the lateral size of a coherent structure is much larger than the vertical dimension of a fluid domain.

It appears that under certain conditions the vertical growth of a turbulent patch is confined by the flow geometry, leading to the formation of a quasi-planar counter-rotating vortex which produces a dipolar eddy at the free surface. Sous *et al.* (2004) studied the effect of two dimensionless parameters on the evolution of the momentum disturbance. The dimensionless parameters are the jet Reynolds number $Re_j = J^{1/2}/\nu$, and the *confinement number* C, defined as

$$C = \frac{J^{1/2}\Delta t_f}{h^2} , \tag{1.9}$$

where J is the forcing intensity, Δt_f is the forcing duration and h is the thickness of a fluid domain. The confinement number is the ratio of an impulsive force to the thickness of a fluid domain and can be interpreted as how big the vertical size of a vortical structure generated by an impulsive force is compared to the depth of the domain. (The physical meaning of the confinement number will be detailed more in § 5.1.) It was found that this condition depends only on the confinement

number, such that it can be used as a threshold for the appearance of a dipole vortex at the free surface. In Sous *et al.*'s (2004) experiment, the dipole vortex was clearly observed when $C \geqslant 2$. The dipole was still visible when $1 < C < 2$, but it was not seen when $C < 1$. The formation and evolution of the vortex dipole formed in shallow water are similar to that in a stratified fluid except that three-dimensional small-scale turbulence appears at the dipole front. Sous *et al.* (2004) stated that the vertical motion at the frontal region might appear due to the effect of bottom friction.

Voropayev *et al.* (2007) performed experiments in a two-layer fluid, where unstratified water was placed above a layer of salt water, in order to reduce the effect of the bottom surface. Their flow environment is similar to the real upper ocean (depth 50 – 100 m), in which denser water rests underneath a nominally constant density gradient. In addition, Voropayev *et al.* (2007) defined another dimensionless parameter, namely the *contrast number* Cn, to describe the intensity of a surface signature. In their experiment, the contrast number is defined as the ratio of the maximum vertical vorticity $\omega_{z,\,\max}$ of the dipole vortex to the root-mean-square (rms) value of the background vertical vorticity $\omega_{z,\,\mathrm{rms}}$, which had been measured prior to the experiments and was identical for all of their runs,

$$Cn(t) = \frac{\omega_{z,\,\max}(t)}{\omega_{z,\,\mathrm{rms}}} \,. \tag{1.10}$$

They classified the intensity of their surface signature into three regimes, which are high, significant, and insignificant, depending on the maximum value of the contrast number. The intensity of the surface signature is high when $Cn_{\max} > 50$ and in this regime the dipole is systematically formed. The dipole vortex can still be observed when $5 \leqslant Cn_{\max} \leqslant 50$, and this regime is termed significant. When $Cn_{\max} < 5$, the contrast is insignificant indicating that the dipole is hardly observed or cannot be observed at all.

The empirical relationship between the confinement number C and the contrast number Cn was also determined by Voropayev *et al.* (2007) as

$$Cn_{\max} = B\left[1 - \mathrm{e}^{2(C_0 - C)}\right] \,, \tag{1.11}$$

where the constants B and C_0 were obtained from the curve fitting of their experimental data and are $B \approx 65$, $C_0 \approx 0.65$. This phenomenological model suggests that the intensity of a surface signature increases exponentially with confinement number.

1.4 Vortical Structures Generated by Body Forces

In order to emulate the motion of a jet nozzle injecting momentum into a fluid, one can apply an external body force directly to the Navier–Stokes equations. This method can be viewed as a *generic* vortex generator, which is independent of the shape of a nozzle. It was previously used to numerically study the dynamics of vortex rings with different purposes, e.g. the interaction between a ring and a no-slip wall (Swearingen *et al.*, 1995), vortex ring pinch-off (Mohseni *et al.*, 2001), and sound radiated from a compressible turbulent ring (Ran & Colonius, 2009). In those studies, the amplitude of the body force was adjusted to obtain the desired circulation of a vortex ring. However, since it appears that the characteristics of this type of flow are subject to the initialised bulk integral momentum, one can make this approach more general by defining the impulse I of the flow via the magnitude of a body force rather than specifying the circulation. (Recall that impulse is a true conserved quantity for this type of flow and $I = J\Delta t_f$.)

A spatially localised force can also be used to generate a far wake as experimentally demonstrated by Voropayev & Smirnov (2003). In their experiment, the body force was created by a jet ejected from a nozzle moving horizontally in a stratified fluid. The force was considered as a point force because the size of the jet was negligibly small. Vortex streets were observed behind the moving point source and their characteristics were in good agreement with those appearing behind a towed body. It was concluded that the evolution and formation of such late-wake vortical structures can be described by the total momentum flux injected into the fluid and are independent of the size and shape of a particular object. Based on Voropayev & Smirnov's (2003) experiment, one can expect to emulate a far-field wake behind a towed or self-propelled body by specifying the magnitude of a localised forcing to get the desired impulse rather than the details of a blunt body. The effect of a towed object on the wake can be modelled by a force whose magnitude equals the drag and is acting in the opposite direction. Since a self-propelled body consists of two different types of forcing, a force doublet (two forces) should be used to model the thrust and the drag of the body. In general, the drag is applied in front of the thrust and these forces act in the opposite directions.

Analytical solutions that describe the steady-state velocity field of finite- and zero-momentum wakes respectively generated by a single force and a force doublet were proposed using the boundary-layer and Oseen's approximations by Smirnov & Voropayev (2003). In that study, the forcing was considered as a point force and hence represented by the Dirac delta function. On the other hand, Afanasyev

(2004) derived the time-dependent solutions for the vorticity and stream function of the point-force-induced finite- and zero-momentum wakes. The velocity field of Afanasyev's (2004) method can be obtained by differentiating the stream function equation. It was found that the velocity profiles of the finite- and zero-momentum wakes obtained from both asymptotic solutions are in close agreement with those generated by towed and self-propelled bodies.

The numerical simulation of two-dimensional finite-momentum wakes and vortex streets induced by a spatially localised force was performed by Afanasyev & Korabel (2008). A smoothly varying finite function (e.g. the Gaussian function) was used to represent the body force rather than the Dirac delta function. The Gaussian distribution was selected since it can provide the bell-like distribution similar to the electromagnetic force used in their previous experiments (Afanasyev & Korabel, 2006). Moreover, the use of the Dirac delta function (the point force) in a numerical simulation can cause some discontinuities in the flow field and cannot be accurately represented (Maxey & Patel, 2001). The stable and unstable wakes (vortex streets) similar to those observed behind a towed body were obtained in Afanasyev & Korabel's (2008) numerical experiment. The conditions under which the wake changes its regime from stable to irregular (vortex-shedding phase) were found to depend on the following flow parameters; the forcing intensity, the size of the forcing area, the free-stream velocity and the kinematic viscosity.

1.5 Objectives and Thesis Outline

When a submersible self-propelled vehicle undergoes a diving manoeuvre, it leaves behind a turbulent coherent structure which, under certain conditions, may be altered to a large long-lived pancake-like counter-rotating vortex (a dipole) and produce its signature at the water surface. Determining such conditions is of practical importance since we can indicate, for example, the possibility that a manoeuvring motion of a submarine could be detected by remote sensing. Additionally, some fundamental issues of dipole dynamics, such as self-similarity and universality of a dipole, are not well understood and remain to be learned.

This work focuses on investigating the formation and evolution of large-scale coherent structures generated from submerged impulsive momentum sources in the small-scale upper ocean mimicked by non-deformable stress-free top and bottom layers, using direct numerical simulation (DNS). An accelerating motion from rest of a self-propelled body is chosen as the momentum source and will be idealised

using an impulsive jet. The aim for this study is to determine the conditions under which the three-dimensional turbulent vortex can be altered to a quasi-two-dimensional counter-rotating structure which produces a dipolar eddy at the free surface. We will also assess how accurately the late-time behaviour of a dipole can be predicted by simple scaling laws and verify if the empirical constant for the decay rate of the vertical vorticity, A, is universal. The accuracy of the existing phenomenological model (from experimental work of Voropayev *et al.*, 2007) that measures the surface signature contrast as a function of the confinement number will also be tested.

The present work intends to compute spatially developing flows rather than the more commonly studied temporal wakes. In spite of achieving a degree of realism and generality, this leads to some rather stiff technical challenges. The computational challenges associated with this work are: (i) How to emulate an accelerating motion of a self-propelled body in a spatially evolving frame? (ii) How to capture the entire process of the dipole formation which requires a very long computational domain?

The thesis is organised as follows. The next chapter (§ 2) will introduce the governing equations and the numerical approach to solve them. In particular, the implementation of an immersed boundary method and an external body force used to emulate an accelerating motion of a self-propelled body, and the numerical techniques that allow us to investigate the entire process of the dipole formation will be detailed. The validation of these numerical tools will then separately be presented in § 3. The following chapter (§ 4) will be devoted for the late-time behaviour of dipole vortices induced by an impulsive turbulent jet and a manoeuvring-body wake. The numerical results will be compared with the dipole scaling laws. The universality of the constant A will also be verified. Finally, the physical meaning and the effect of the confinement number will be explored in § 5. The relationship between the confinement number and the intensity of a surface signature will also be determined and compared with the phenomenological model of Voropayev *et al.* (2007). Conclusions and future extension of this study will be given in § 6.

Chapter 2

Governing Equations and Numerical Method

The numerical code used in this work, CgLES, has been developed in C/C++. One of the most advanced features of this code is that it can be used to run on a large numbers of processors efficiently. In this code, the main computational domain is split into several blocks by means of a multiblock technique. Each block is then computed simultaneously on distributed memory machines architecture. Message Passing Interface (MPI) libraries are also used to transfer data between blocks located on different processors. The code has been validated (Thomas & Williams, 1997) and previously used in many applications with both Large Eddy Simulation (LES) and Direct Numerical Simulation (DNS); for example LES of vortex shedding behind an inclined cubic obstacle (Thomas & Williams, 1999), DNS of a turbulent trailing edge flow (Yao *et al.*, 2001; Thomas *et al.*, 2003), DNS of flow over groups of urban-like cubic obstacles (e.g. Coceal *et al.*, 2006, 2007; Branford *et al.*, 2011), DNS of a vortex ring (Archer *et al.*, 2008, 2010) and DNS of a breaking internal gravity wave over a two-dimensional cosine hill (Yakovenko *et al.*, 2011).

2.1 Governing Equations

Since we need to maintain the location of either an accelerating self-propelled body or a turbulent patch within the computational box, the calculations are performed in a moving reference frame. The sketches of the computational domain for a spatially developing wake and an impulsively generated turbulent patch are respectively shown in Figures 2.1 and 2.2. The non-dimensional continuity and incompressible Navier–Stokes equations in a non-inertial moving reference frame can be written in Cartesian tensor notation as

$$\frac{\partial u_i}{\partial x_i} = 0\,, \tag{2.1}$$

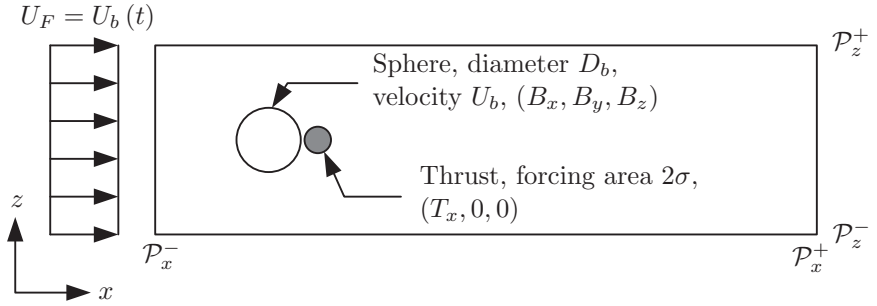

FIGURE 2.1: Schematic of geometry of a manoeuvring-body wake. The boundaries of the domain in the $\pm x_i$-direction are denoted by $\mathcal{P}_{x_i}^{\pm}$.

$$\frac{\partial u_i}{\partial t} + u_j \frac{\partial u_i}{\partial x_j} = -\frac{\partial p}{\partial x_i} + \frac{1}{Re_{\text{ref}}} \frac{\partial^2 u_i}{\partial x_j \partial x_j} - \frac{\mathrm{d}U_F}{\mathrm{d}t}\delta_{1i} + f_i\,, \tag{2.2}$$

where $x_i = (x, y, z)$ and $u_i = (u, v, w)$ are respectively Cartesian coordinates and the corresponding velocity vector in the streamwise, lateral and vertical directions, t denotes the time, p is the kinematic pressure, and δ_{ij} is the Kronecker delta. The velocity of an unsteady moving reference frame U_F (i.e. the time-dependent inflow velocity) is set equal to the velocity of the virtual (wake-generating) body U_b or the propagation velocity of the momentum patch U_d. The quantity f_i is the external body forces due to the virtual body surface $\boldsymbol{B} = (B_x, B_y, B_z)$ and/or thrust $\boldsymbol{T} = (T_x, 0, 0)$.

The non-dimensional reference Reynolds number $Re_{\text{ref}} = \mathcal{U}\mathcal{L}/\nu$ is written in terms of the reference length $\mathcal{L}$ and velocity scale $\mathcal{U}$ (which both vary from flow to flow, as illustrated below) and ν is the kinematic viscosity. In the subsequent chapters, all variables are non-dimensionalised by $\mathcal{U}$ and $\mathcal{L}$ unless otherwise stated.

2.2 Spatial and Temporal Discretisation

The Navier–Stokes equations are advanced in time with the second-order explicit Adams–Bashforth scheme. A second-order central finite-difference scheme is used to discretise the spatial derivatives on a staggered grid, where the velocity components are defined at the cell faces while the scalar quantity (pressure) is located at the cell centre. The staggered grid is employed in order to prevent any spatial oscillations in velocity and pressure fields, which may occur due to the use of the central differencing scheme.

The Adams–Bashforth scheme can be formulated as

$$u_i^{n+1} = u_i^* - \frac{3\Delta t}{2} \frac{\partial p_i^n}{\partial x_i} - (U_F^{n+1} - U_F^n)\,, \tag{2.3}$$

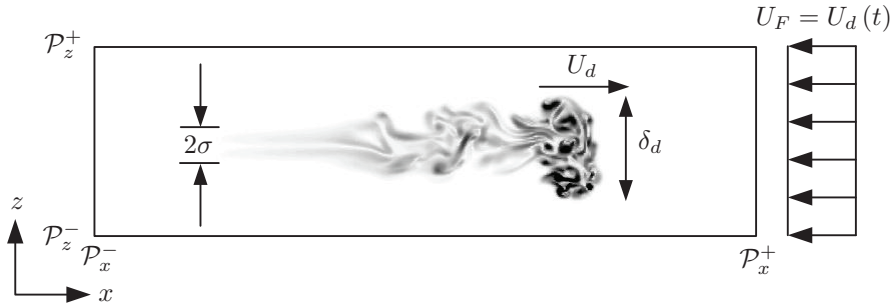

FIGURE 2.2: Schematic of computational domain for an impulsively generated turbulent patch. A non-initial moving frame of reference is attached to the patch moving in a positive x-direction with the propagation speed U_d. The quantity 2σ illustrates the size of the body force.

where the superscripts $n+1$ and n respectively denote the next and current time steps, Δt is the time step size, and the provisional velocity u_i^* is defined as

$$u_i^* = u_i^n + \frac{3\Delta t}{2} H_i^n - \frac{\Delta t}{2} H_i^{n-1} + \frac{3\Delta t}{2} f_i^n - \frac{\Delta t}{2} f_i^{n-1} + \frac{\Delta t}{2} \frac{\partial p_i^{n-1}}{\partial x_i}\,, \tag{2.4}$$

where the quantity H_i, containing the convective and viscous terms in Equation (2.2), is defined as

$$H_i = \nu \frac{\partial^2 u_i}{\partial x_j \partial x_j} - u_j \frac{\partial u_i}{\partial x_j}\,. \tag{2.5}$$

Note that since the Adams–Bashforth scheme is a multiple-step method and is not a self-starting method, an explicit Euler method is used to start the calculation for the first time step. The velocity of the moving reference frame U_F in Equation (2.3) is determined explicitly via either Equation (2.22) (for a manoeuvring self-propelled body) or Equation (2.32) (for a co-moving frame attached to a vortex).

To determine the pressure at the current time step, a Poisson equation for the pressure is constructed by taking the divergence of Equation (2.3) and then using the divergence-free condition from the continuity equation (Equation 2.1). The resulting Poisson equation for the pressure is in the form

$$\frac{\partial^2 p^n}{\partial x_i^2} = \frac{2}{3\Delta t} \frac{\partial u_i^*}{\partial x_i}\,. \tag{2.6}$$

In general, Equation (2.6) can be solved when the pressure at the boundaries is prescribed (i.e. using a Dirichlet condition). If the pressure at the boundaries is not provided, the Poisson solver used will enforce a Neumann condition for the pressure equation, i.e. $\boldsymbol{\nabla} p \cdot \hat{\boldsymbol{n}} = 0$, where $\hat{\boldsymbol{n}}$ is the unit normal vector. To make the

solution of the Poisson equation with the Neumann conditions on all boundaries unique, the pressure is defined to within an arbitrary constant. Since the iterative process conserves the constant, the iteration is started with a normalised pressure whose average is zero to make this property persist during the iteration.

2.3 Numerical Procedure

In order to find the velocity field at the next $(n+1)$ time step, the provisional velocity u_i^* is first calculated via Equation (2.4) to create the source term for the Poisson equation (RHS of Equation 2.6). After that, the Poisson equation (2.6) is solved using a *parallel* multigrid algorithm to obtain the pressure field at the current time step (Thomas & Williams, 1997). Finally, the velocity field at the next $(n+1)$ time step can be obtained by substituting the provisional velocity and the gradient of the pressure field into Equation (2.3).

2.4 Immersed Boundary Method

In order to embed an axisymmetric body into a computational grid, an immersed boundary (IB) technique is employed. This approach was first proposed by Peskin (1972), who did a two-dimensional simulation of the blood flow in a human heart valve at a very low Reynolds number. The concept of an IB method is to add an extra force, called the 'boundary force' $\boldsymbol{B} = (B_x, B_y, B_z)$, to the Navier–Stokes equations in order to emulate the effect of a virtual object on the surrounding fluid. The most advanced feature of an IB method is that the simulation of flow over complex geometries can be carried out in a Cartesian grid, in which the computational cost is much cheaper than using a body-fitted or an unstructured mesh. In the original IB approach of Peskin (1972), an immersed elastic body was mimicked by a set of virtual surface (*Lagrangian*) points moving in the fixed computational (*Eulerian*) points. The boundary force was directly computed at the Lagrangian markers using Hooke's law (the spring force) and was then distributed to the Eulerian points via a discrete delta function (Peskin, 1972).

Goldstein *et al.* (1993) extended an IB technique to the case of flow over a rigid body by applying the concept of a proportional-integral (PI) feedback control to determine the boundary force. This type of the IB method is often referred to as a 'feedback forcing approach'. Goldstein *et al.* (1993) implemented

the feedback forcing approach into a pseudo-spectral solver to compute a two-dimensional startup flow past a circular cylinder and to perform DNS of a three-dimensional turbulent channel flow. In their simulations, the location of the virtual surface points was set to coincide with the computational points and a narrow Gaussian distribution was used to blur the location of the immersed (virtual) boundary in order to generate a smooth surface. Goldstein *et al.* (1993) observed spurious oscillations caused by the discontinuity of the boundary force in a spectral representation of a flow field when the forcing was not applied over several (3–4) computational points across an immersed boundary. In fact, it was demonstrated that the use of a finite-difference scheme can avoid the appearance of the spurious oscillations although the boundary force was spread to the Eulerian points by using an area-weighted average function (Saiki & Biringen, 1996). The feedback forcing approach contains two free parameters, which are the proportional and integral gains, that need to be adjusted and these parameters are flow dependent. When computing unsteady flows, the magnitude of the gains must be large enough to drive the boundary force to respond correctly to the changing flow field. The major drawback of the feedback forcing approach is that large values of the proportional and integral gains make the discrete-time Navier–Stokes equations stiff, leading to the severe restriction on the computational time step.

To avoid the restriction on the time step size, Mohd-Yusof (1997) introduced an alternative way to determine the boundary force, called a 'direct forcing approach', for a pseudo-spectral scheme. This approach was later extended to the context of a finite-difference method by Fadlun *et al.* (2000). The concept of the direct forcing approach is that the boundary force is directly computed from the discrete-time Navier–Stokes equations, which can be written as

$$\frac{\boldsymbol{u}_{\mathrm{vs}}^{n+1} - \boldsymbol{u}_{\mathrm{vs}}^{n}}{\Delta t} = \mathrm{RHS}_{\mathrm{vs}} + \boldsymbol{B}_{\mathrm{vs}}\,, \tag{2.7}$$

where RHS regroups the convective, viscous and pressure gradient terms and the subscript 'vs' represents the variables at the virtual boundary surface. Assuming that a Dirichlet boundary condition is used and $\boldsymbol{V}_{\mathrm{vs}}$ is the desired velocity at the virtual body surface, we can simply set $\boldsymbol{u}_{\mathrm{vs}}^{n+1} = \boldsymbol{V}_{\mathrm{vs}}$ to impose the boundary condition on the immersed boundary. Thus the forcing term can be obtained by

$$\boldsymbol{B}_{\mathrm{vs}} = \frac{\boldsymbol{V}_{\mathrm{vs}} - \boldsymbol{u}_{\mathrm{vs}}^{n}}{\Delta t} - \mathrm{RHS}_{\mathrm{vs}}\,. \tag{2.8}$$

In the initial works of the direct forcing approach (see, e.g., Fadlun *et al.*,

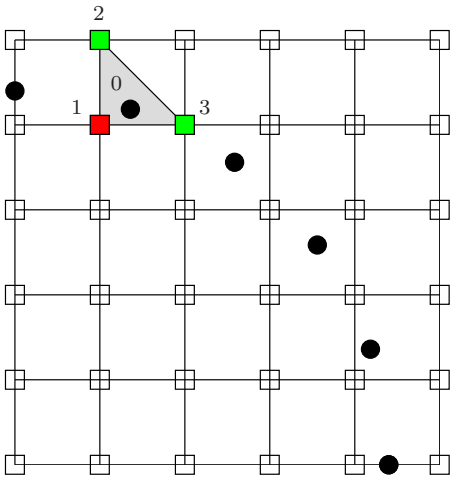

FIGURE 2.3: Schematic of the IB method showing the locations of the Lagrangian markers (●) and the computational points (□).

2000; Kim *et al.*, 2001), the boundary force at the Lagrangian points was never computed. The effect of a virtual body was represented by reconstructing the velocity field of the computational points immediately inside the interface of the virtual body via interpolation procedures. For example, the velocity field at point 1 in Figure 2.3 is obtained from the values of points 2 and 3 (exterior to the virtual surface) together with the wall value (point 0) using linear interpolation. The comprehensive reviews of the boundary reconstruction and the IB method are given by Iaccarino & Verzicco (2003) and Mittal & Iaccarino (2005).

However, it was shown by Uhlmann (2003) that the use of an interpolation procedure to obtain the velocity field at the computational points can lead to unphysical force oscillations when computing flow past a moving body. This problem led to a new procedure of the direct forcing scheme, described as follows. The boundary force is first calculated at the Lagrangian points via Equation (2.8), and are then spread to the Eulerian markers using a discrete delta function (e.g. Uhlmann, 2005; Yang *et al.*, 2009; Pinelli *et al.*, 2010).

The IB approach used in this work is based on the concept of the feedback forcing scheme of Goldstein *et al.* (1993). The major difference between our approach and Goldstein *et al.* (1993) is that we mimic a virtual body by a set of Lagrangian (virtual surface) points that do not coincide with the computational points as shown in Figure 2.3. The magnitude of the Lagrangian grid spacing $|\Delta \boldsymbol{x}_{\mathrm{vs}}|$ is set approximately equal to the grid spacing of the computational points $\Delta \boldsymbol{x}$. A discrete delta function is used to spread the effect of the virtual body to the neighbouring Eulerian points. Since the boundary force $\boldsymbol{B}$ is determined directly at the virtual surface points, the velocity field needs to be interpolated to

the immersed boundary

$$\boldsymbol{u}_{\mathrm{vs}} = \mathcal{I}\left(\boldsymbol{u}\right) , \tag{2.9}$$

where the interpolation operator $\mathcal{I}$ is the linear interpolation.

The values of $\boldsymbol{u}_{\mathrm{vs}}$ are used to compute the boundary force that restores the desired boundary values $\boldsymbol{V}_{\mathrm{vs}}$ on the virtual boundary surface via a proportional-integral (PI) feedback controller as

$$\boldsymbol{B}_{\mathrm{vs}}\left(t\right) = \varphi_f \int_0^t \left[\boldsymbol{u}_{\mathrm{vs}}\left(t\right) - \boldsymbol{V}_{\mathrm{vs}}\left(t\right)\right] \mathrm{d}t + \beta_f [\boldsymbol{u}_{\mathrm{vs}}\left(t\right) - \boldsymbol{V}_{\mathrm{vs}}\left(t\right)] , \tag{2.10}$$

where φ_f and β_f are respectively the integral and the proportional gains and are negative constants. In this work, the integral term is simply approximated as a Riemann sum, viz.

$$\int_0^t \left(\boldsymbol{u}_{\mathrm{vs}} - \boldsymbol{V}_{\mathrm{vs}}\right) \mathrm{d}t = \sum_{i=1}^{N_t} \left(\boldsymbol{u}_{\mathrm{vs}} - \boldsymbol{V}_{\mathrm{vs}}\right) \Delta t , \tag{2.11}$$

where Δt is the time step size and N_t is the total number of steps.

The boundary force is then distributed to the Eulerian points by using a three-dimensional discrete delta function δ_h

$$\boldsymbol{B} = \sum_{i=1}^{N_{\mathcal{L}}} \delta_h \left(\mathbf{x} - \mathbf{x}_{\mathrm{vs}}\right) \boldsymbol{B}_{\mathrm{vs}} \, \Delta \mathbb{V}_{\mathrm{vs}} , \tag{2.12}$$

where $N_{\mathcal{L}}$ is the total number of Lagrangian markers and $\Delta \mathbb{V}_{\mathrm{vs}} = \Delta x_{\mathrm{vs}} \Delta y_{\mathrm{vs}} \Delta z_{\mathrm{vs}}$.

In general, the three-dimensional discrete delta function can be constructed by a product of one-dimensional discrete delta functions Φ in the following manner

$$\delta_h \left(\boldsymbol{x} - \boldsymbol{x}_{\mathrm{vs}}\right) = \frac{1}{\Delta \mathbb{V}} \Phi \left(\frac{x - x_{\mathrm{vs}}}{\Delta x}\right) \Phi \left(\frac{y - y_{\mathrm{vs}}}{\Delta y}\right) \Phi \left(\frac{z - z_{\mathrm{vs}}}{\Delta z}\right) , \tag{2.13}$$

where $\Delta \mathbb{V} = \Delta x \Delta y \Delta z$. A three-point discrete delta function, which involves only three grid points in each coordinate direction, proposed by Roma *et al.* (1999) as

$$\Phi\left(r\right) = \begin{cases} \frac{1}{3}\left(1 + \sqrt{-3r^2 + 1}\right) , & |r| \leq 0.5 , \\ \frac{1}{6}\left(5 - 3\left|r\right| - \sqrt{-3\left(1 - \left|r\right|\right)^2 + 1}\right) , & 0.5 \leq |r| \leq 1.5 , \\ 0 , & 1.5 \leq |r| , \end{cases} \tag{2.14}$$

is used throughout this work. An extensive review on the construction of a discrete delta function is available in Peskin (2002).

As mentioned earlier that computing the boundary force by means of the PI controller can influence the stability of the discrete-time Navier–Stokes equations (the example of the stability issue of the PI controller will be shown in § 3.2.1), we simply remedy this issue by neglecting the integral term in Equation (2.10). Hence the boundary force is determined via a proportional controller as

$$\boldsymbol{B}_{\mathrm{vs}}(t) = \beta_f \left[\boldsymbol{u}_{\mathrm{vs}}(t) - \boldsymbol{V}_{\mathrm{vs}}(t)\right] . \tag{2.15}$$

The proportional gain β_f is chosen equal to the inverse of the time step size Δt, to obtain the maximum gain while maintaining the stability. Note that this choice of the proportional gain ($\beta_f = -1/\Delta t$) makes Equation (2.15) equivalent to the direct forcing approach (Equation 2.8) except that the term $\mathrm{RHS}_{\mathrm{vs}}$ is not included.

2.5 Boundary Conditions

To study the evolution of a submerged momentum source induced by an accelerating motion of a self-propelled body in the small-scale upper ocean, inflow and outflow boundary conditions are employed in the streamwise direction. The body moves from right to left (see Figure 2.1), such that the inflow plane is at $x = \mathcal{P}_x^-$ and the exit plane is at $x = \mathcal{P}_x^+$. At the inflow plane, Dirichlet boundary conditions are used as follows

$$u|_{\mathcal{P}_x^-} = U_F = U_b(t) , \qquad v|_{\mathcal{P}_x^-} = w|_{\mathcal{P}_x^-} = 0 . \tag{2.16}$$

The exit boundary condition is a zero gradient condition written as

$$\left.\frac{\partial u_i}{\partial x}\right|_{\mathcal{P}_x^+} = 0 . \tag{2.17}$$

The body is placed midway between an idealised thermocline and a free surface. Stress-free boundary conditions are specified at the top and bottom as an idealisation of the non-deformable free surface and the top of a region of a stratified fluid. The velocities at the no-stress surfaces are

$$w|_{\mathcal{P}_z^\pm} = 0 , \qquad \left.\frac{\partial u}{\partial z}\right|_{\mathcal{P}_z^\pm} = \left.\frac{\partial v}{\partial z}\right|_{\mathcal{P}_z^\pm} = 0 . \tag{2.18}$$

In the lateral direction (y), periodic boundary conditions are specified.

2.6 Emulation of an Accelerating Self-Propelled Body

We emulate a self-propelled body manoeuvre by imposing a thrust $f_i = T_i = T_x\delta_{1i}$, which is modelled as a jet from the body, as illustrated in Figure 2.1. The intensity of the thrust is estimated as

$$J_T = u_{\text{jet}} sN \left[u_{\text{jet}} - U_b(t)\right] , \tag{2.19}$$

where u_{jet} is the jet velocity, s is the area of the nozzle, and N is a free parameter used to adjust the jet Reynolds number and the confinement number. A three-dimensional Gaussian function is used to distribute the intensity of the thrust to the computational grids as

$$T_x = \frac{J_T}{\left(\sigma^2\pi\right)^{3/2}} \exp\left[-\frac{(x-x_0)^2 + (y-y_0)^2 + (z-z_0)^2}{\sigma^2}\right] , \tag{2.20}$$

where σ is the Gaussian semi-width, and x_0, y_0, z_0 are the centre of the thrust. Note that Equation (2.20) is determined such that J_T is associated with the total integrated force, not its maximum. The velocity of the body can be found via the balance of momentum between a manoeuvring object and the total force acting on the fluid, with

$$M_{\text{eff}} \frac{\mathrm{d}U_b}{\mathrm{d}t} = \rho \left(J_T - J_D\right) , \tag{2.21}$$

where M_{eff} is the sum of the actual and added/virtual mass, ρ is the fluid density (taken to be constant) and J_D is the intensity of the drag, which can be calculated from the volume integral of the streamwise boundary force B_x. An explicit Euler method is used to update $U_b(t)$ at every time step, viz.

$$U_b^{n+1} = U_b^n + \frac{\rho \Delta t}{M_{\text{eff}}} \left(J_T - J_D\right) . \tag{2.22}$$

2.7 Domain Resizing

Since the length scale of the flow of interest increases with time while its Reynolds number decreases, the computational box and the grid spacing need to be resized in order to effectively capture the largest and smallest scales of the flow. During the domain-resizing process, some parts of the flow are allowed to be omitted, i.e. a portion of a near-field momentumless wake or the wake shed from a vortex, because they are assumed to have negligible effect on the development of a momentum patch. To avoid any discontinuity of the flow field in a new domain especially in

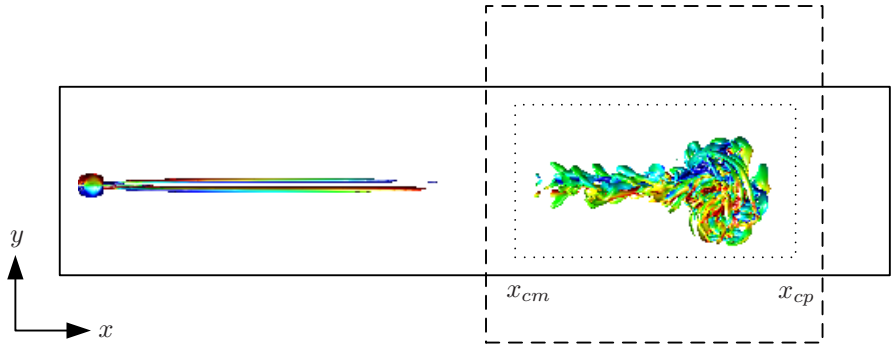

FIGURE 2.4: Schematic of domain resizing: —— old domain; ---- new domain; ····· window function f_w.

the clipping region and the edge of an old computational box (see Figure 2.4), we project the vorticity field to a new computational domain rather than the velocity field since vorticity has a finite extent. A window function f_w is also introduced in order to smoothly decay the last few planes of vorticity in an old domain to be zero in a new domain. It is defined as

$$f_w\left(x,y\right) = g_w(x)h_w(y)\,, \tag{2.23}$$

where the streamwise $g_w(x)$ and lateral $h_w(y)$ windowing functions are defined as

$$g_w(x) = \frac{1}{2}\left\{\left[\tanh\left(\sigma_w\left(x - x_{cm}\right)\right) + 1\right] - \left[\tanh\left(\sigma_w\left(x - x_{cp}\right)\right) + 1\right]\right\}\,, \tag{2.24a}$$

$$h_w(y) = \frac{1}{2}\left[\tanh\left(\sigma_w\left(l_y/2 - |y|\right)\right) + 1\right]\,, \tag{2.24b}$$

and σ_w is a smoothing coefficient, x_{cm} and x_{cp} are respectively the cutoff positions (see Figure 2.4), and l_y controls the lateral length of the window function.

The new velocity field is obtained via a vorticity–vector stream function (often called vector potential) method (see, e.g., Richardson & Cornish, 1977; Tutty, 1986; E & Liu, 1997). The Poisson equation for the vector stream function $\boldsymbol{\psi} = (\psi_x, \psi_y, \psi_z)$ whose source term is the projected vorticity vector $\boldsymbol{\omega} = (\omega_x, \omega_y, \omega_z)$ can be constructed as follows. Using Helmholtz's theorem, we first decompose the velocity vector $\boldsymbol{u} = (u, v, w)$ into a vector stream function (divergence-free component) and a scalar potential ϕ (curl-free component) (Saffman, 1995), viz.

$$\boldsymbol{u} = \boldsymbol{\nabla} \times \boldsymbol{\psi} + \boldsymbol{\nabla}\phi\,. \tag{2.25}$$

Taking the curl of Equation (2.25) and using $\boldsymbol{\nabla} \cdot \boldsymbol{\psi} = 0$ (the verification of this condition can be seen in Saffman, 1995), we then achieve the Poisson equation

$$\boldsymbol{\nabla}^2 \boldsymbol{\psi} = -\boldsymbol{\omega} \,. \tag{2.26}$$

Recall that $\boldsymbol{\omega} = \boldsymbol{\nabla} \times \boldsymbol{u}$. If there is no potential flow (no flow through boundary of the domain), $\boldsymbol{\nabla}\phi = 0$ (Richardson & Cornish, 1977). The new velocity field can then be obtained from

$$\boldsymbol{u} = \boldsymbol{\nabla} \times \boldsymbol{\psi} \,. \tag{2.27}$$

In this work, a Fourier series is used to solve Equation (2.26) in the streamwise and lateral directions, while a second-order central finite-difference scheme is employed in the vertical direction since it cannot be treated as periodic (recall that stress-free boundary conditions are being employed in this direction). Equation (2.26) thus becomes

$$\widehat{\boldsymbol{\psi}}_{k-1} + \left(-\kappa_x^2 \Delta z^2 - \kappa_y^2 \Delta z^2 - 2\right) \widehat{\boldsymbol{\psi}}_k + \widehat{\boldsymbol{\psi}}_{k+1} = -\Delta z^2 \widehat{\boldsymbol{\omega}}_k \,, \tag{2.28}$$

where $\widehat{\boldsymbol{\psi}}\left(\kappa_x, \kappa_y, z\right)$ and $\widehat{\boldsymbol{\omega}}\left(\kappa_x, \kappa_y, z\right)$ are respectively the vector stream function and vorticity vector in Fourier space, κ_x and κ_y are respectively the streamwise and lateral wavenumbers, and the subscripts k, $k-1$ and $k+1$ denote grid points in the vertical direction. At each wavenumber, $\widehat{\boldsymbol{\psi}}$ at every vertical grid node is solved simultaneously using the Tridiagonal Matrix Algorithm (TDMA) (e.g. see Ferziger & Perić, 2002; Press *et al.*, 2007). A set of boundary conditions that represent a stress-free condition (cf. Equation 2.18) for $\boldsymbol{\psi}$ is given by Hirasaki (1967) as

$$\psi_x|_{\mathcal{P}_z^\pm} = \psi_y|_{\mathcal{P}_z^\pm} = \left.\frac{\partial \psi_z}{\partial z}\right|_{\mathcal{P}_z^\pm} = 0 \,. \tag{2.29}$$

2.8 Moving Reference Frame Attached to a Vortex

Since the momentum patch moves from left to right as displayed in Figure 2.2, the inflow boundary of a co-moving frame of reference attached to the momentum patch is at $x = \mathcal{P}_x^+$, while the outflow boundary is at $x = \mathcal{P}_x^-$. The time-dependent uniform inflow velocity, adjusted to be equivalent to a propagation speed of the patch U_d via a simple control algorithm, is employed at the inflow plane, viz.

$$u|_{\mathcal{P}_x^+} = -U_F(t) \,, \tag{2.30}$$

to keep the patch at the fixed streamwise position. Additionally, the vorticity field at the inflow plane is set to zero to avoid introducing any spurious vorticity into the domain, we thus specify Neumann conditions to the other two velocity components as

$$\left.\frac{\partial v}{\partial x}\right|_{\mathcal{P}_x^+} = \left.\frac{\partial w}{\partial x}\right|_{\mathcal{P}_x^+} = 0\,. \tag{2.31}$$

At the outflow plane ($x = \mathcal{P}_x^-$), a zero gradient condition is applied as given earlier in Equation (2.17).

The time-dependent reference-frame speed U_F that minimises the difference between the streamwise position of the patch $X_d(t)$ (cf. Equation 4.2) and the target location X_c, $\varepsilon = X_d(t) - X_c$, is determined via a proportional-integral (PI) controller,

$$U_F(t) = c_1\varepsilon + c_2^2 \int_0^t \varepsilon \,\mathrm{d}t\,, \tag{2.32}$$

where c_1 and c_2 are respectively the proportional and integral gains that control the damping and oscillation time scales (cf. Archer *et al.*, 2008). The constant c_1 is chosen to give a critically damped response, such that $c_1 = 2c_2$. The integral term is approximated via the trapezoidal rule,

$$\int_0^t \varepsilon \,\mathrm{d}t = \frac{\Delta t}{2} \sum_{i=1}^{N_t} \left(\varepsilon^n + \varepsilon^{n-1}\right), \tag{2.33}$$

where the superscripts n and $n-1$ respectively denote the current and previous time steps, Δt is the time step size and N_t is the total number of step.

Chapter 3

Validation for Generating a Virtual Body and Numerical Strategies

This chapter presents the validation of two new features added to CgLES, which are an external body force that is to generate an impulsive momentum source and an immersed boundary method used to embed a virtual body. Additionally, the accuracy of the numerical strategies (i.e. the domain-resizing technique and the moving reference frame attached to a vortex) is presented. The external body force is validated by calculating two-dimensional finite- and zero-momentum wakes as given in § 3.1, while flow past a sphere is computed to test the ability of the immersed boundary method as shown in § 3.2. The correctness of the numerical approach used to adjust the size of the computational domain is presented in § 3.3, while the proportional-integral controller that computes the speed of the moving frame of reference attached to a vortical structure is tested in § 3.4. Finally, the summary and conclusions of the validation are offered in § 3.5.

3.1 Generate a Virtual Body using Single and Doublet Forces

For a purpose of validation, single and doublet forces were used to create 2D finite- and zero-momentum wakes since there exist experimental and numerical works of Afanasyev & Korabel (2006, 2008), who used single and doublet forces to generate the wakes with various input momentum flux. Afanasyev & Korabel (2006) performed a set of experiments to study towed and self-propelled wakes induced by an electromagnetic force in a stratified fluid. The main role of the stratification is to generate a two-dimensional vortical structure, i.e. a vortex street. They observed that the behaviour of the wakes induced by the localised forces depends on four quantities, which are the forcing intensity, the size of the forcing area, the free-stream velocity U_∞ and the kinematic viscosity ν. These quantities were

grouped together in terms of two dimensionless parameters as

$$\Pi_\nu = \frac{\tilde{J}}{\nu U_\infty}\,, \tag{3.1}$$

$$\Pi_a = \frac{\tilde{J}}{\sigma U_\infty^2}\,, \tag{3.2}$$

where σ is the Gaussian semi-width and $\tilde{J}$ is the 2D forcing intensity equal to the forcing intensity of the thrust or the drag. The parameter Π_ν can be considered as an analogue of a Reynolds number, whilst Π_a can be interpreted as the ratio of the momentum flux transported by the forcing to the momentum flux delivered by the velocity of the fluid through the forcing area.

This section is started by introducing the asymptotic solutions of plane wakes behind point single/doublet forces in § 3.1.1, followed in § 3.1.2 by the implementation of single and doublet forces. The results compared with the theoretical solutions and the data of Afanasyev & Korabel (2006, 2008) are then reported in § 3.1.3 and § 3.1.4.

3.1.1 Asymptotic Solutions

Full details of deriving the analytical solutions of 2D finite- and zero-momentum wakes created by a point momentum source are given by Smirnov & Voropayev (2003) and Afanasyev (2004). Smirnov & Voropayev (2003) derived the steady-state solutions of the streamwise velocity deficit based on the boundary-layer and Oseen's approximations, whilst the time-dependent solutions of the vorticity ω and the stream function ψ of the towed and self-propelled wakes are proposed by Afanasyev (2004). In this work, we follow the asymptotic solutions of Afanasyev (2004) because they can provide not only the streamwise velocity but also the vertical velocity.

Afanasyev (2004) obtained the solutions of the vorticity and stream function of the wakes behind single/doublet point forces acting continuously in time by integrating the solutions of those induced by the impulsive forces as

$$\begin{bmatrix}\omega_{J,Q}\\ \psi_{J,Q}\end{bmatrix}(x,y,t) = \int_0^t \begin{bmatrix}\omega_{I,M}\\ \psi_{I,M}\end{bmatrix}[x - U_\infty\tau, y, \tau]\,\mathrm{d}\tau\,, \tag{3.3}$$

where the subscript I (or M) represents an impulsive single (or doublet) force, and the subscript J (or Q) denotes a continuous single (or doublet) force. The

vorticity and the stream function of a plane (2D) wake induced by an impulsive point force can be obtained from Stokes' approximation (Cantwell, 1986),

$$\omega_I(x,y,t) = \frac{\tilde{I}y}{8\pi(\nu t)^2} e^{-\xi^2}, \tag{3.4}$$

$$\psi_I(x,y,t) = \frac{\tilde{I}y}{2\pi(x^2+y^2)} \left(1 - e^{-\xi^2}\right), \tag{3.5}$$

where $\tilde{I}$ is the 2D impulse ($[\tilde{I}] = L^3T^{-1}$), L and T are respectively units of length and time, ν is the kinematic viscosity and $\xi^2 = (x^2+y^2)/4\nu t$. Substituting Equations (3.4) and (3.5) into Equation (3.3) will change the type of the forcing from impulsive to continuous and the steady-state solutions can be obtained by letting $t \to \infty$

$$\omega_J(x,y) = \frac{\tilde{J}U_\infty}{4\pi\nu^2} \frac{y}{(x^2+y^2)^{1/2}} \exp\left(\frac{xU_\infty}{2\nu}\right) K_1\left(\frac{U_\infty}{2\nu}\sqrt{x^2+y^2}\right), \tag{3.6}$$

$$\psi_J(x,y) = \frac{\tilde{J}y}{2\pi} \int_0^\infty \frac{1 - e^{-\vartheta^2}}{(x - U_\infty\tau)^2 + y^2} \mathrm{d}\tau, \tag{3.7}$$

where $\tilde{J}$ is the 2D forcing intensity of the continuous single force ($[\tilde{J}] = L^3T^{-2}$), $\vartheta^2 = \left[(x - U_\infty\tau)^2 + y^2\right]/4\nu\tau$ and $K_n(x)$ is a modified Bessel function of the second kind. Let $u_{\mathrm{def}} = U_\infty - u$ be the streamwise velocity deficit. Using the Oseen's approximation, i.e. $u_{\mathrm{def}}/U_\infty \ll 1$, and the differentiation of the stream function with respect to y, $u_{\mathrm{def}} = \partial\psi/\partial y$, the distribution of the streamwise velocity deficit of a finite-momentum wake generated by a point force along its axis can be obtained as

$$u_{\mathrm{def}}(x,0) = \frac{\tilde{J}}{2\pi} \int_0^\infty \frac{1 - e^{-\varkappa^2}}{(x - U_\infty\tau)^2} \mathrm{d}\tau, \tag{3.8}$$

where $\varkappa^2 = \left[(x - U_\infty\tau)^2\right]/4\nu\tau$.

The asymptotic solution of a momentumless wake induced by a point force doublet can be obtained by the same manner and will be described as follows. The vorticity field of the wake generated by two forces can simply be obtained by the sum of the vorticity of each force. Assuming that both forces are separated by distance ϵ and act in the opposite directions with the same magnitude, the vorticity field is then given by

$$\omega_M(x,y,t) = \omega_I(x,y,t) - \omega_I(x-\epsilon,y,t). \tag{3.9}$$

One may use a standard limiting procedure to obtain the forcing intensity of an impulsive force doublet M (Afanasyev, 2004), as

$$M = \lim_{\substack{\epsilon \to 0 \\ I \to \infty}} I\epsilon \,. \tag{3.10}$$

The vorticity and the stream function of the wake induced by an impulsive force doublet are also given by Afanasyev (2004) as

$$\omega_M\left(x, y, t\right) = -\frac{\tilde{M} x y}{32\pi\left(\nu t\right)^3} e^{-\xi^2} \,, \tag{3.11}$$

$$\psi_M\left(x, y, t\right) = -\frac{\tilde{M} x y}{\pi\left(x^2 + y^2\right)^2}\left[1 - \left(1 + \xi^2\right) e^{-\xi^2}\right] \,, \tag{3.12}$$

where $\tilde{M}$ is the 2D forcing intensity of the impulsive force doublet ($[\tilde{M}] = L^4 T^{-1}$). We then change the type of the forcing (from impulsive to continuous) by using the integral operator in Equation (3.3) and perform the integration until time is large enough to obtain the steady-state solutions. The steady-state solutions of the vorticity and stream function of the wake behind a point force doublet are

$$\begin{aligned} \omega_Q\left(x, y\right) \;=\; & -\frac{\tilde{Q} U_\infty^2}{16\pi\nu^3} \frac{x y}{\left(x^2 + y^2\right)} \exp\left(\frac{x U_\infty}{2\nu}\right) K_0\left(\frac{U_\infty}{2\nu}\sqrt{x^2 + y^2}\right) \\ & -\frac{\tilde{Q} U_\infty}{4\pi\nu^2} \frac{x y}{\left(x^2 + y^2\right)^{3/2}} \exp\left(\frac{x U_\infty}{2\nu}\right) K_1\left(\frac{U_\infty}{2\nu}\sqrt{x^2 + y^2}\right) \\ & +\frac{\tilde{Q} U_\infty^2}{16\pi\nu^3} \frac{y}{\left(x^2 + y^2\right)^{1/2}} \exp\left(\frac{x U_\infty}{2\nu}\right) K_1\left(\frac{U_\infty}{2\nu}\sqrt{x^2 + y^2}\right) \,, \end{aligned} \tag{3.13}$$

$$\psi_Q\left(x, y\right) = -\frac{\tilde{Q} y}{\pi} \int_0^\infty \frac{\left(x - U_\infty \tau\right)\left[1 - \left(1 + \vartheta^2\right) e^{-\vartheta^2}\right]}{\left[\left(x - U_\infty \tau\right)^2 + y^2\right]^2} \, \mathrm{d}\tau \,. \tag{3.14}$$

where $\tilde{Q}$ is the 2D forcing intensity of the continuous force doublet ($[\tilde{Q}] = L^4 T^{-2}$). Finally, the distribution of the velocity deficit of a zero-momentum wake induced by a point force doublet along its centreline is obtained by the differentiation of the corresponding stream function as

$$u_{\mathrm{def}}\left(x, 0\right) = -\frac{\tilde{Q}}{\pi} \int_0^\infty \frac{1 - \left(1 + \varkappa^2\right) e^{-\varkappa^2}}{\left(x - U_\infty \tau\right)^3} \, \mathrm{d}\tau \,. \tag{3.15}$$

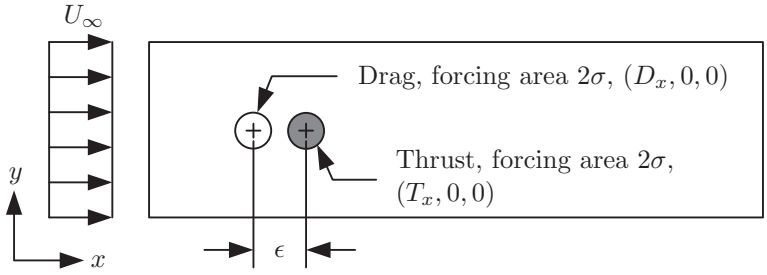

FIGURE 3.1: Schematic of geometry of a 2D momentumless wake.

3.1.2 Numerical Approach

Since a force doublet consists of both thrust and drag, we prefer to describe the numerical approach based on the implementation of the force doublet used to generate a two-dimensional momentumless wake. Note that the thrust is not active when a 2D finite-momentum wake behind a single force is computed. The drag $\boldsymbol{D} = (D_x, 0, 0)$ and the thrust $\boldsymbol{T} = (T_x, 0, 0)$ are added to the RHS of the Navier–Stokes equations and their forcing intensity is distributed to the computational grids via a 2D Gaussian function

$$D_x = -\frac{\tilde{J}_D}{\sigma^2\pi} \exp\left[-\frac{(x - x_{0,D})^2 + (y - y_{0,D})^2}{\sigma^2}\right], \tag{3.16}$$

$$T_x = \frac{\tilde{J}_T}{\sigma^2\pi} \exp\left[-\frac{(x - x_{0,T})^2 + (y - y_{0,T})^2}{\sigma^2}\right], \tag{3.17}$$

where $\boldsymbol{x}_{0,D} = (x_{0,D}, y_{0,D})$ and $\boldsymbol{x}_{0,T} = (x_{0,T}, y_{0,T})$ are respectively the centre of the drag and the thrust, and σ is the Gaussian semi-width. The 2D thrust $\tilde{J}_T$ and drag intensity $\tilde{J}_D$ are defined to be of equal magnitude while acting in the opposite directions to create a momentumless wake. The drag is applied slightly in front of the thrust with the distance $\epsilon/2\sigma = 5$. The Gaussian semi-width σ in Equations (3.16) and (3.17) is set to have the same size to reproduce the experimental work of Afanasyev & Korabel (2006) and is chosen as $\sigma = 0.2$.

The schematic of the flow geometry is displayed in Figure 3.1. The boundary condition at the upstream boundary is a constant free-stream velocity U_∞ with the forces being stationary, whilst the convective outflow boundary condition is applied at the outlet. Stress-free boundary conditions are specified in the vertical direction. In order to use the three-dimensional code, CgLES, to simulate a two-dimensional flow, free-slip boundary conditions are used in the lateral direction and the grid spacing in this direction is chosen to be extremely large compared to the other

Case	$\Pi_a = \tilde{J}/\sigma U_\infty^2$	$\Pi_\nu = \tilde{J}/\nu U_\infty$
M1	1.1	75
M2	1.4	125
M3	2.1	120
M4	2.6	130
M5	3.2	160
M6	6.0	300

TABLE 3.1: Run parameters for a 2D finite-momentum wake.

directions. The simulations of finite- and zero-momentum wakes were performed in the 2D domain size of $-50 \leqslant x/2\sigma \leqslant 190$ and $-40 \leqslant y/2\sigma \leqslant 40$, with 3072×1024 grid cells in the streamwise (x) and vertical (y) directions, respectively. It should be noted that the grid spacing used in this validation is close to a minimum mesh size of Afanasyev & Korabel's (2008) simulation, in which an unstructured grid was employed.

3.1.3 2D Finite-Momentum Wakes Generated by a Single Force

We generated finite-momentum wakes by applying a single force which acts against the incoming stream into a flow domain. This problem is similar to a towed wake behind a bluff body. Six values of forcing intensity were selected to study the dynamics of the wake and are given in terms of Π_a and Π_ν in Table 3.1. It was observed by Afanasyev & Korabel (2006, 2008) that there are two regimes of the wake induced by a localised force: (i) a stable regime when Π_a and Π_ν are quite low, and (ii) a vortex shedding regime when Π_a and Π_ν exceed their critical values.

Figure 3.2 depicts the vorticity distribution at late time. At $\Pi_a = 1.1$ and $\Pi_\nu = 75$, we observed that the wake behind the forcing is stable and is in the form of a jet-like flow (Figure 3.2a). We also compare the distribution of the streamwise velocity deficit along its centreline for these values of Π_a and Π_ν with the theoretical solution (Equation 3.8), as shown in Figure 3.3. Good quantitative agreement can be seen in both upstream and downstream of the body force, in spite of the appearance of the differences in the forcing region due to the fact that we applied a finite force whereas a point force is used in the analytical solution.

When the values of Π_a and Π_ν are increased to $\Pi_a = 1.4$ and $\Pi_\nu = 125$, the wake is not stable anymore. It can be seen from Figure 3.2(b) that the vorticity is periodically shed from the body force and is visually similar to the well-known

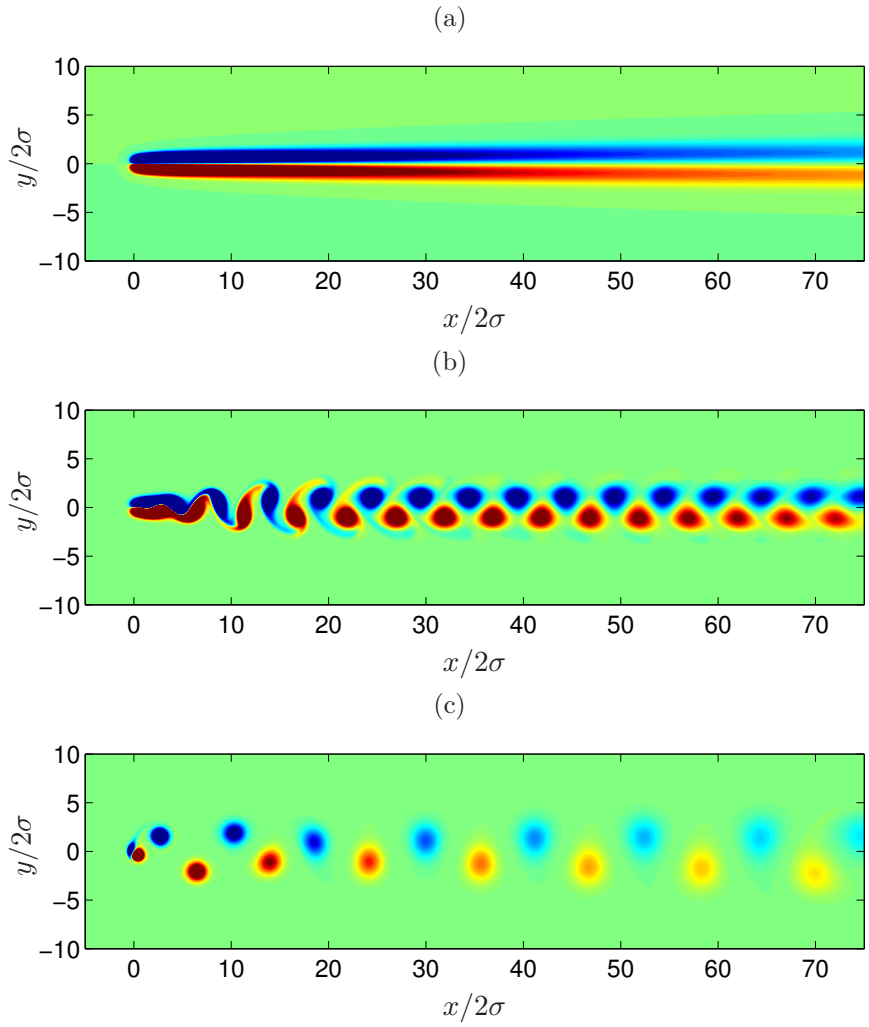

FIGURE 3.2: Contours of vorticity of 2D finite-momentum wake with different forcing intensity: (a) $\Pi_a = 1.1$ and $\Pi_\nu = 75$, (b) $\Pi_a = 1.4$ and $\Pi_\nu = 125$, (c) $\Pi_a = 6.0$ and $\Pi_\nu = 300$. Vorticity varies from $-0.2\,|\omega_z|_{\max}$ to $0.2\,|\omega_z|_{\max}$.

Kármán vortex street. In order to compare our results with Afanasyev & Korabel's (2008) data, we collected history of the vorticity at $x/2\sigma = 7.5$ and then used a Fast Fourier Transform (FFT) to analyse the time series of the vorticity to obtain the shedding frequency f_s. The non-dimensional frequency, Strouhal number $St = f_s\tilde{J}/U_\infty^3$, versus Π_a is illustrated in Figure 3.4. Our shedding frequency is in excellent agreement with the results of Afanasyev & Korabel (2008). It is of interest to note that Afanasyev & Korabel (2008) reported that the vortex street underwent from regular to irregular shedding when the shedding frequency rapidly dropped. The transition to the irregular shedding regime was observed to occur around $\Pi_a = 2.6$ (see Figure 3.4). The distribution of the vorticity in the irregular shedding regime is illustrated in Figure 3.2(c), where $\Pi_a = 6.0$ and $\Pi_\nu = 300$.

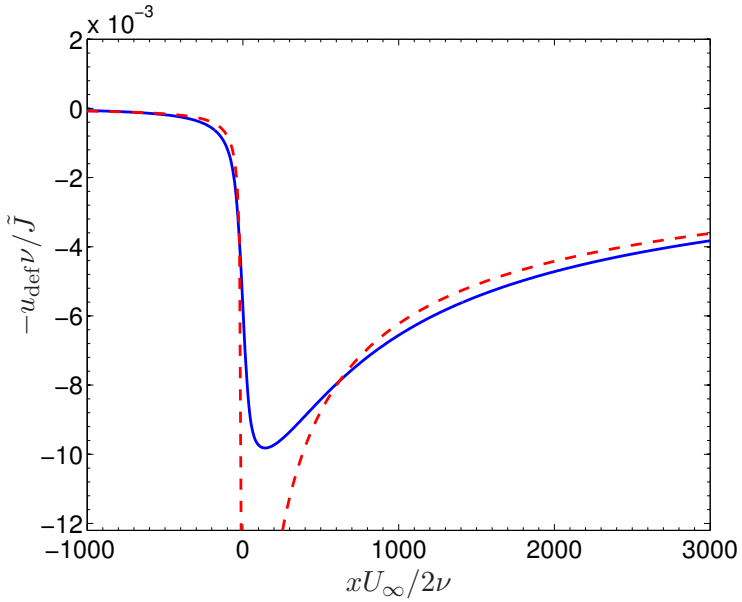

FIGURE 3.3: Distribution of the streamwise velocity deficit along its axis of a 2D finite-momentum wake: $\Pi_a = 1.1$ and $\Pi_\nu = 75$: —— Present (finite source); - - - - Theoretical solution (point source, Equation 3.8).

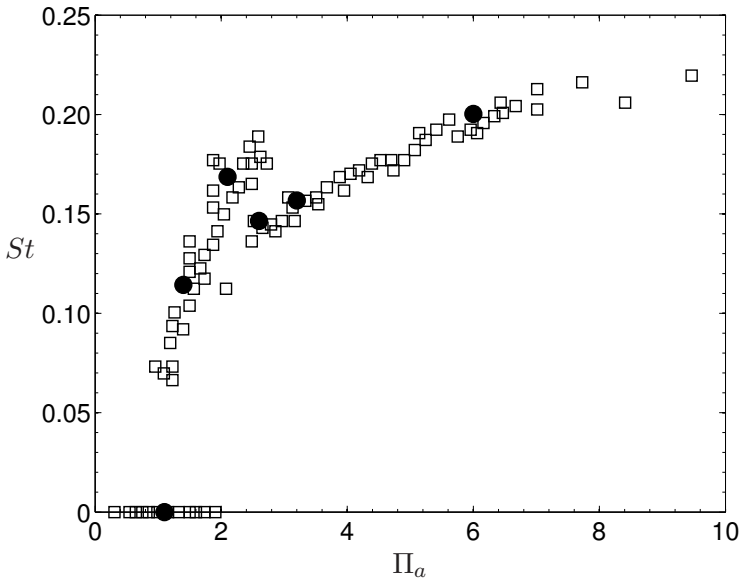

FIGURE 3.4: Strouhal number versus Π_a of a 2D finite-momentum wake: ● Present; □ Afanasyev & Korabel (2008).

Case	$\Pi_a = \tilde{J}/\sigma U_\infty^2$	$\Pi_\nu = \tilde{J}/\nu U_\infty$
Z1	1.0	50
Z2	2.1	120
Z3	3.0	150
Z4	4.0	200
Z5	6.0	300
Z6	8.0	400
Z7	11.0	230

TABLE 3.2: Run parameters for a 2D zero-momentum wake.

3.1.4 2D Zero-Momentum Wakes behind a Force Doublet

The strategy to impose a force doublet (drag of a body plus thrust) was validated by performing a two-dimensional (2D) simulation of zero-momentum wakes. The results are compared with both an analytical solution of Afanasyev (2004), which was explained earlier in § 3.1.1, and experimental results of Afanasyev & Korabel (2006). The run parameters Π_a and Π_ν for this study are provided in Table 3.2. Note that this range of Π_a contains the wakes in both stable and vortex shedding regimes.

The distribution of the vorticity at late time is displayed in Figure 3.5. In the stable regime (Figure 3.5a), the momentumless wake is in the from of a jet convecting downstream similar to that in the simulation with the single force. Figure 3.6 displays the distribution of the streamwise velocity deficit along the axis of the flow at $\Pi_a = 1$ and $\Pi_\nu = 50$, compared with an analytical solution provided in Equation (3.15). Away from the expected near-field deviation (due to comparing finite versus singular dipoles), the agreement is satisfactory. The balance of the streamwise momentum flux was also checked to make sure that the net momentum flux of the zero-momentum wake in this direction is identically zero (recall that no net momentum is imparted into the wake by the force doublet). The conservation of x-momentum can be written as,

$$\frac{\mathrm{d}}{\mathrm{d}t}\left(\int u\,\mathrm{d}x\,\mathrm{d}y\,\mathrm{d}z\right) + F_M = \int (D_x + T_x)\,\mathrm{d}x\,\mathrm{d}y\,\mathrm{d}z\,, \tag{3.18}$$

where F_M is the net volume-integrated momentum flux, including the difference between the momentum, pressure and viscous fluxes at the inlet and outlet planes. If was found that the LHS terms of Equation (3.18) is of $\mathcal{O}(10^{-5})$.

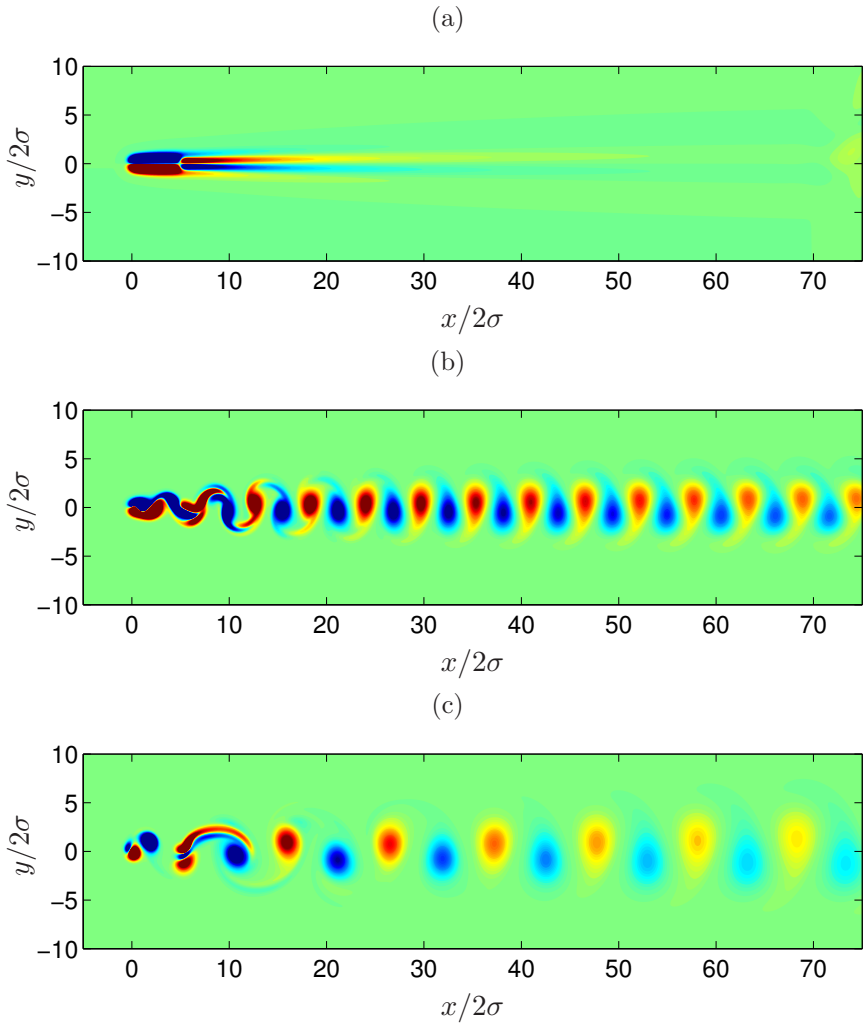

FIGURE 3.5: Contours of vorticity of 2D momentumless wake with different forcing intensity: (a) $\Pi_a = 1.0$ and $\Pi_\nu = 50$, (b) $\Pi_a = 2.1$ and $\Pi_\nu = 120$, (c) $\Pi_a = 11.0$ and $\Pi_\nu = 230$. Vorticity varies from $-0.2\,|\omega_z|_{max}$ to $0.2\,|\omega_z|_{max}$.

For higher value of Π_a and Π_ν ($\Pi_a = 2.1, \Pi_\nu = 120$), the vortex street was observed to appear behind the doublet (see Figure 3.5b). The vortex street in this simulation is visually similar to the mushroom-like vortex sheet observed in Afanasyev & Korabel's (2006) experiment. For a quantitative comparison with the laboratory experiment of Afanasyev & Korabel (2006), the shedding frequency was measured by performing a FFT of the vorticity at $x/2\sigma = 12.5$. A plot of St versus Π_a for the zero-momentum wakes is displayed in Figure 3.7, showing that the numerical results are in good agreement with the experimental data. Note that we could not observe any sign of a rapid drop of the shedding frequency for the zero-momentum wake. Once the magnitude of the forcing intensity increases to $\Pi_a = 11$ and $\Pi_\nu = 230$, the size of the mushroom-like vortex is bigger, while its shape is similar to that in the lower magnitude as illustrated in Figure 3.5(c).

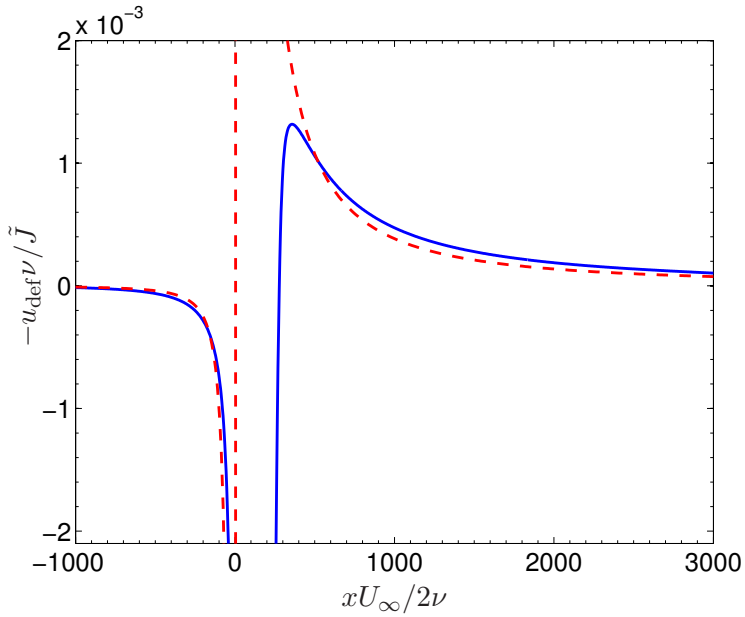

FIGURE 3.6: Distribution of the streamwise velocity deficit along its axis of a 2D zero-momentum wake: $\Pi_a = 1$ and $\Pi_\nu = 50$: —— Present (finite-size force doublet); - - - - Theoretical solution (point force doublet, Equation 3.15).

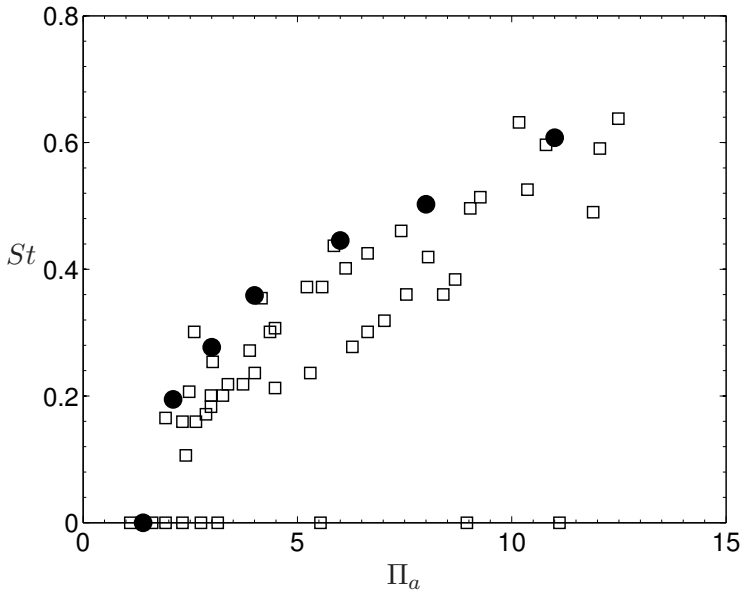

FIGURE 3.7: Strouhal number versus Π_a of a 2D zero-momentum wake: ● Present; □ Afanasyev & Korabel (2006).

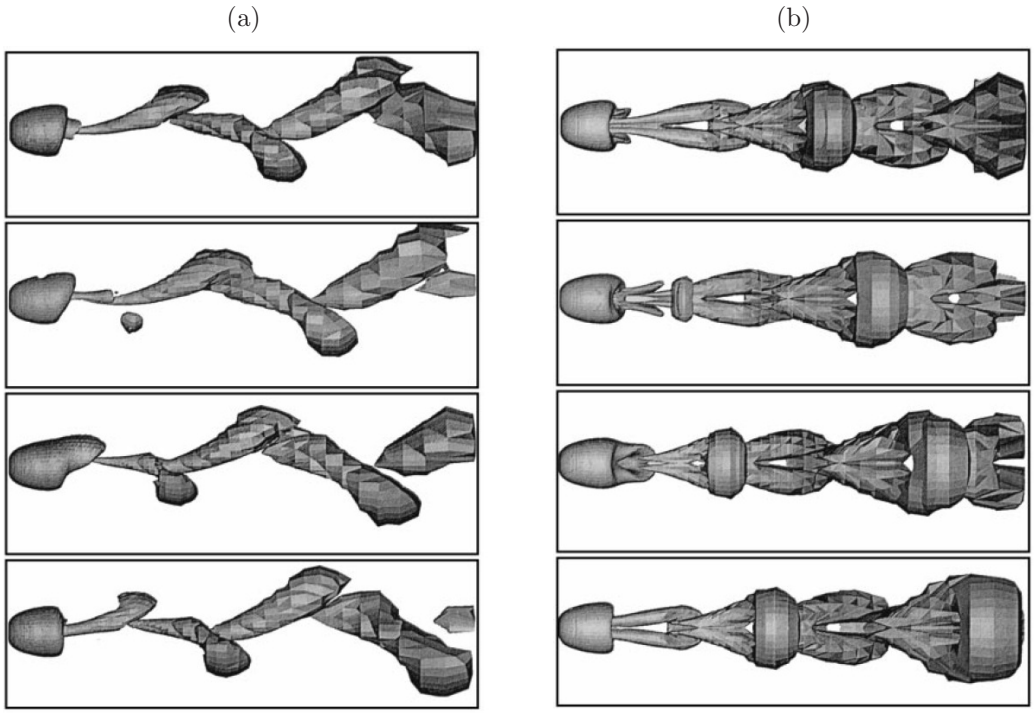

FIGURE 3.8: Evolution of vortical structure of flow past a sphere at $Re_b = 300$ at every quarter period from Johnson & Patel (1999): (a) side view; (b) top view.

3.2 Generate a Virtual Body using Immersed Boundary Method

Flow past a sphere at $Re_b = 300$ was selected to validate the implementation of the IB approach in CgLES. The Reynolds number is defined in terms of the free-stream velocity U_∞ and the sphere diameter D_b, i.e. $Re_b = U_\infty D_b/\nu$. At this Reynolds number, the flow is still laminar, but it is unsteady and planar symmetric. It is thus expected to observe a coherent vortical structure periodically shed with a constant strength in the same orientation (Johnson & Patel, 1999; Tomboulides & Orszag, 2000), as displayed in Figure 3.8.

The simulations with both the PI and the P controllers were carried out in the domain of size $-10 \leqslant x/D_b \leqslant 26$, $-5 \leqslant y/D_b \leqslant 5$ and $-5 \leqslant z/D_b \leqslant 5$, with the number of grid cells $576 \times 160 \times 160$. The sphere is located at $(0, 0, 0)$ and is mimicked by using 931 equally spaced Lagrangian points whose grid spacing is equal to the Eulerian grid spacing. Inflow and convective outflow boundary conditions are employed in the streamwise (x) direction, whilst free-slip boundary conditions are applied in the lateral (y) and vertical (z) directions.

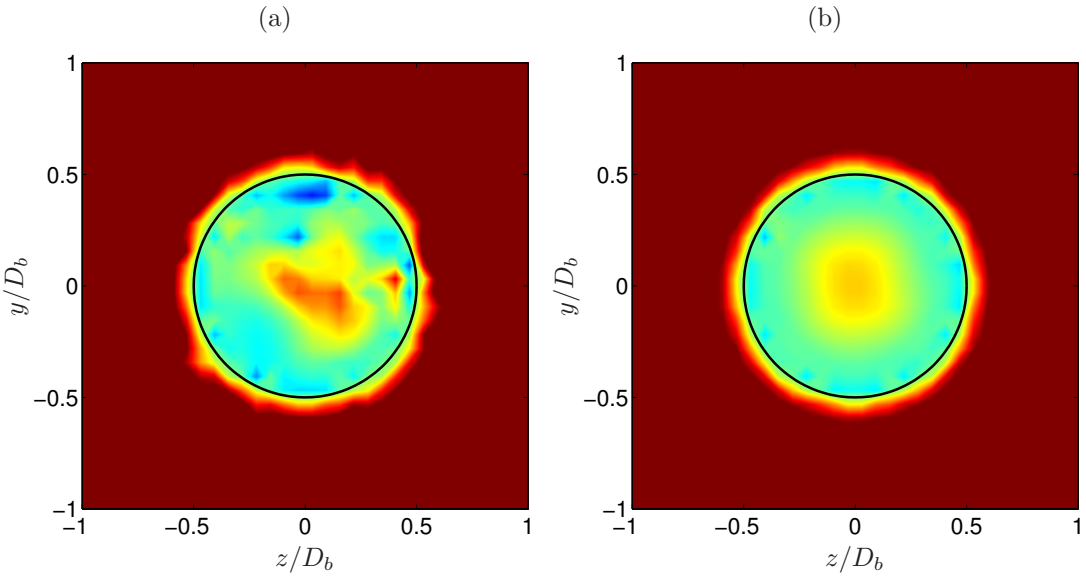

FIGURE 3.9: Contours of the streamwise velocity at $x/D_b = 0$, $tU_\infty/D_b = 40$ and $Re_b = 300$ from the simulation using the proportional-integral feedback: (a) Case PI1 ($\varphi_f D_b^2/U_\infty^2 = -3947.8418$, $\beta_f D_b/U_\infty = -125.6637$); (b) Case PI2 ($\varphi_f D_b^2/U_\infty^2 = -246.7401$, $\beta_f D_b/U_\infty = -31.4159$). The edge of the sphere is represented by the black circle. The streamwise velocity varies from $-1 \leq u_x/U_\infty \leq 1$.

3.2.1 Proportional-Integral Feedback

Since Equation (2.10) represents a simple mass-spring-damper system (Fadlun *et al.*, 2000), the integral φ_f and proportional β_f gains can be obtained from the angular frequency of the oscillator ω_f and the damping ratio ζ as

$$\varphi_f = -\omega_f^2, \quad \beta_f = -2\zeta\omega_f \,. \tag{3.19}$$

where ω_f can be obtained from the oscillation time scale T_o, i.e. $\omega_f = 2\pi/T_o$, and ζ is chosen to be 1 to give a critically damped response.

The simulation of flow past a sphere was first carried out with $\varphi_f D_b^2/U_\infty^2 = -3947.8418$ and $\beta_f D_b/U_\infty = -125.6637$, labelled as Case PI1, to test the efficiency of the PI feedback. The simulation was performed until $tU_\infty/D_b = 40$ with the time step size $\Delta tU_\infty/D_b = 0.002$. It was observed that the PI feedback could not represent a smooth axisymmetric sphere as shown in Figure 3.9(a). This happened because the time step size used in this simulation is higher than the numerical stability limit.

To improve the stability limit, we decreased φ_f and β_f rather than reducing the time step size in order to maintain the computational cost. The values of

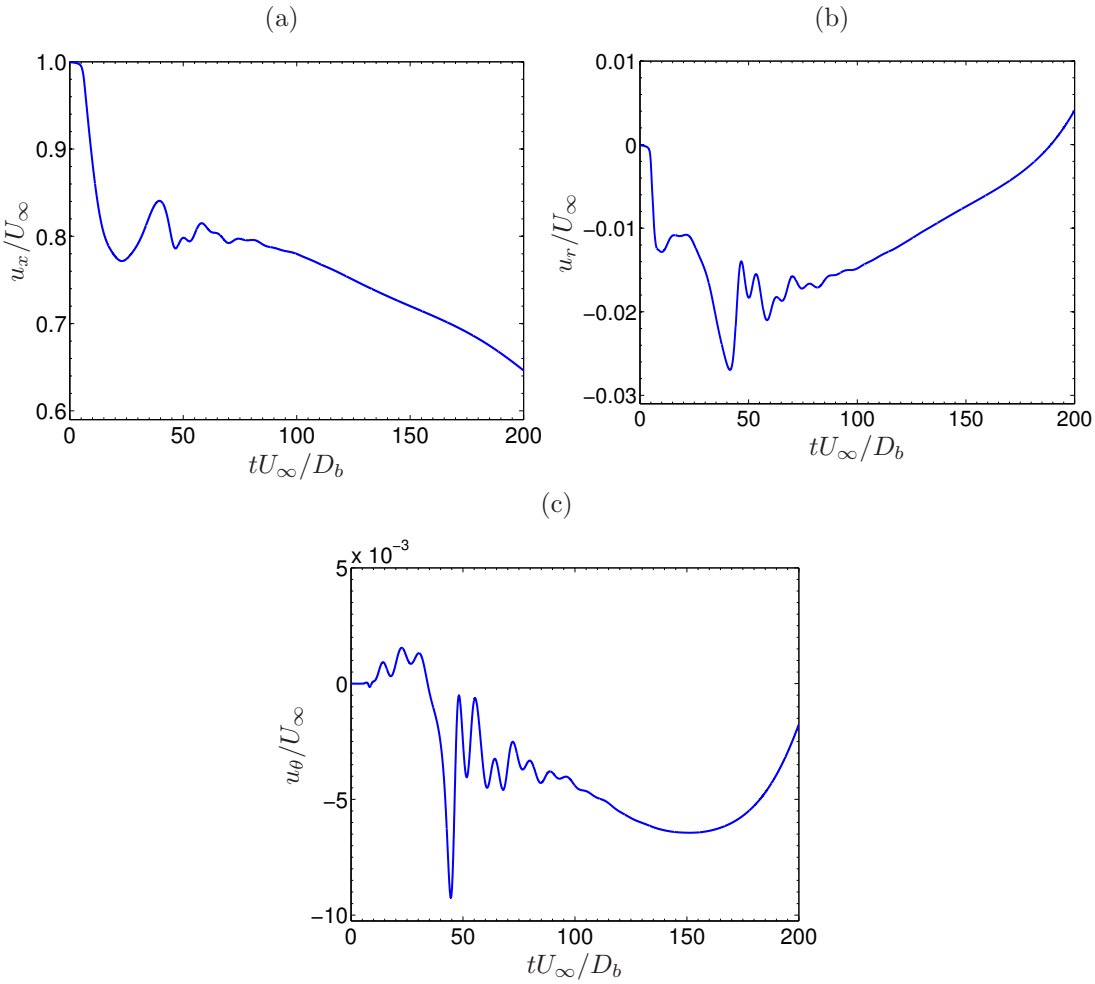

FIGURE 3.10: Histories of the cylindrical velocity components at $x/D_b = 5.78$, $r/D_b = 0.4$ and $Re_b = 300$ from the simulation using the proportional-integral feedback with $\varphi_f D_b^2/U_\infty^2 = -246.7401$, $\beta_f D_b/U_\infty = -31.4159$ (Case PI2): (a) u_x, (b) u_r and (c) u_θ.

the proportional and integral gains were decreased to $\varphi_f D_b^2/U_\infty^2 = -246.7401$ and $\beta_f D_b/U_\infty = -31.4159$ (labelled as Case PI2) at which the PI feedback can represent a smoother axisymmetric sphere (Figure 3.9b). To make the comparison between Figures 3.9(a) and 3.9(b) more quantitative, the mean error $\varepsilon_{\text{mean}}$, which is the azimuthal average of the difference between the streamwise velocity and the desired velocity (set to zero to represent the no-slip surface of the virtual sphere) at $r/D_b = 0.5$, and the root-mean-square error ε_{rms} were determined. It was found that $\varepsilon_{\text{mean}} = -0.0414$ and $\varepsilon_{\text{rms}} = 0.0318$ for Case PI1, while the values of $\varepsilon_{\text{mean}}$ and ε_{rms} for Case PI2 reduce to -0.0383 and 0.0182, respectively. The significant drop (about 1.75 times) in ε_{rms} is important in this work since it can prevent the occurrence of spurious small-scale turbulence (as can be seen in Figure 3.9a) that might affect the formation and evolution of a far-field coherent structure. The simulation with the new values of the proportional and integral gains was

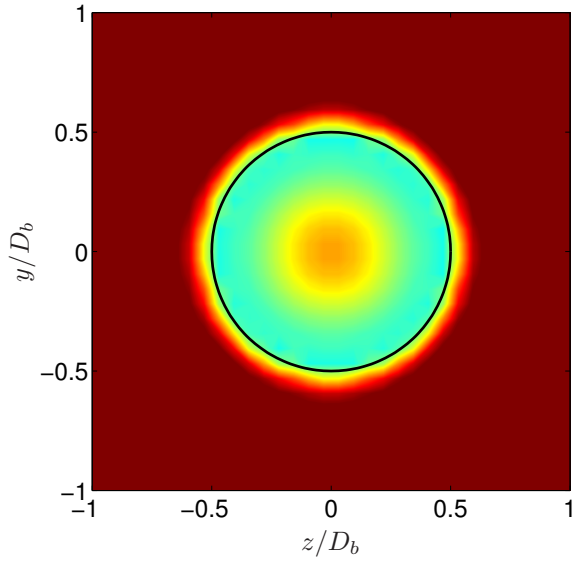

FIGURE 3.11: Contour of the streamwise velocity at $x/D_b = 0$, $tU_\infty/D_b = 40$ and $Re_b = 300$ from the simulation using the proportional feedback. The edge of the sphere is represented by the black circle. The streamwise velocity varies from $-1 \leq u_x/U_\infty \leq 1$.

advanced for a total of 200 time units. Histories of the streamwise u_x, radial u_r and azimuthal u_θ velocity components in the near field region are displayed in Figure 3.10. The histories of all the velocity components do not show any sign of a fluctuation that would appear at $tU_\infty D_b \approx 100$ (see Figure 3.12), implying that the vortex shedding could not be observed behind the sphere in this simulation because the gains used are not high enough to drive the boundary force to react as fast as the biggest frequency of the flow.

3.2.2 Proportional Feedback

The proportional gain β_f in Equation (2.15) was chosen as the inverse of the time step size ($\beta_f = -1/\Delta t$), in such a way that maximises gain while maintaining stability. The simulation was performed with the time step size $\Delta t U_\infty/D_b = 0.004$, corresponding to $\beta_f D_b/U_\infty = 250$ (two times higher than that in § 3.2.1). Even though the time step size used in this simulation is two times higher than that in § 3.2.1, the proportional feedback can still produce a smooth axisymmetric sphere with $\varepsilon_{\text{mean}} = -0.0317$ and $\varepsilon_{\text{rms}} = 0.0169$, as shown in Figure 3.11.

Histories of the cylindrical velocity components are plotted in the near wake at $x/D_b = 5.78$ and $r/D_b = 0.4$ and are displayed in Figure 3.12. It can be observed that the fluctuating velocities begin to appear at $tU_\infty/D_b \approx 100$, suggesting that

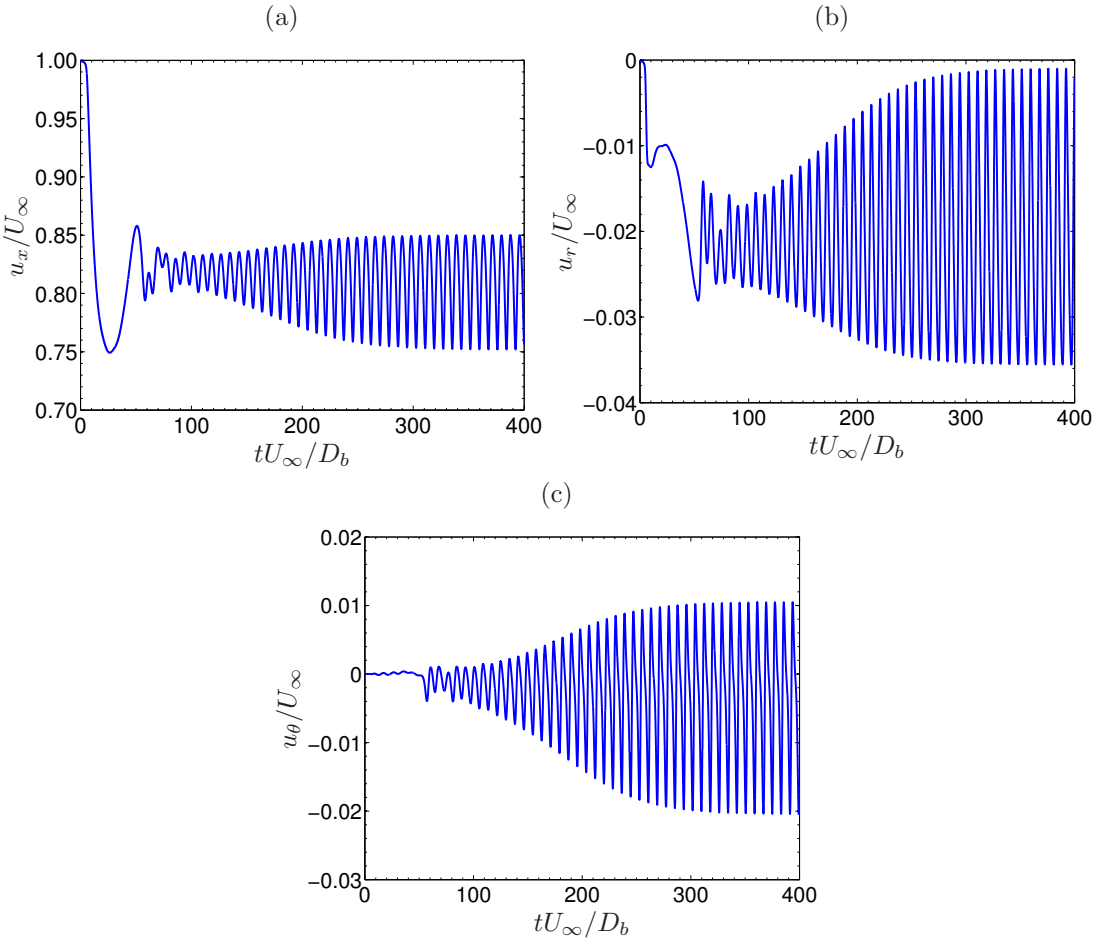

FIGURE 3.12: Histories of the cylindrical velocity components at $x/D_b = 5.78$, $r/D_b = 0.4$ and $Re_b = 300$ from the simulation using the proportional feedback: (a) u_x, (b) u_r and (c) u_θ. At this Reynolds number, the velocity field periodically oscillates due to the appearance of the vortex shedding.

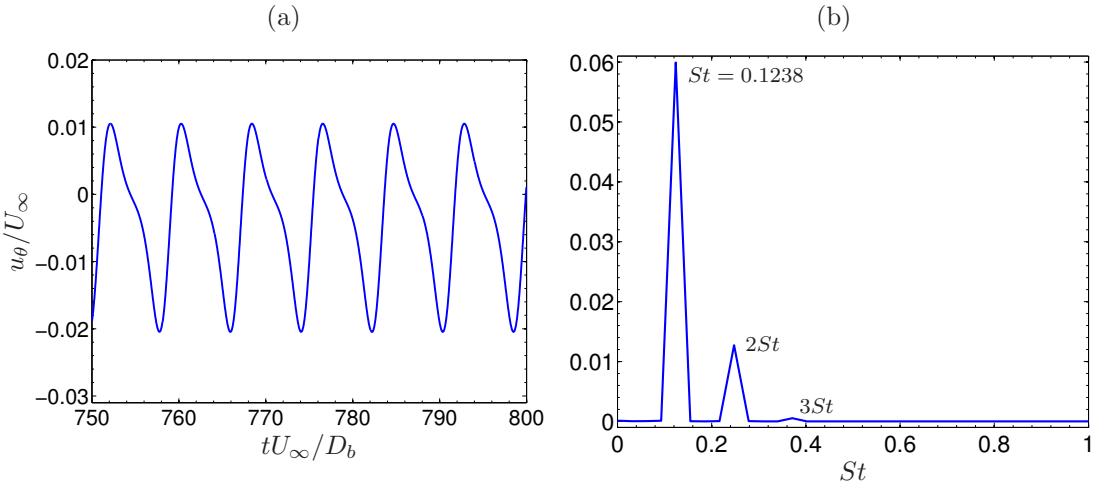

FIGURE 3.13: (a) History of the azimuthal velocity at late time and (b) its power spectrum at $x/D_b = 5.78$, $r/D_b = 0.4$ and $Re_b = 300$ from the simulation using the proportional feedback.

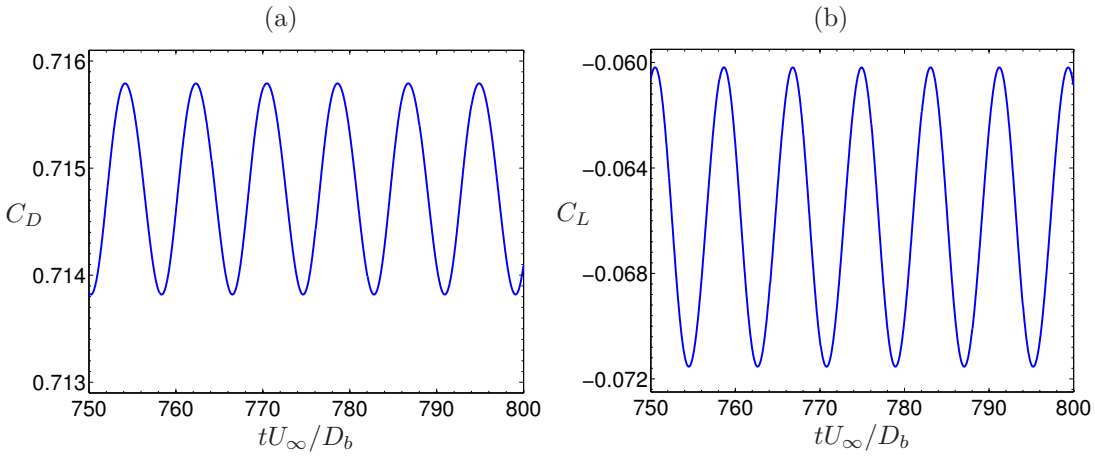

FIGURE 3.14: Histories of (a) the drag C_D and (b) the lateral force C_L coefficients at $Re_b = 300$ from the simulation using the proportional feedback.

the vortex shedding would be observed around that time. After the flow reached its statistically steady state, the simulation was further carried out for the next 400 time units giving the total time steps of 800. The simulation was time averaged for the last 200 time units, corresponding to about 25 shedding periods. History of the azimuthal velocity and its power spectrum at late time are illustrated in Figure 3.13. The non-dimensional shedding frequency, Strouhal number $St = f_s D_b/U_\infty$, found in this work is $St = 0.1238$. Note that we also observed the second and the third superharmonics of the shedding frequency as shown in figure 15 of Tomboulides & Orszag (2000).

Figure 3.14(a) shows a plot of the drag coefficient C_D versus time, whilst history of the lateral force coefficient C_L is displayed in Figure 3.14(b). The drag and the lateral force coefficients are calculated as

$$C_D = \frac{\int B_x \, \mathrm{d}x \, \mathrm{d}y \, \mathrm{d}z}{\frac{1}{8} U_\infty^2 \pi D_b^2}, \quad C_L = \frac{\int B_y \, \mathrm{d}x \, \mathrm{d}y \, \mathrm{d}z}{\frac{1}{8} U_\infty^2 \pi D_b^2}, \tag{3.20}$$

where B_x and B_y are the streamwise and lateral boundary forces, respectively.

The coefficients of the drag and lateral force and the Strouhal number are compared with the values reported by Johnson & Patel (1999), Tomboulides & Orszag (2000) and Ploumhans *et al.* (2002), and are displayed in Table 3.3. A relative error of those quantities is also computed and is given in Table 3.4. It was found that the relative difference between our values and those reported by the references is lower than 10%. It is of importance to note that the correctness of predicting the drag coefficient and the Strouhal number — in which more accuracy can be obtained by increasing the number of points in the boundary layer of

	$\overline{C}_D$	$\overline{C}_L$	St
Present (immersed boundary, proportional feedback)	0.7148	−0.0658	0.1238
Johnson & Patel (1999) (finite-difference, body-fitted)	0.656	−0.069	0.137
Tomboulides & Orszag (2000) (spectral element, body-fitted)	0.6714	–	0.136
Ploumhans *et al.* (2002) (vortex method)	0.683	−0.061	0.135

TABLE 3.3: Comparison of time-averaged values of the drag $\overline{C}_D$ and the lateral force $\overline{C}_L$ coefficients, and the Strouhal number St at $Re_b = 300$ from the simulation using the proportional feedback.

	$\overline{C}_D$	$\overline{C}_L$	St
Johnson & Patel (1999) (finite-difference, body-fitted)	8.96%	4.64%	9.64%
Tomboulides & Orszag (2000) (spectral element, body-fitted)	6.46%	–	8.97%
Ploumhans *et al.* (2002) (vortex method)	4.66%	7.87%	8.30%

TABLE 3.4: Relative error between the values of $\overline{C}_D$, $\overline{C}_L$ and St, from the simulation using the proportional feedback, and the values reported by the references listed in Table 3.3.

the virtual sphere — is not important in this work since we assume that the late-time characteristics of a dipole depend only on the bulk integral momentum, i.e. independent of the small-scale shear layers associated with the boundary layer of the virtual body. The main role of the virtual body is just to impart the drag into the flow in order to provide the desired amount of the net momentum flux (the difference between the thrust and the drag). The proof of this assumption will be shown later in § 4.

Figure 3.15 displays the time-averaged streamwise velocity $\overline{u}_x$ along its centre-line compared with the DNS result of Tomboulides & Orszag (2000) at the same Reynolds number. The distribution of $\overline{u}_x$ in the near wake was found to agree well with Tomboulides & Orszag's (2000) data although some discrepancies were

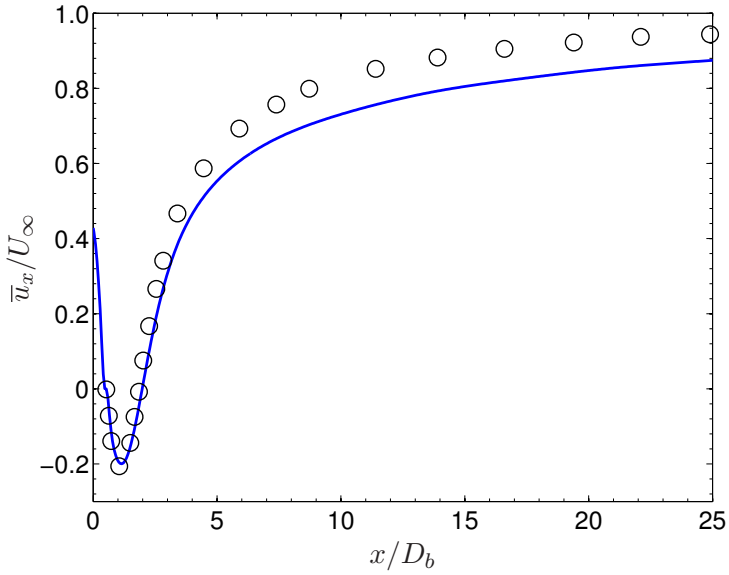

FIGURE 3.15: Time-averaged streamwise velocity $\overline{u}_x$ along its axis, obtained from the simulation using the proportional feedback, compared with the numerical result from Tomboulides & Orszag (2000) at $Re_b = 300$: —— Present; ○ Tomboulides & Orszag (2000).

observed in the far field due to the fact that the number of grid points used in this simulation is not fine enough to fully resolve the flow within the boundary layer. The boundary-layer thickness of a sphere at $Re_b = 300$ can be approximated as $\delta = 1.13/Re_b^{1/2} = 0.065$, where δ is the non-dimensional boundary-layer thickness (Schlichting, 1979). It can be seen from this approximation that only one grid point was placed within the boundary layer.

Finally, the vortex shedding mechanism is studied by visualising the isosurface of the second invariant of the velocity gradient tensor Q proposed by Hunt *et al.* (1988). The second invariant of the velocity gradient tensor is defined as

$$Q = -\frac{1}{2}\frac{\partial u_i}{\partial x_j}\frac{\partial u_j}{\partial x_i} = \frac{1}{2}\left(\Omega_{ij}\Omega_{ij} - S_{ij}S_{ij}\right) , \tag{3.21}$$

where $\Omega_{ij} = (u_{i,j} - u_{j,i})/2$ is the rate of rotation tensor and $S_{ij} = (u_{i,j} + u_{j,i})/2$ is the rate of strain tensor. Hence, Q represents whether the rotation rate exceeds the shear strain rate. More details of the Q-definition and the other markers of a vortical structure can be found in Jeong & Hussain (1995) and in a review of Chakraborty *et al.* (2005).

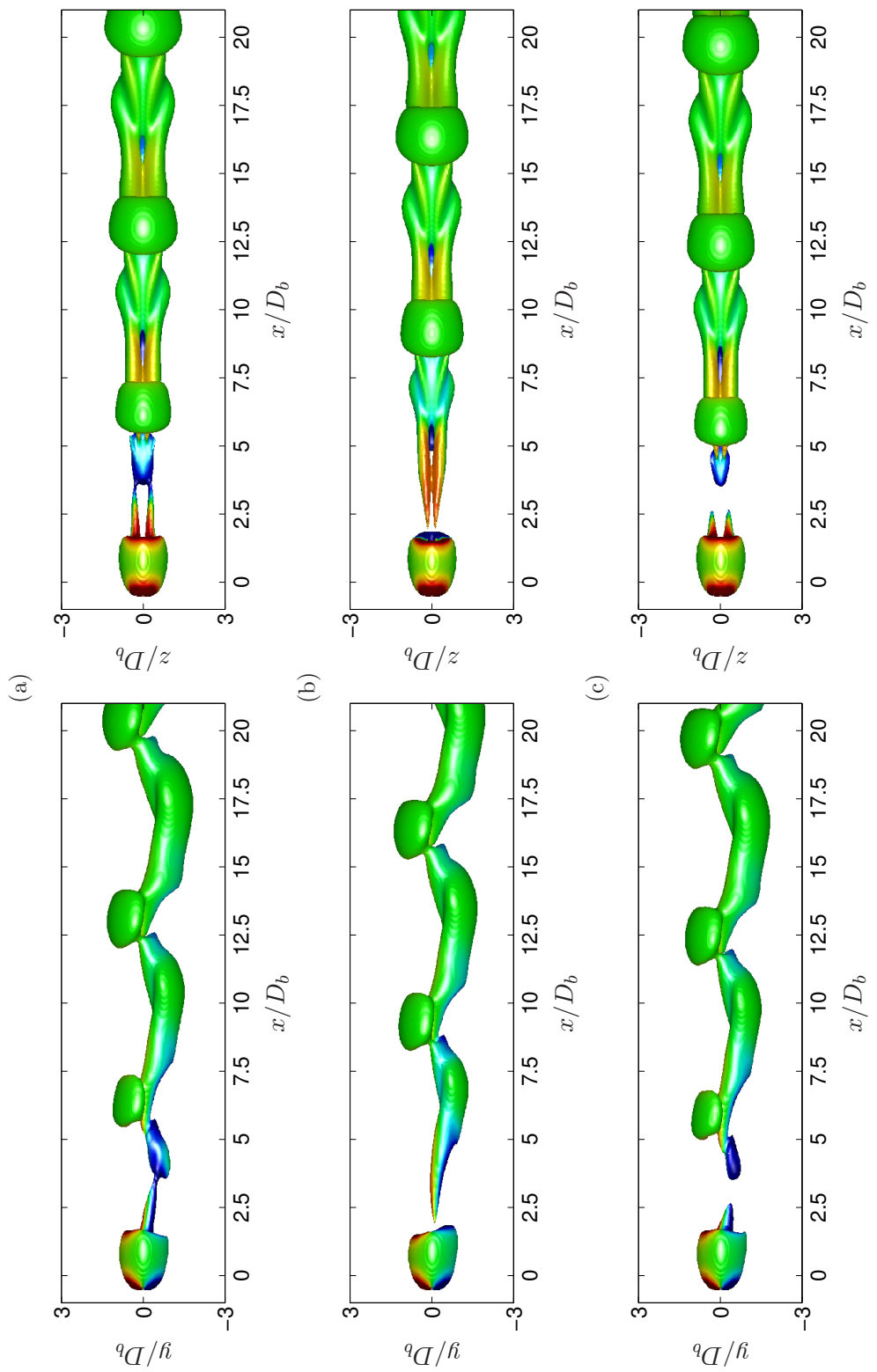

FIGURE 3.16: xy- and xz-planes (left and right part of the picture, respectively) of vortical structure (visualised by the isosurface of Q) periodically shed from the sphere at $Re_b = 300$: (a) $tU_\infty/D_b = 400$, (b) $tU_\infty/D_b = 420$, (c) $tU_\infty/D_b = 440$.

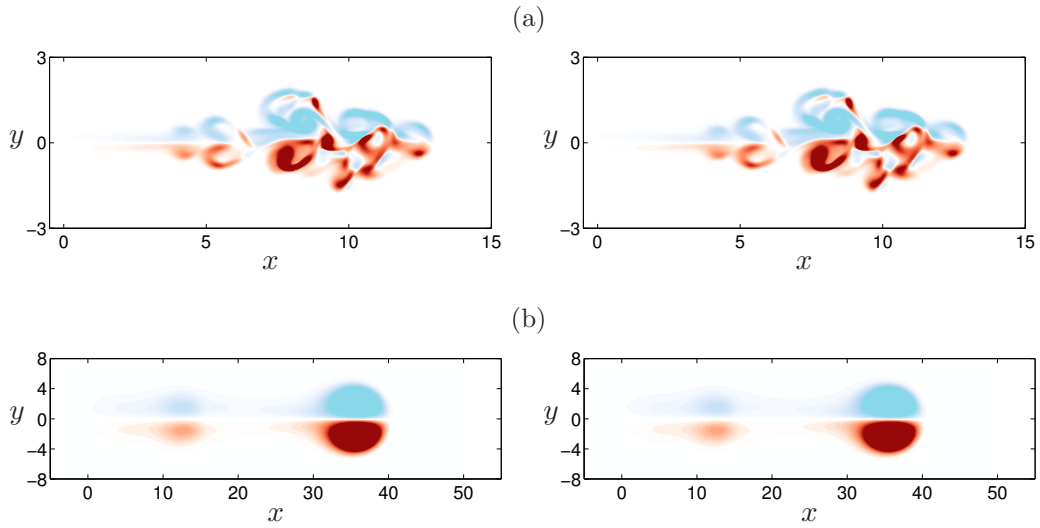

FIGURE 3.17: Contours of ω_z at the free surface from (left) Case JS3a and (right) Case JS3aDR at (a) the projected time ($t = 50$) and (b) $t = 3000$. Vorticity varies from $-0.2 < \omega_z/|\omega_z|_{\max} < 0.2$. Blue (light) and red (dark) patches show negative and positive vorticity, respectively. Plots at $t = 50$ show only selected region of the streamwise and lateral domains, while the full domain is displayed for the plots at $t = 3000$.

The vortical structure behind the sphere is shown in Figure 3.16 and each frame is 20 time units apart. It can be seen that the hairpin-like vortex forms very close to the sphere (about five diameters downstream of the sphere centre). While it convects downstream, the legs of the vortex stretch and are connected to the head of the next vortex, which is shed in the same orientation as the previous one. Our flow visualisation is in very good agreement with the hairpin vortex of Johnson & Patel (1999), which is illustrated in Figure 3.8.

3.3 Validation of Domain Resizing

The accuracy of the vector-potential solver (Equations 2.26 and 2.27) and the boundary conditions used (Equation 2.29) was validated as described below. We first computed a turbulent patch induced by an impulsive jet, which acts over a short time period Δt_f with a forcing intensity J_T, at $Re_j = J_T^{1/2}/\nu = 1250$ in a shallow fluid domain corresponding to the confinement number (see Equation 1.9) of 2 (cf. Case JS3a; see Table 4.1 for details of the grid resolution and the domain size). At this value of C, the vertical growth of the patch is limited, leading to a vortex dipole at late time. Note that more details of the dynamics of a vortex dipole will be given later in § 4. At $t = 50$, the vorticity field of Case JS3a was projected to another computational domain whose size and resolution are exactly

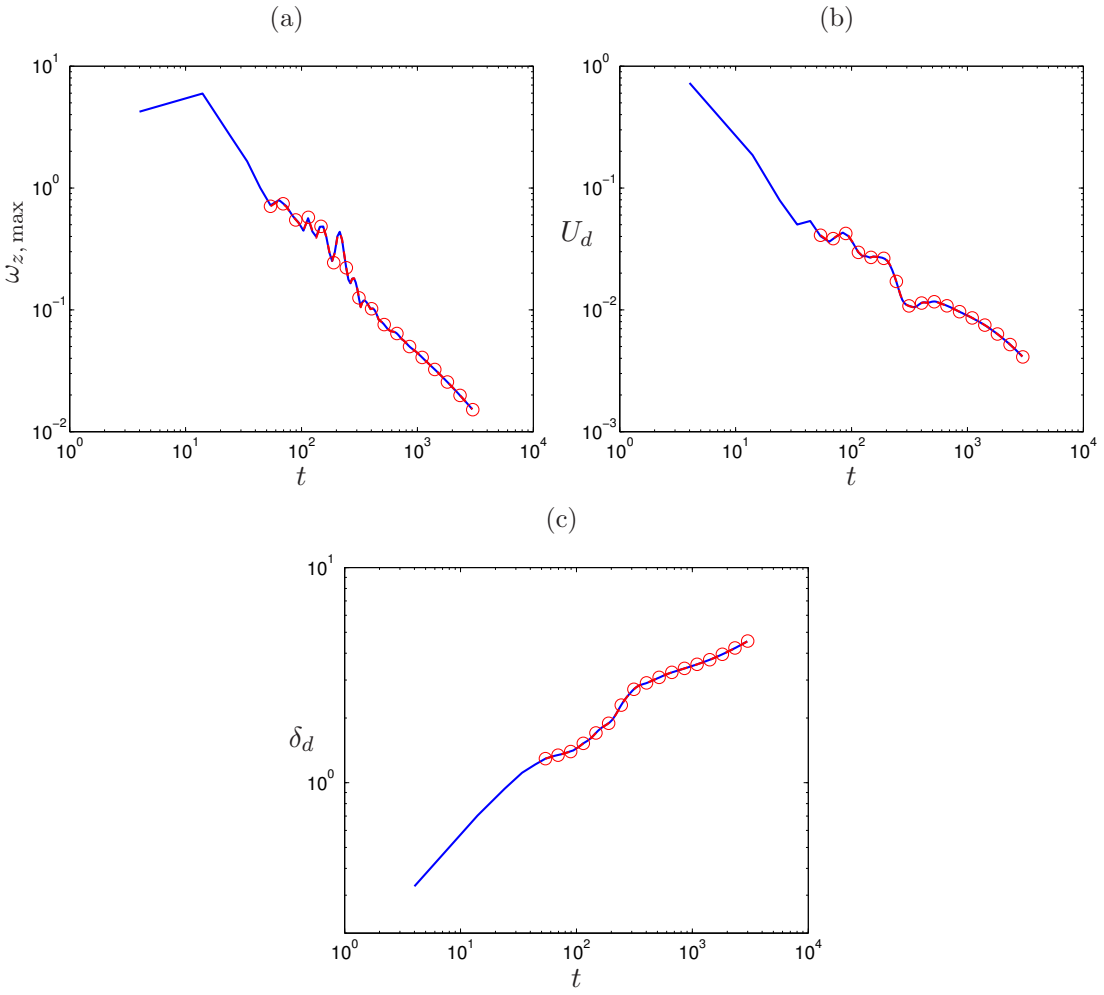

FIGURE 3.18: Comparison of dipole characteristics between Case JS3a and Case JS3aDR: —— Case JS3a; --○-- Case JS3aDR. (a) Maximum vertical vorticity at the free surface. (b) Dipole propagation velocity. (c) Dipole size. Case JS3aDR starts at $t = 50$.

the same. We labelled the simulation started from the projected vorticity field as Case JS3aDR. The velocity field of Case JS3aDR was obtained by solving Equations (2.26) – (2.27). The simulations of both cases were continued until $t = 3000$, at which the dipole is fully formed.

The vorticity contours in Figure 3.17 are used to visually quantify any difference between the vertical vorticity ω_z at the free surface from Case JS3aDR and that of Case JS3a. It is of importance to note that ω_z at $t = 50$ of Case JS3aDR, displayed in Figure 3.17, is obtained by taking the curl of its velocity field (i.e. taking the curl of Equation 2.27), not the projected vorticity field from Case JS3a. It can be seen that ω_z at the free surface from the present simulation is visually similar to that from Case JS3a at both the projected time ($t = 50$) and $t = 3000$. The dipole characteristics (i.e. the maximum vertical vorticity at the free surface

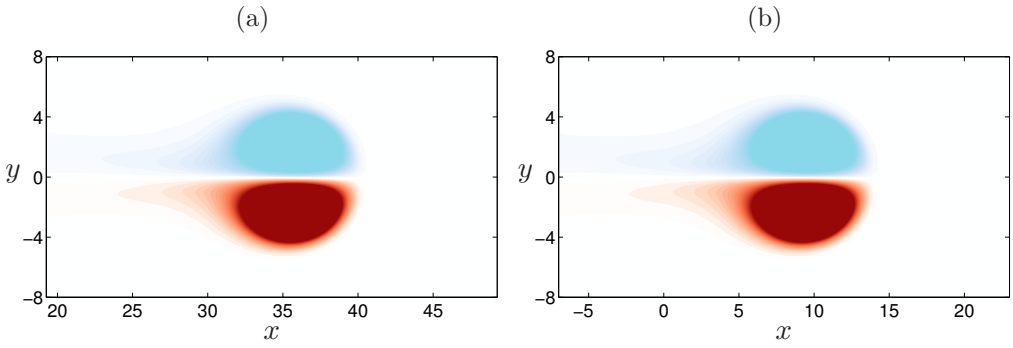

FIGURE 3.19: Contours of ω_z at the free surface from (a) Case JS3a and (b) Case JS3aMF (at which a co-moving frame of reference attached to a vortex is employed) at $t = 3000$. Vorticity varies from $-0.2 < \omega_z/|\omega_z|_{\max} < 0.2$. Blue (light) and red (dark) patches show negative and positive vorticity, respectively. Only selected region of the streamwise domain of Case JS3a is shown here, while the full domain of Case JS3aMF is illustrated.

$\omega_{z,\max}$, the dipole size δ_d (Equation 4.1), and the dipole translation velocity U_d (Equation 4.4)) of Case JS3aDR are determined to ensure the correctness of the vector-potential solver and are compared with the baseline case (Case JS3a), as displayed in Figure 3.18. For all the quantities, very close agreement was obtained with the maximum relative difference being within 2%.

3.4 Validation of Moving Reference Frame Attached to a Vortex

We validated the PI controller used to adjust the speed of the co-moving reference frame by projecting the vorticity field of Case JS3a (see Table 4.1) at $t = 50$ to a smaller computation domain using a window function given in Equation (2.23). The new velocity field of this validation was obtained using Equations (2.26) – (2.27). The simulation (labelled as Case JS3aMF) was performed in a domain of size $-7 \leqslant x \leqslant 23$, $-8 \leqslant y \leqslant 8$ and $-0.5 \leqslant z \leqslant 0.5$, with $960 \times 512 \times 32$ grid cells resulting in the same grid resolution as Case JS3a.

The PI controller and the proportional and integral gains used locate the coherent structure to within 5×10^{-5} of the target position by 8 time units. Once locked in place, the vortex remains at this position, in spite of changing its translation speed. Contours of the vertical vorticity at the free surface from Case JS3a and the present calculation are given in Figure 3.19, showing exactly the same counter-rotating vortical structure at late time ($t = 3000$). The characteristics of the coherent structure of the present computation, compared with Case JS3a, are illustrated in Figure 3.20. Despite a decrease in the impulse (about 9%) due

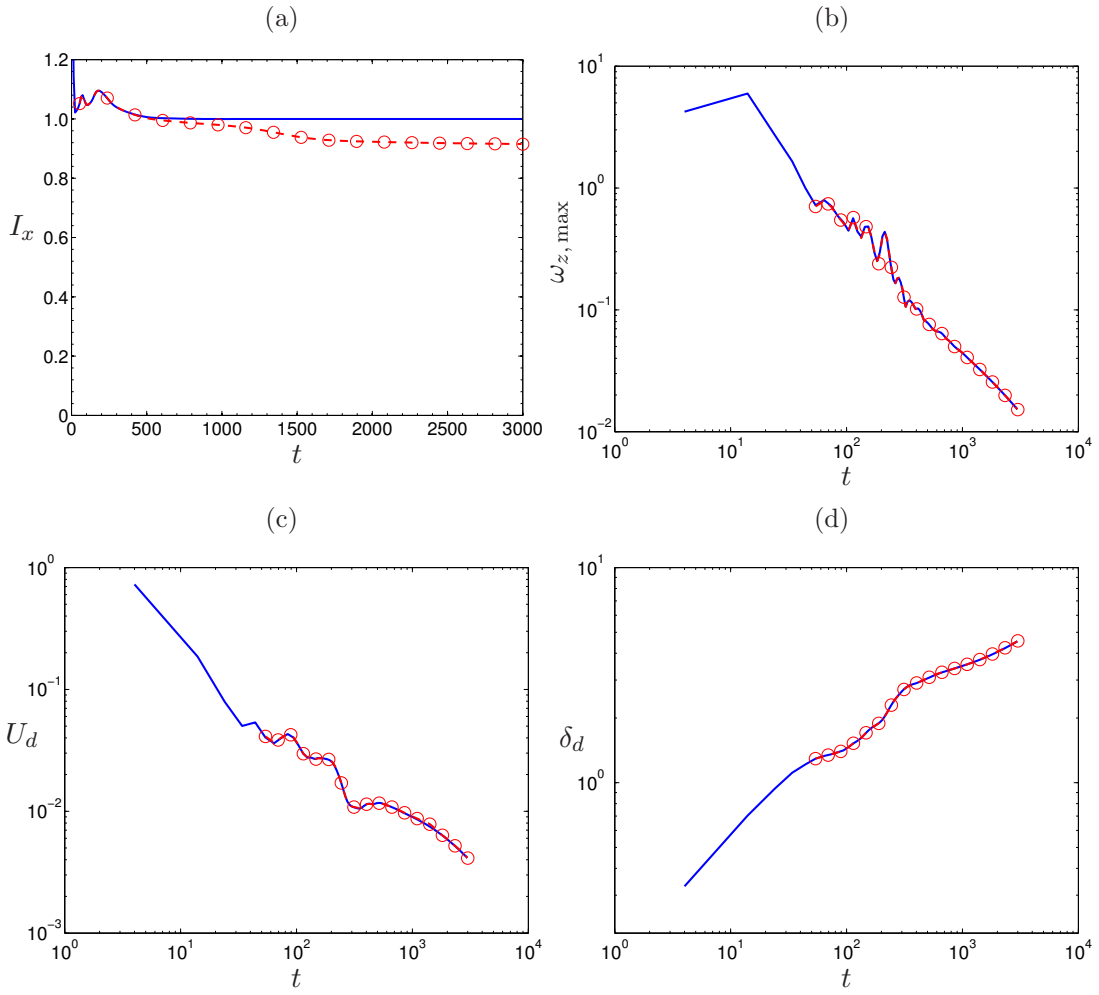

FIGURE 3.20: Comparison of dipole characteristics between Case JS3a and Case JS3aMF (at which a co-moving frame of reference attached to a vortex is employed): —— Case JS3a; --o-- Case JS3aMF. (a) Dipole impulse. (b) Maximum vertical vorticity at the free surface. (c) Dipole propagation velocity. (d) Dipole size. Case JS3aMF starts at $t = 50$.

to the loss of the wake shed from the vortex (Figure 3.20a), excellent agreement was found for $\omega_{z,\max}$ at the free surface and the others integral measures with the maximum relative difference of these quantities less than 2%.

3.5 Chapter Summary

In summary, this chapter validated the concept of applying an external body force to generate finite- and zero-momentum wakes, the implementation of an immersed boundary method, the domain-resizing approach and the PI controller used to adjust the reference-frame speed. The validation of the domain resizing and the moving reference frame attached to a vortex shows excellent agreement with the

baseline case. The test of the moving reference frame attached to a vortex also confirms that the wake shed from the vortex can be allowed to go out of the computational domain since it has very little effect on the dipole dynamics.

The body force seems to work well for generating two-dimensional large-scale vortical structures, such as a Kármán vortex street (induced by a single force) or an inverted Kármán vortex street (generated by a force doublet). However, when the magnitude of the drag is too large (i.e. $J_D/0.5\pi\sigma^2 U_\infty^2 > 1$), it would drive the velocity in the forcing region to become negative such that the energy flux ($E_i = u_i D_i$) in that region is increased. This is contradictory to the definition of drag force, which decreases the energy flux, and is thus unphysical. Moreover, when the body force is applied to a three-dimensional problem, the negative velocity provides fine-scale turbulence, which needs very fine grid resolutions to fully resolve it. Therefore, an immersed boundary method is implemented to emulate a virtual body, which imparts the drag to the flow, to avoid these problems.

An immersed boundary method used in this work is based on the concept of a proportional-integral (PI) feedback. We observed that the integral term can cause the stability issue when the gains are relatively large, such that only the proportional term will be used throughout this work. The proportional gain used is chosen to be related to the time step size to obtain the maximum gain (to make sure that the error from the feedback loop is close to zero) while maintaining stability. The validation shows that the accuracy of the IB approach used is reasonable although only one grid point was placed within the boundary layer of the virtual sphere.

Chapter 4

Evolution of Impulsively Generated Turbulent Patches: I. Self-Similar Dipole

In this chapter[1], the late-time formation of large-scale coherent structures generated from either an impulsive turbulent jet or an accelerating motion of a self-propelled body between non-deformable stress-free layers is reported. This chapter begins with a brief detail of the mathematical formulation used to study vortex dynamics in § 4.1. The late-time behaviour of a dipole induced by an impulsive turbulent jet is described in § 4.2.1, whilst the evolution of a turbulent patch generated by an accelerating motion of a self-propelled body is detailed in § 4.2.2. The conclusion of this study is given in § 4.3.

4.1 Mathematical Background

In order to determine the evolution of a submerged impulsive momentum source, the characteristics of the vortical structure, i.e. the dipole propagation velocity and the dipole size, are defined in terms of the integral parameters proposed for vortex-ring geometry by Saffman (1970). The dipole size δ_d and the dipole centroid $\boldsymbol{X}_d = (X_d, Y_d, Z_d)$ are defined using the first moment of enstrophy via

$$\delta_d = \frac{2}{\Omega} \int r \, |\omega|^2 \, \mathrm{d}x \, \mathrm{d}y \, \mathrm{d}z \,, \tag{4.1}$$

$$\boldsymbol{X}_d = \frac{1}{\Omega} \int \boldsymbol{x} \, |\omega|^2 \, \mathrm{d}x \, \mathrm{d}y \, \mathrm{d}z \,, \tag{4.2}$$

[1] Much of the material in this chapter has been presented in Rojanaratanangkule *et al.* (2012); see Appendix A.

where $r = \sqrt{y^2 + z^2}$, $|\omega|^2 = \omega_x^2 + \omega_y^2 + \omega_z^2$ and Ω is the total integrated enstrophy, defined as

$$\Omega = \int |\omega|^2 \, \mathrm{d}x \, \mathrm{d}y \, \mathrm{d}z \, . \tag{4.3}$$

Thus the dipole propagation velocity $\boldsymbol{U}_d = (U_d, V_d, W_d)$ can be obtained as

$$\boldsymbol{U}_d = \frac{\mathrm{d}\boldsymbol{X}_d}{\mathrm{d}t} \, . \tag{4.4}$$

We also define lateral ℓ_y and vertical ℓ_z length scales of the vortical structure as

$$\ell_y = \frac{2}{\Omega_y} \int_{\mathcal{H}} y \, |\omega|^2 \, \mathrm{d}x \, \mathrm{d}y \, \mathrm{d}z \, , \tag{4.5}$$

$$\ell_z = \frac{2}{\Omega_z} \int_{\mathcal{H}} z \, |\omega|^2 \, \mathrm{d}x \, \mathrm{d}y \, \mathrm{d}z \, , \tag{4.6}$$

where $\Omega_{y,\,z} = \int_{\mathcal{H}} |\omega|^2 \, \mathrm{d}x \, \mathrm{d}y \, \mathrm{d}z$ and the subscript $\mathcal{H}$ denotes that the integration is performed over the half-positive y- or z-domain. Note that Equations (4.1), (4.5) and (4.6) all require the origin of the y- and z-axes systems to be in the centre of the computational domain. These definitions give the dipole sizes that are roughly the distance between the vorticity extrema (maximum and minimum) of the dipole (Saffman, 1995).

The impulse $\boldsymbol{I} = (I_x, I_y, I_z)$ and the xy-plane circulation Γ of the dipole are also defined via their usual forms as

$$\boldsymbol{I} = \int \boldsymbol{x} \times \boldsymbol{\omega} \, \mathrm{d}x \, \mathrm{d}y \, \mathrm{d}z \, , \tag{4.7}$$

$$\Gamma = \int_{\mathcal{H}} \omega_z \, \mathrm{d}x \, \mathrm{d}y \, , \tag{4.8}$$

where $\boldsymbol{\omega} = (\omega_x, \omega_y, \omega_z)$.

4.2 Results

The evolution of the impulsively submerged momentum disturbance in the small-scale upper ocean, which is mimicked by stress-free top and bottom layers, is reported in this section. Two different types of momentum sources are chosen to investigate the self-similarity of a dipolar vortex created by: (i) an impulsive jet, and (ii) an accelerating motion of a self-propelled body.

Case	Domain depth (H^{a})	Re_j	Domain size	$N_x \times N_y \times N_z$
JD	Deep (4)	2000	$-5 \leqslant x \leqslant 25$, $-4 \leqslant y \leqslant 4$, $-4 \leqslant z \leqslant 4$	$960 \times 256 \times 256$
JS1	Shallow (0.5)	2000	$-5 \leqslant x \leqslant 25$, $-8 \leqslant y \leqslant 8$, $-0.5 \leqslant z \leqslant 0.5$	$960 \times 512 \times 32$
JS2	Shallow (0.5)	2000	$-5 \leqslant x \leqslant 55$, $-8 \leqslant y \leqslant 8$, $-0.5 \leqslant z \leqslant 0.5$	$1920 \times 512 \times 32$
JS3a	Shallow (0.5)	1250	$-5 \leqslant x \leqslant 55$, $-8 \leqslant y \leqslant 8$, $-0.5 \leqslant z \leqslant 0.5$	$1920 \times 512 \times 32$
JS3b[b]	Shallow (0.5)	1250	$-5 \leqslant x \leqslant 55$, $-8 \leqslant y \leqslant 8$, $-0.5 \leqslant z \leqslant 0.5$	$1920 \times 512 \times 32$
JS3LD	Shallow (0.5)	1250	$-5 \leqslant x \leqslant 55$, $-16 \leqslant y \leqslant 16$, $-0.5 \leqslant z \leqslant 0.5$	$1920 \times 1024 \times 32$
$\mathrm{JS3F}^{c}_{P1}$	Shallow (0.5)	1250	$-5 \leqslant x \leqslant 15$, $-3 \leqslant y \leqslant 3$, $-0.5 \leqslant z \leqslant 0.5$	$2560 \times 768 \times 128$
$\mathrm{JS3F}^{c}_{P2}$	Shallow (0.5)	1250	$-20 \leqslant x \leqslant 20$, $-6 \leqslant y \leqslant 6$, $-0.5 \leqslant z \leqslant 0.5$	$2560 \times 768 \times 64$
$\mathrm{JS3F}^{c}_{P3}$	Shallow (0.5)	1250	$-20 \leqslant x \leqslant 20$, $-12 \leqslant y \leqslant 12$, $-0.5 \leqslant z \leqslant 0.5$	$1280 \times 768 \times 32$
JS4	Shallow (0.5)	625	$-5 \leqslant x \leqslant 55$, $-8 \leqslant y \leqslant 8$, $-0.5 \leqslant z \leqslant 0.5$	$1920 \times 512 \times 32$

[a] H is the vertical distance from the centreline of the forcing to the free surface.
[b] This case is equivalent to Case JS3a except that low-level random noise is added to the initial condition.
[c] This case was initially computed using the finest grid resolution (labelled as P1) to prove the assumption made about the self-similarity of a dipole. The domain was resized twice at $t = 20$ (the beginning time of phase P2) and $t = 100$ (the beginning time of phase P3) to ensure that the lateral domain width is always at least four times bigger than the lateral size of the dipole. A co-moving frame of reference attached to a vortex was also employed for the simulation in phases P2 and P3 to fix the streamwise position of the vortical structure.

Table 4.1: Impulsive-jet-induced wake run parameters.

4.2.1 Jet-Induced Dipole

We first investigate the evolution and formation of a turbulent patch generated by an impulsive jet as a test case. The jet acts over a short time interval Δt_f with a forcing intensity J_T, distributed to the computational grid via the 3D Gaussian function with semi-width σ (cf. Equation 2.20). We choose $\Delta t_f = 4$ and $J_T = 1/4$, in units of $\mathcal{L}/\mathcal{U}$ and $\mathcal{U}^2\mathcal{L}^2$, respectively, with $\mathcal{L} = 8\sigma$ (such that $\mathcal{U} = J_T^{1/2}/4\sigma$). When the code described in § 2 is used to study the evolution of an impulsive jet, the boundary force from the virtual body B_i is not active. Recall that the calculations are carried out in a stationary frame of reference. To study the effect of a (non-deforming) free surface, we consider two distinct canonical flows: an impulsive jet in a deep layer and another in a shallow layer. These are simulated for a jet Reynolds number of 2000 based on the forcing intensity, i.e. $Re_j = J_T^{1/2}/\nu$. Free-slip boundary conditions are applied in the vertical direction for the jet in both deep and shallow layers, whilst the lateral direction is assumed to be periodic. The main difference between these two cases is that the vertical growth of the vortical structure created by the jet in a deep layer is not confined by the stress-free boundaries. The number of grid cells and the domain size for both cases, labelled as Cases JD and JS1 respectively, are given in Table 4.1. For the shallow-layer case, the forcing interval and the height of the computational domain were selected to correspond to the confinement number $C = 2$, for which the vortex dipole has been observed at the free surface (Voropayev *et al.*, 2007). Note that the lateral domain width L_y for all cases in this section was chosen to be at least 2.7 times larger than the maximum lateral size ℓ_y of the coherent structure (see Equation 4.5 above). That this value is sufficient is implied by the agreement of the dipole characteristics for Cases JS3a and JS3LD (which is equivalent to Case JS3a, apart from using L_y that is twice as large); see Figure 4.8. However, it should be noted that since the length of the initial momentum-containing region is relatively large, some of the pre-dipole dynamics may be influenced by the lateral domain size.

A check of the spatial resolution was performed by comparing the difference between the left- and right-hand sides of the volume-integrated instantaneous kinetic-energy equation, written such that (Pope, 2000)

$$\frac{\mathrm{d}K}{\mathrm{d}t} = -\epsilon_K - F_K + \int u_i T_i \,\mathrm{d}x\,\mathrm{d}y\,\mathrm{d}z\,, \tag{4.9}$$

where K is the volume-integrated kinetic energy, ϵ_K is the volume-integrated rate of kinetic energy dissipation and F_K is the net volume-integrated kinetic energy

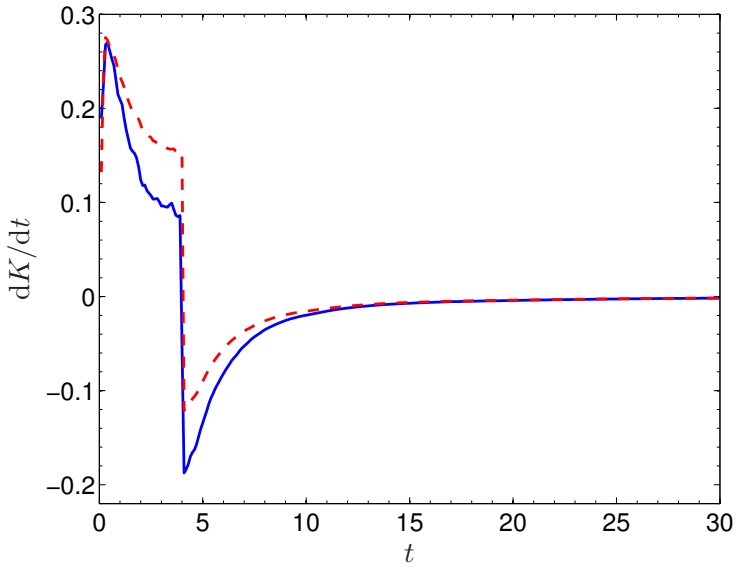

FIGURE 4.1: History of rate of change of volume-integrated kinetic energy $\mathrm{d}K/\mathrm{d}t$ for Case JD (jet in deep layer): —— $\mathrm{d}K/\mathrm{d}t$; ---- $-\epsilon_K - F_K + \int u_i T_i \,\mathrm{d}x\,\mathrm{d}y\,\mathrm{d}z$.

flux. This check indicates whether the grid is fine enough to resolve the smallest turbulence scales. History of the rate of change in the volume-integrated kinetic energy is provided in Figure 4.1. Although the smallest scales of the flow (i.e. the small-scale shear layers associated with, e.g., the boundary layer of the virtual body) generated by the jet impulse are not well captured before $t \approx 10$ (which leads to the differences between the left- and right-hand sides of Equation 4.9), after this time the flow is fully resolved. For all cases in this section except for Case JS3F, the maximum difference after 10 time units was less than 1.53% of the maximum value of $\mathrm{d}K/\mathrm{d}t$. The early under-resolution (when the calculation was effectively a large-eddy simulation in the context that the large turbulence scales are well resolved, while the small scales are not) corresponds to ambiguity of the details of the geometry of the wake-generating body. Since it appears that a vortex dipole is universal, i.e. a self-similar dipole can be obtained naturally from different initial conditions and paths (see Figure 4.8), a full resolution of the early-time small-scale turbulence (as used for Case JS3F; see Figure 4.7 below) is not necessary to obtain the correct long-time behaviour of the dipole.

The development of an impulsive jet in deep and shallow layers is shown in Figure 4.2 by the second invariant of the velocity gradient tensor Q (cf. Equation 3.21). After the relatively strong jet ($Re_j \gg 1$) is imparted into the fluid, it generates a vortical structure with azimuthal vorticity in the frontal region. The frontal region propagates away from its origin with speed U_d, which is half the local fluid velocity behind the front (Stern & Voropayev, 1984). Thus the jet fluid

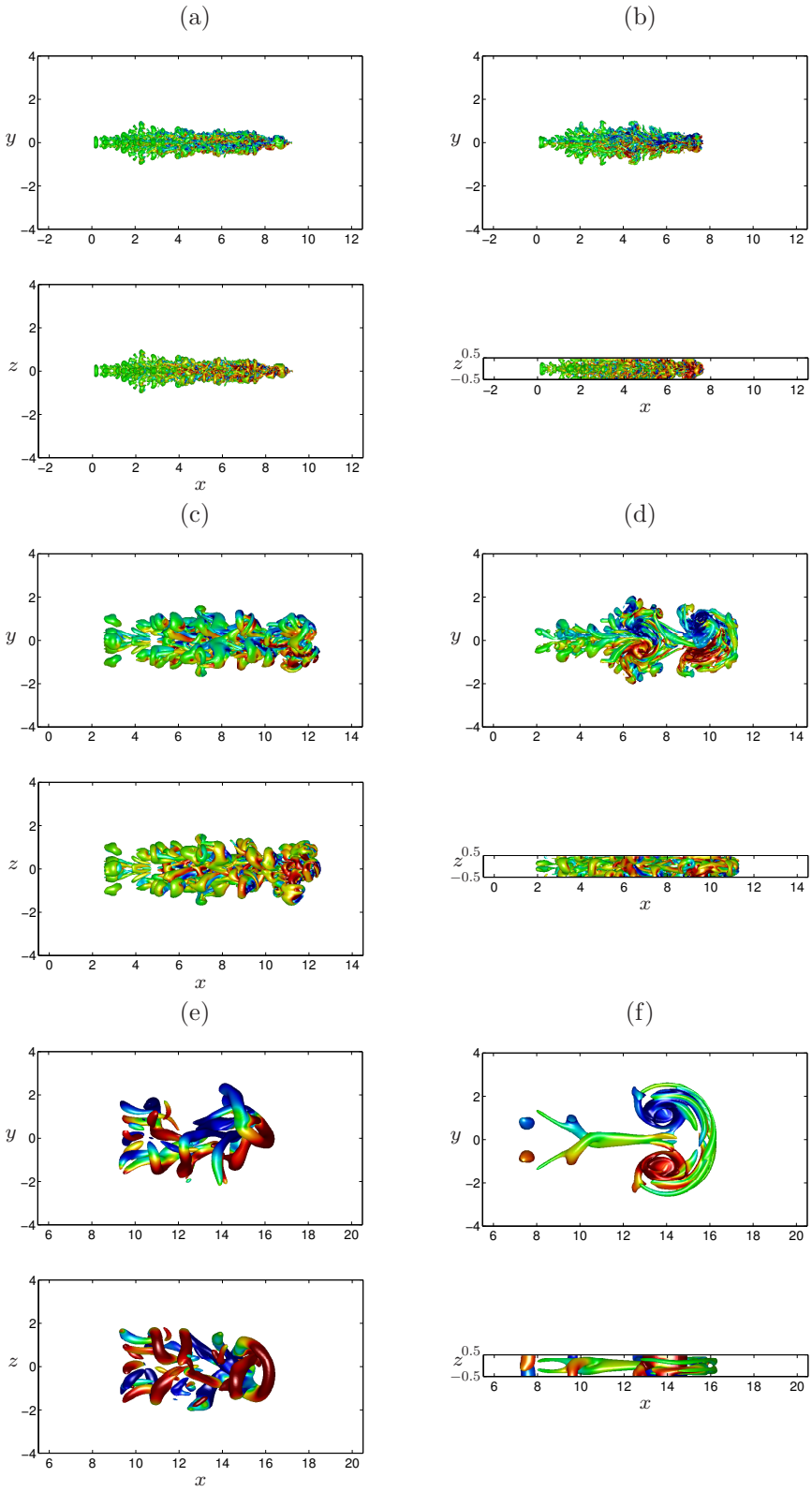

FIGURE 4.2: Top and side views (upper and lower part of each picture, respectively) of the vortical structure in (left) a deep layer (Case JD) and (right) a shallow layer (Case JS1) at $Re_j = 2000$ with level $Q = 2.5 \times 10^{-4}$: (a, b) $t = 10$, (c, d) $t = 50$, (e, f) $t = 250$. Isosurfaces of Q are coloured by vertical vorticity component ω_z.

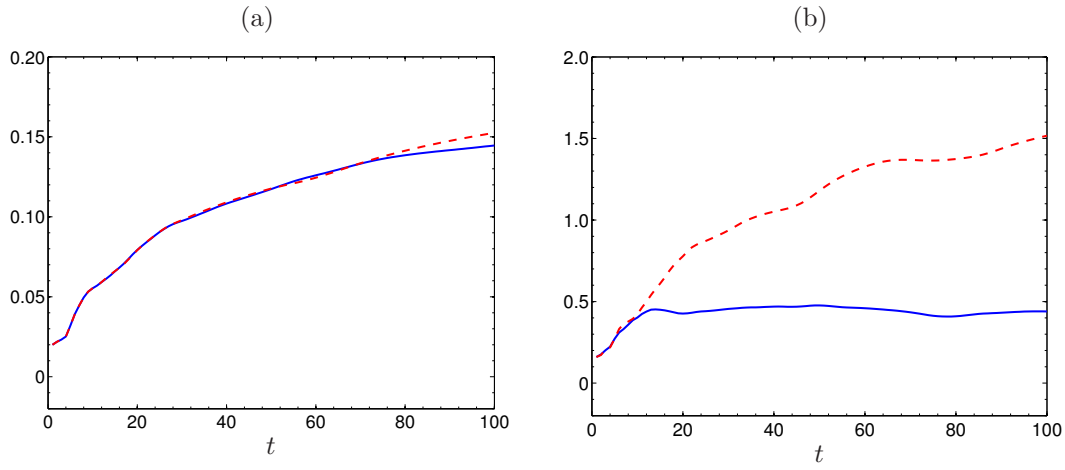

FIGURE 4.3: Histories of the lateral (ℓ_y) and vertical (ℓ_z) vortex sizes normalised by the domain depth for impulsive-jet flow in (a) a deep layer (Case JD) and (b) a shallow layer (Case JS1): ---- ℓ_y/h; —— ℓ_z/h. The domain depth h of Cases JD and JS1 is different.

merges into the vorticity front. At this stage, the ambient fluid is entrained in the frontal region, resulting in increasing the sizes of the coherent structure. When the vertical growth of the turbulent patch is not restricted (as for Case JD), the vertical and horizontal sizes of the patch increase, while decreasing the propagation speed to conserve momentum. With time the turbulent patch transforms into a toroidal vortex, as shown in Figure 4.2(e).

When the vertical growth of the turbulent patch is suppressed by the stress-free layers (Case JS1), the frontal region can only expand horizontally due to lateral entrainment (Figure 4.2d). A quasi-two-dimensional counter-rotating vortical structure eventually forms at late times, as illustrated in Figure 4.2(f). A plot of the lateral and vertical vortex sizes (ℓ_y, ℓ_z) versus time for Cases JD and JS1 is displayed in Figure 4.3. The agreement of the ℓ_y and ℓ_z histories for Case JD underlines the axisymmetric nature of the turbulent patch observed in Figures 4.2(a), 4.2(c) and 4.2(e), throughout the simulation (and indirectly validates the choices made for the sizes [and boundary condition] for the vertical and lateral domains). For Case JS1, the ℓ_y and ℓ_z histories imply that the turbulent patch is affected by the free-surface confinement for $t > 10$ (see Figures 4.2b, 4.2d, 4.2f).

The volume-integrated kinetic energy K of both cases is displayed in Figure 4.4. The kinetic energy of the vortical structure resulting from the jet in a deep layer decreases faster than the vortex suppressed by a free surface. This suggests that the toroidal vortex decays more rapidly than the vortex dipole, which can be confirmed by the theoretical scaling laws. Based on the ring and the dipole

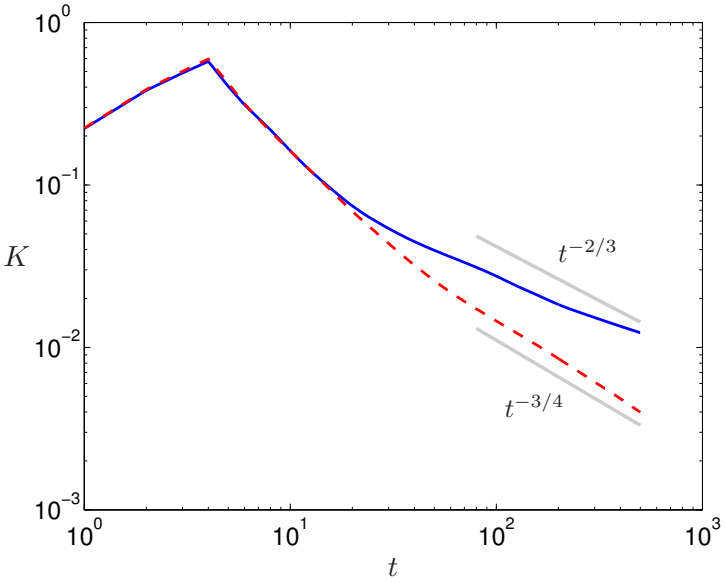

FIGURE 4.4: History of the volume-integrated kinetic energy K: ---- Case JD (deep layer); —— Case JS1 (shallow layer).

power laws, the volume-integrated kinetic energy of the ring and the dipole decreases with time as $t^{-3/4}$ and $t^{-2/3}$, respectively. Note that most of the kinetic energy of the flow is provided by the large-scale structures, hence the small scales observed from the ring at $t = 250$ (Figure 4.2e) do not have much effect on the kinetic energy.

Figure 4.5 illustrates the signature of the momentum disturbance caused by an impulsive jet. Initially, it can be seen from Figure 4.5(a) that the concentrated momentum disturbance at the free surface does not form a vortex dipole. With time, the patch propagates away from its origin, while increasing its horizontal size and decreasing its propagation speed, transforming into a quasi-planar dipole, as displayed in Figure 4.5(c). This is consistent with Voropayev *et al.*'s (2007) prediction that a dipole will be visible on the free surface when the confinement number (which for Case JS1 is 2) is greater than about 2.2.

To study the self-similar behaviour of the dipole at late time, the simulation at $Re_j = 2000$ was re-computed in a longer streamwise domain to avoid any effect of the outflow boundary condition. The length of the streamwise domain was increased from $L_x = 30$ to $L_x = 60$, with a corresponding increase in the number of grid cells to $N_x = 1920$. In addition, two more Reynolds numbers ($Re_j = 625$ and 1250) were considered (see Table 4.1). After the dipole is fully formed, Figure 4.6(a) shows that the intensity of the vertical vorticity at the free surface

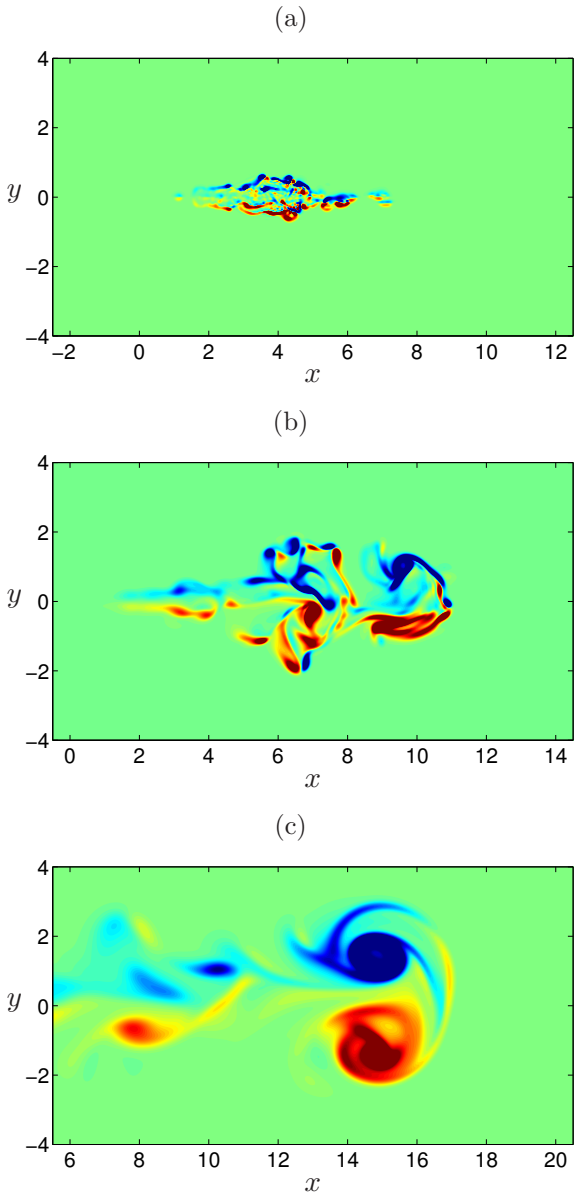

FIGURE 4.5: Contours of vorticity at the free surface showing the penetration of the momentum source created by an impulsive jet at $Re_j = 2000$ (Case JS1): (a) $t = 10$, (b) $t = 50$, (c) $t = 300$. Vorticity varies from $-0.2 \leq \omega_z / |\omega_z|_{\max} \leq 0.2$. Blue and red patches show negative and positive vertical vorticity, respectively.

reduces with time as $\omega_{z,\max} \sim t^{-1}$. The temporal evolution of the dipole propagation velocity U_d and the dipole size δ_d are illustrated in Figures 4.6(b) and 4.6(c), respectively. The dipole propagation speed decreases with time as $U_d \sim t^{-2/3}$, while its size increases as $\delta_d \sim t^{1/3}$. The power laws of the dipole in this simulation are the same as those in the previous measurements in a linearly stratified fluid (Voropayev *et al.*, 1991) and in a shallow layer (Sous *et al.*, 2004; Voropayev *et al.*, 2007). The dipole at a lower Reynolds number requires less time to achieve

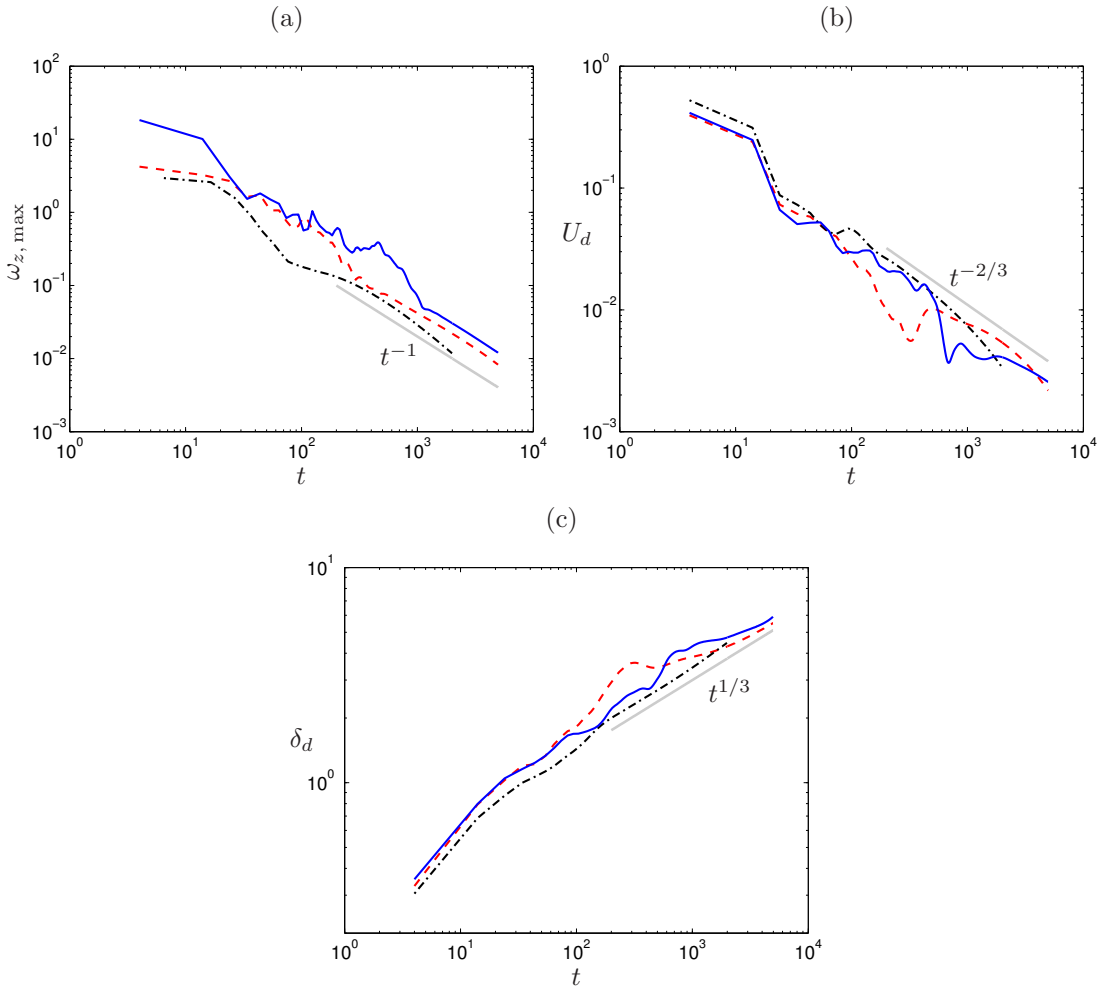

FIGURE 4.6: Histories of characteristics of jet-induced dipole: —— $Re_j = 2000$ (Case JS2); - - - - $Re_j = 1250$ (Case JS3a); -·-·- $Re_j = 625$ (Case JS4). (a) Maximum vertical vorticity at the free surface. (b) Dipole propagation velocity. (c) Dipole size.

power-law behaviour. For example, the dipole propagation velocity at $Re_j = 625$ starts to follow $t^{-2/3}$ at $t \approx 150$, while about 500 and 1800 time units are required for the dipoles at $Re_j = 1250$ and 2000, respectively. It should be noted that the theoretical scaling laws are based on the idea of the flow similarity and they satisfactorily describe the results of experiments and our numerical simulations at an intermediate asymptotic state only — but they are not useful in describing the whole flow evolution. Additionally, using only one realisation might not be enough to obtain close agreement between DNS results and the theoretical scaling laws, especially during the transformation process leading to a dipole. An ensemble of realisations is needed to address this point.

To investigate the sensitivity of the intermediate-time behaviour (about $200-500$ time units; see Figure 4.8) to small changes in the initial conditions (including

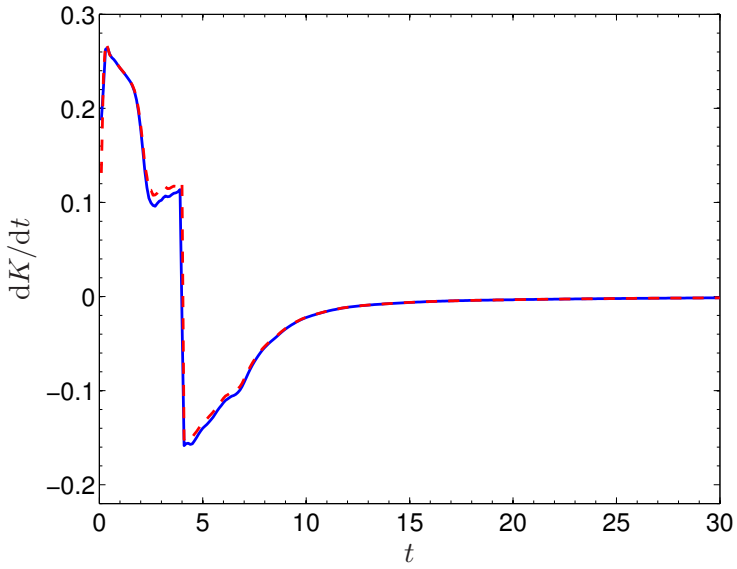

FIGURE 4.7: History of rate of change of volume-integrated kinetic energy $\mathrm{d}K/\mathrm{d}t$ for Case JS3F (jet in shallow layer using finest resolution): —— $\mathrm{d}K/\mathrm{d}t$; ---- $-\epsilon_K - F_K + \int u_i T_i \,\mathrm{d}x\,\mathrm{d}y\,\mathrm{d}z$.

the full resolution of the small-scale turbulence at the early time) and domain size, Case JS3a (jet-induced dipole at $Re_j = 1250$) was repeated, first in the same computational domain but with low-amplitude (maximum value of $10^{-8}\mathcal{U}$) random seeding (Case JS3b), second in a two times larger lateral domain (Case JS3LD), and third using many more grid points (Case JS3F). Note that the resolution for the first three cases is identical, while the resolution for Case JS3F during the forcing duration is four times finer, which results in the difference between $\mathrm{d}K/\mathrm{d}t$ and its RHS terms (see Equation 4.9) during the breakdown to turbulence ($t \approx 2.5$) being about 5% of the maximum value of $\mathrm{d}K/\mathrm{d}t$ as displayed in Figure 4.7. Histories of the dipole characteristics from these four cases are illustrated in Figure 4.8. Although their initial development is different, all four cases nevertheless converge to very similar dipole flows. This suggests that the dipole is a robust two-dimensional limit that is relatively insensitive to the path taken during its development.

4.2.2 Manoeuvring-Body Wake

We limit attention here to wakes in a shallow layer of same depth used for Cases JS1 – JS4. In order to capture the entire process of a late wake eddy behind a manoeuvring body, the simulation of a spatially developing wake needs to be performed in a very long domain, which is computationally inefficient. To overcome the problem, the simulation is split into two phases. The first phase of the

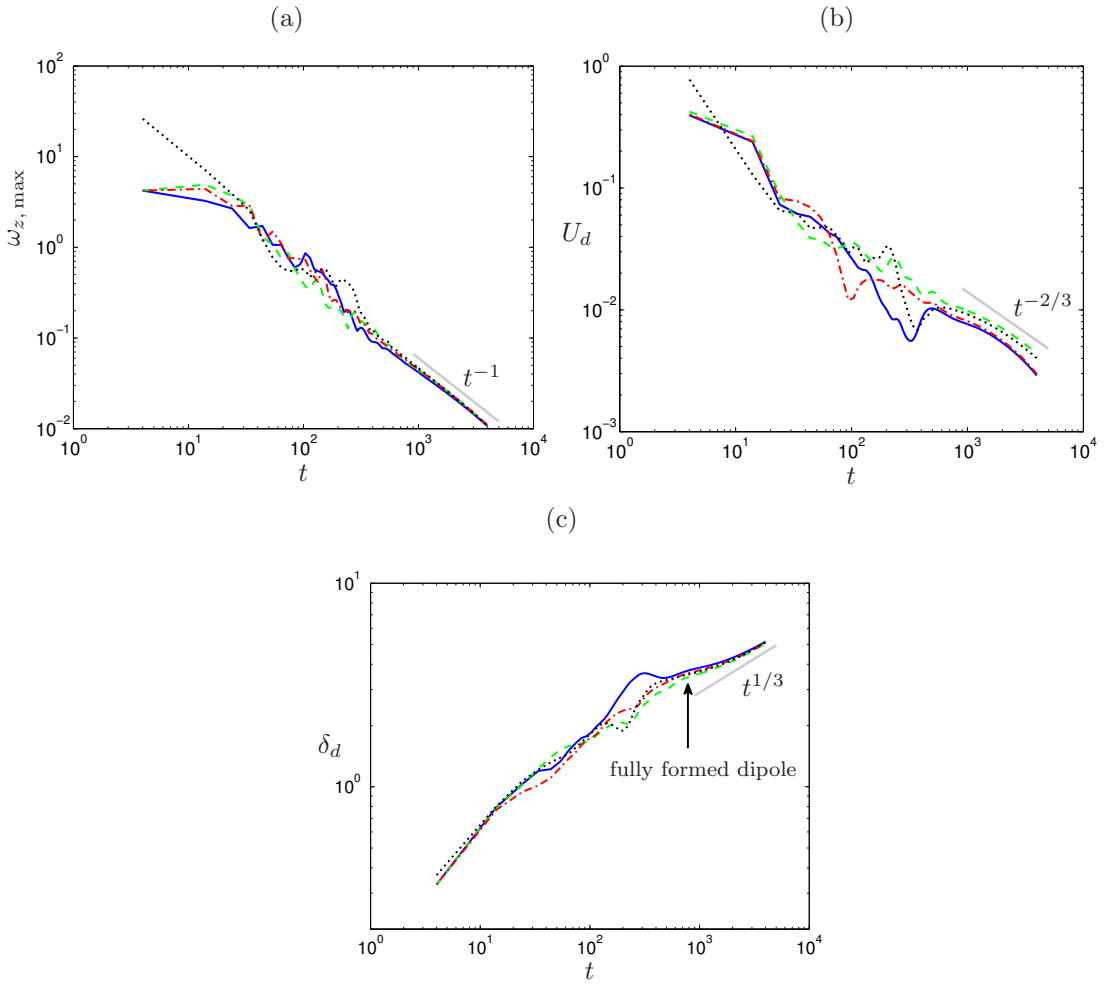

FIGURE 4.8: Histories of characteristics of jet-induced dipole at $Re_j = 1250$ from four different realisations: —— Case JS3a; -·-·- Case JS3b; - - - - Case JS3LD; ····· Case JS3F. (a) Maximum vertical vorticity at the free surface. (b) Dipole propagation velocity. (c) Dipole size.

simulation is concerned with the early-time behaviour of the wake, including both the near-field wake and the starting vortex, whilst the final phase contains only the late-time dipole behaviour (see § 4.2.2.2)

4.2.2.1 Early-Time Behaviour

We select a sphere with diameter D_b as the manoeuvring body. The Reynolds number based on the diameter and the terminal velocity $U_{b,t}$ of the sphere is $Re_b = U_{b,t}D_b/\nu = 826$. The simulation is performed in the domain given by $-5 \leqslant x \leqslant 30$, $-4 \leqslant y \leqslant 4$ and $-0.5 \leqslant z \leqslant 0.5$, with $2240 \times 512 \times 64$ grid cells. Here the reference length $\mathcal{L}$ is $2.5D_b$ and the reference velocity $\mathcal{U}$ is $2.05U_{b,t}$.

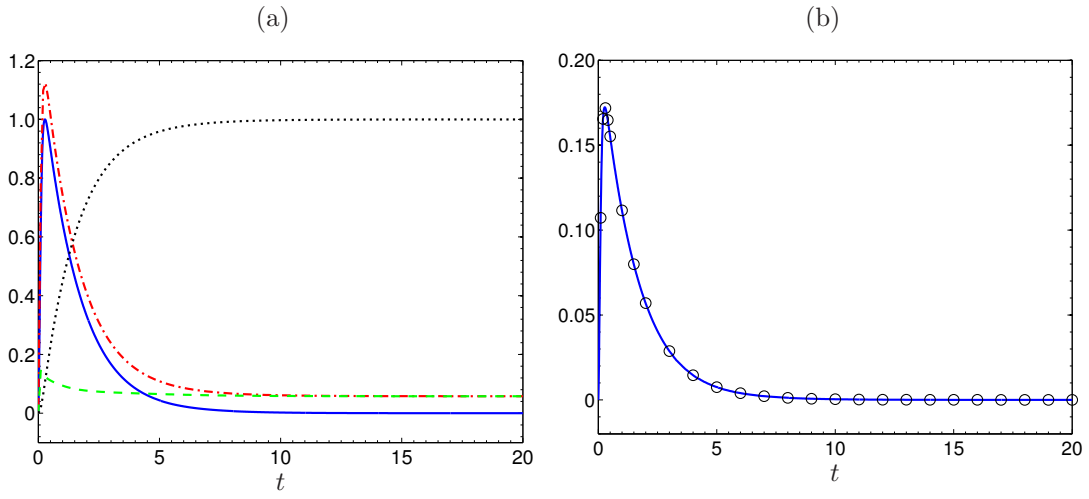

FIGURE 4.9: (a) Histories of the momentum flux, thrust, drag and speed of the body for manoeuvring-body wake: —— $F/F_{\max}$; -·-·- Thrust$/F_{\max}$; - - - - Drag$/F_{\max}$; ····· $U_b/U_{b,t}$. (b) History of the volume-integrated streamwise momentum flux: —— F_M; ○ $\int (-\partial u/\partial t + B_x + T_x - \mathrm{d}U_b/\mathrm{d}t)\,\mathrm{d}x\,\mathrm{d}y\,\mathrm{d}z$. The simulation parameters for this case are $Re_b = U_{b,t}D_b/\nu = 826$, $Re_j = J^{1/2}/\nu = 785$ and $C = J^{1/2}\Delta t_f/h^2 = 1.62$.

At $t = 0$, the body accelerates from rest. The forcing time scale in Equation (2.21) was chosen such that the density of the object associated with M_{eff} is 552 times that of the fluid. At this stage, the thrust is greater than the drag, leading to a momentum flux F being transported to the fluid. After some time, the body reaches and maintains its terminal speed. Histories of the momentum flux, the thrust, the drag and the velocity of the body are displayed in Figure 4.9(a). The jet Reynolds number Re_j and the confinement number C for this case are of 785 and 1.62, respectively. Note that we do not fully resolve the boundary layers of the sphere because we assume that the dipole will eventually become self-similar, such that the late-time characteristics of the dipole do not depend critically on the near-field wake (supported by the evidence in Figure 4.8) and only a momentum flux imparted into the fluid is important (compare comments following Equation 4.9, above). Thus, it is necessary to check if the net volume-integrated momentum flux F_M, which is the difference between the momentum, pressure and viscous fluxes at the inlet and outlet planes, is balanced by the forces added to the Navier–Stokes equations. The streamwise momentum balance in the non-inertial moving reference frame can be written such that

$$F_M = \int \left(-\frac{\partial u}{\partial t} + B_x + T_x - \frac{\mathrm{d}U_b}{\mathrm{d}t} \right) \mathrm{d}x\,\mathrm{d}y\,\mathrm{d}z\,. \tag{4.10}$$

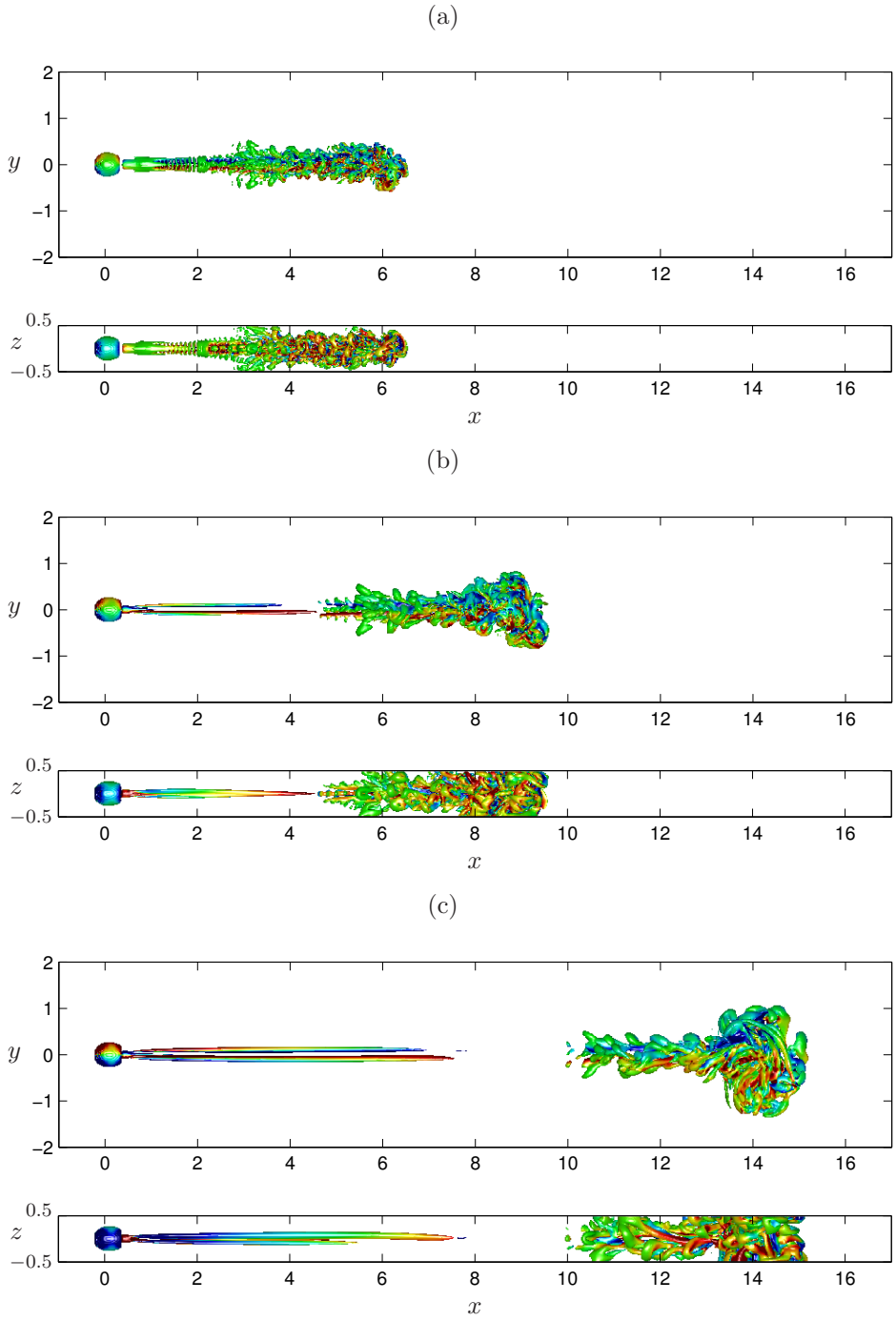

FIGURE 4.10: Top and side views (upper and lower part of the picture, respectively) of the vortical structure of a manoeuvring-body wake with level $Q = 2.5 \times 10^{-4}$: (a) $t = 5$, (b) $t = 10$, (c) $t = 20$. Isosurfaces of Q are coloured by vertical vorticity component ω_z.

A plot of the balance of the volume-integrated streamwise momentum flux versus time is displayed in Figure 4.9(b), showing good agreement between the flux terms F_M and the external forces. The difference is less than 0.11% of the maximum value of F_M during the acceleration period ($t < 9$) and less than 2×10^{-3}% when the body moves at its terminal speed. The adequacy of the spatial resolution was also checked in the same way as described in § 4.2.1. It was found that the error remaining after five time units was lower than 0.12% of the maximum value of $\mathrm{d}K/\mathrm{d}t$.

The second invariant of the velocity gradient tensor Q is again used to visualise the vortical structure of the manoeuvring-body wake, as displayed in Figure 4.10. It is found that a large-scale vortical structure, resulting from the acceleration of the body, appears in the late wake. The horizontal size of this vortical structure increases with time, due to lateral entrainment, while the vertical growth is restricted by the top and bottom free-slip walls. When the body is moving at its terminal velocity, a momentumless wake is observed in the near-field region. The zero-momentum wake decays very quickly without the formation of any coherent vortical structures. Note that the momentumless wake at the early time is still laminar, despite the relatively high Reynolds number, because the near-field wake is *convectively* unstable, i.e. has no strong reversed-flow region. Hence this flow compares to that over a streamlined body in which no flow separation occurs and it thus needs a very long time to become turbulent. If we were to use a high-intensity body force (i.e. $J_D/0.5\pi\sigma^2 U_{b,t}^2 > 1$) to represent the drag instead of the virtual body, the instability of the near-field wake would change to an absolute-type instability and would thus quickly break down to turbulence with a lot of small-scale eddies, which require very fine grid resolutions to fully resolve them. We did not follow that strategy, since the objective of this work is to study the characteristics of the late-wake eddy.

4.2.2.2 Late-Time Behaviour

After the body has reached its terminal velocity (at $t = 20$), the vorticity field was projected to a smaller computation domain using a window function f_w defined in Equation (2.23). The objective of using the window function is to remove a portion of the near-field wake, allowing computational resources to capture only the far-wake portion of the flow, as illustrated in Figure 4.11. Note that the removal of

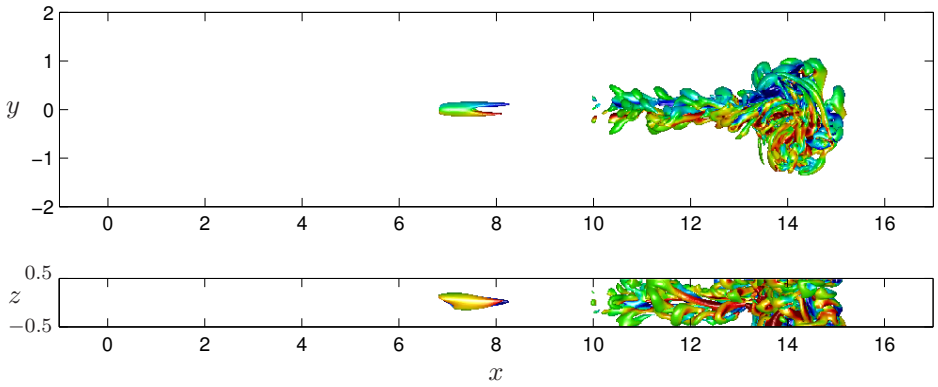

FIGURE 4.11: The projected vortical structure with the window function at $t = 20$: (Upper) top view, (Lower) side view.

the momentum source does not affect the formation and evolution of the late-wake eddy because negligible net momentum is imparted into the flow by the self-propelled body after it has achieved its terminal speed, when the drag is practically cancelled by the thrust. In order to obtain the new velocity field, we first solve the Poisson equation for the vector stream function $\boldsymbol{\psi} = (\psi_x, \psi_y, \psi_z)$ whose source term is the projected vorticity field $\boldsymbol{\omega} = (\omega_x, \omega_y, \omega_z)$ (cf. Equation 2.26). The new velocity field can then be obtained directly by taking the curl of the vector stream function as given in Equation (2.27). Full details of the domain-resizing approach including a corresponding set of boundary conditions are given in § 2.7.

The simulation in this phase is first carried out in a domain of size $4 \leqslant x \leqslant 24$, $-8 \leqslant y \leqslant 8$ and $-0.5 \leqslant z \leqslant 0.5$, with $1280 \times 1024 \times 64$ grid cells. Since the coherent structure propagates in the positive x-direction and could leave the domain if the domain length in that direction is not long enough, we employ a proportional-integral-derivative (PID) controller, described in § 2.8, to keep the vortical structure at a fixed streamwise location within the domain. This also significantly reduces the computational cost. The PID controller locates the vortex dipole to within 10^{-4} of the desired location by 20 time units. We allow the wake shed from the vortex to go out of the computational domain in the negative (outflow) x-direction (note that in the frame of reference attached to the vortex/dipole structure, the inflow boundary is at $x = 24$ and the outflow at $x = 4$), since its effect on the dipole dynamics is assumed to be negligible (supported by Figure 3.20). At very late time, high resolution is no longer required, since the global Reynolds number, based on the dipole translation speed U_d and the dipole size δ_d, decreases with time as $t^{-1/3}$ (Voropayev *et al.*, 1999), but the size of the domain has to be increased to capture the dipole as its lateral size increases. Thus, the computational domain was expanded at $t = 200$, with $-2 \leqslant x \leqslant 30$, $-16 \leqslant y \leqslant 16$ and

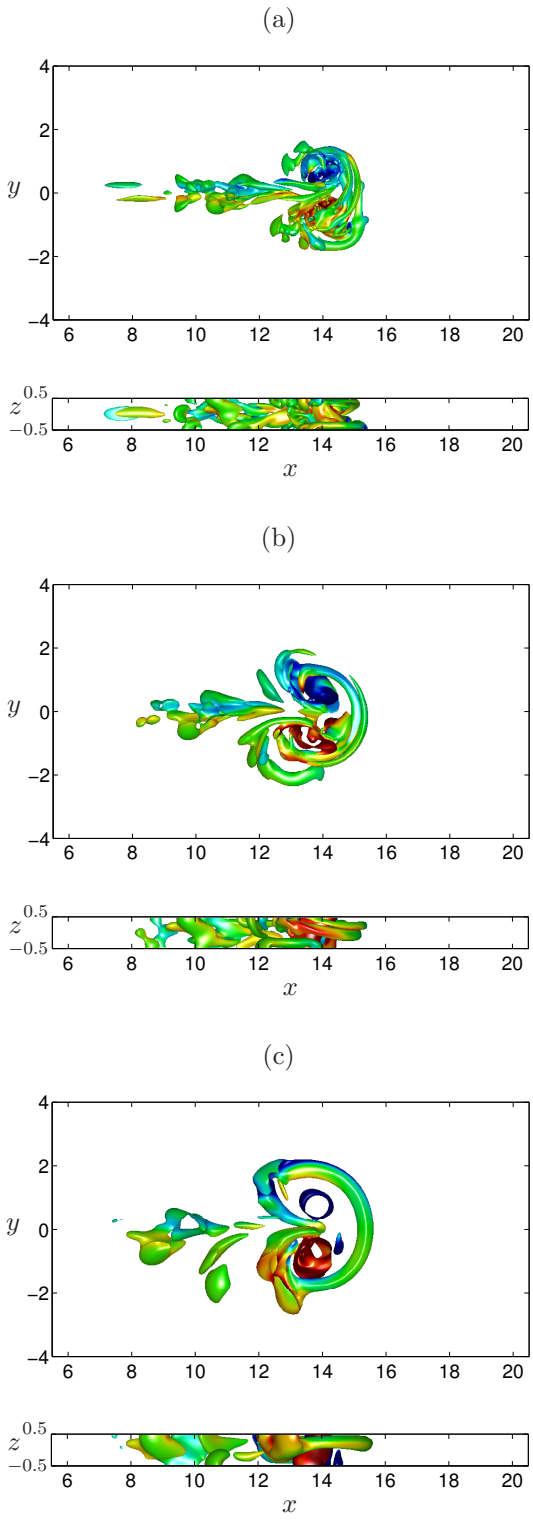

FIGURE 4.12: Top (upper) and side (lower) views of isosurfaces of Q showing the evolution of the vortical structure generated by the manoeuvring body at late time: (a) $t = 50$, (b) $t = 100$, (c) $t = 200$. Isosurfaces of Q are coloured by ω_z and the surface level is $Q = 2.5 \times 10^{-6}$.

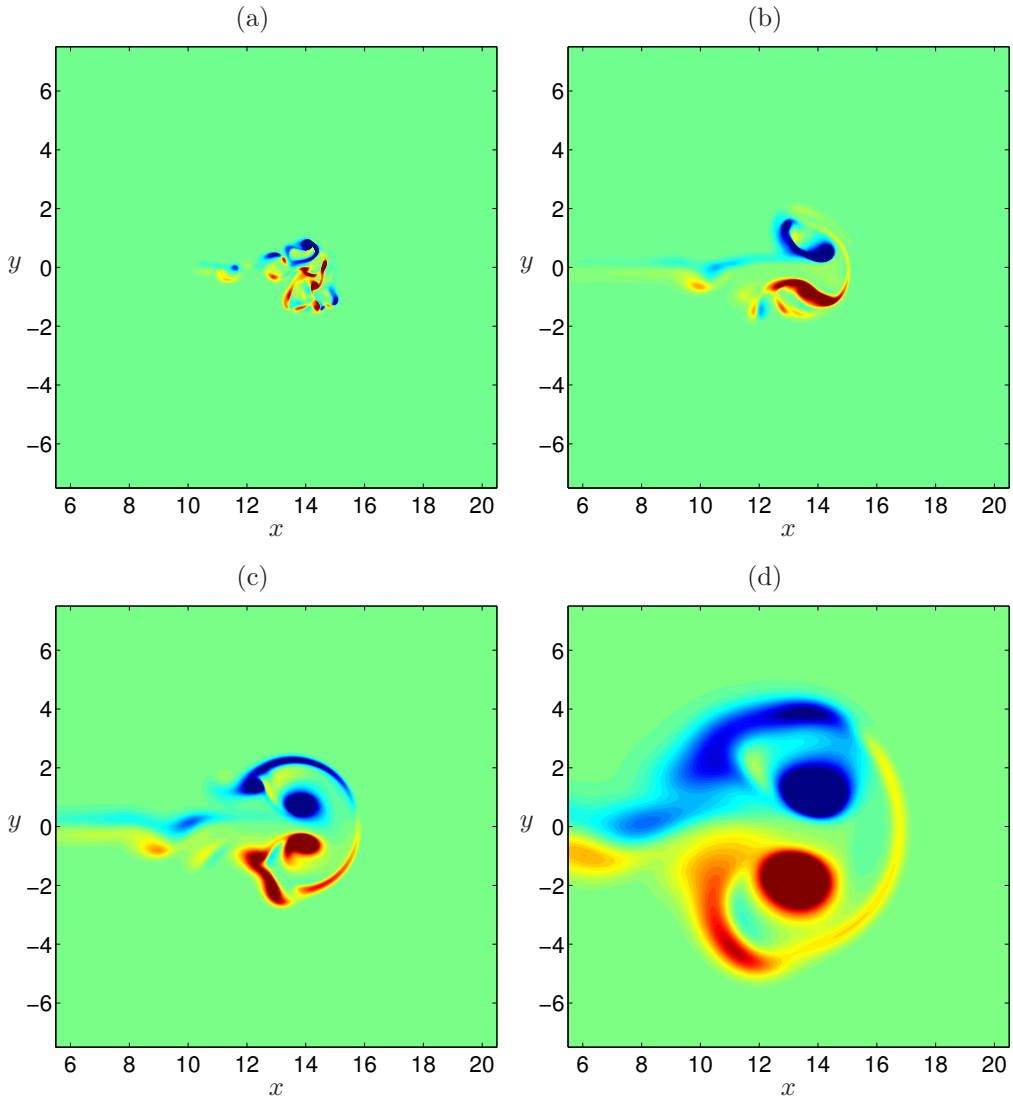

FIGURE 4.13: Contours of vertical vorticity ω_z at the free surface showing the penetration of a wake signature of a manoeuvring self-propelled body: (a) $t = 30$, (b) $t = 100$, (c) $t = 200$ (the computational domain is resized as described in § 2.7), (d) $t = 1000$. Vorticity varies from $-0.2 \leq \omega_z / |\omega_z|_{\max} \leq 0.2$. Blue and red patches show negative and positive vertical vorticity, respectively.

$-0.5 \leqslant z \leqslant 0.5$, and the resolution reduced to $1024 \times 1024 \times 32$ grid cells. It should be noted that during the entire simulation, the lateral domain width L_y is at least six times larger than the lateral size of the coherent structure created by the manoeuvring body.

The isosurfaces of Q displayed in Figure 4.12 show the evolution of the vortical structure. Only the horizontal size of the late-wake eddy can expand, yielding a coherent structure in the form of two patches of opposite-signed vortices, as shown in Figure 4.12(c). The evolution of the vortical structure at the free surface is displayed in Figure 4.13. Figure 4.13(a) shows that the momentum disturbance

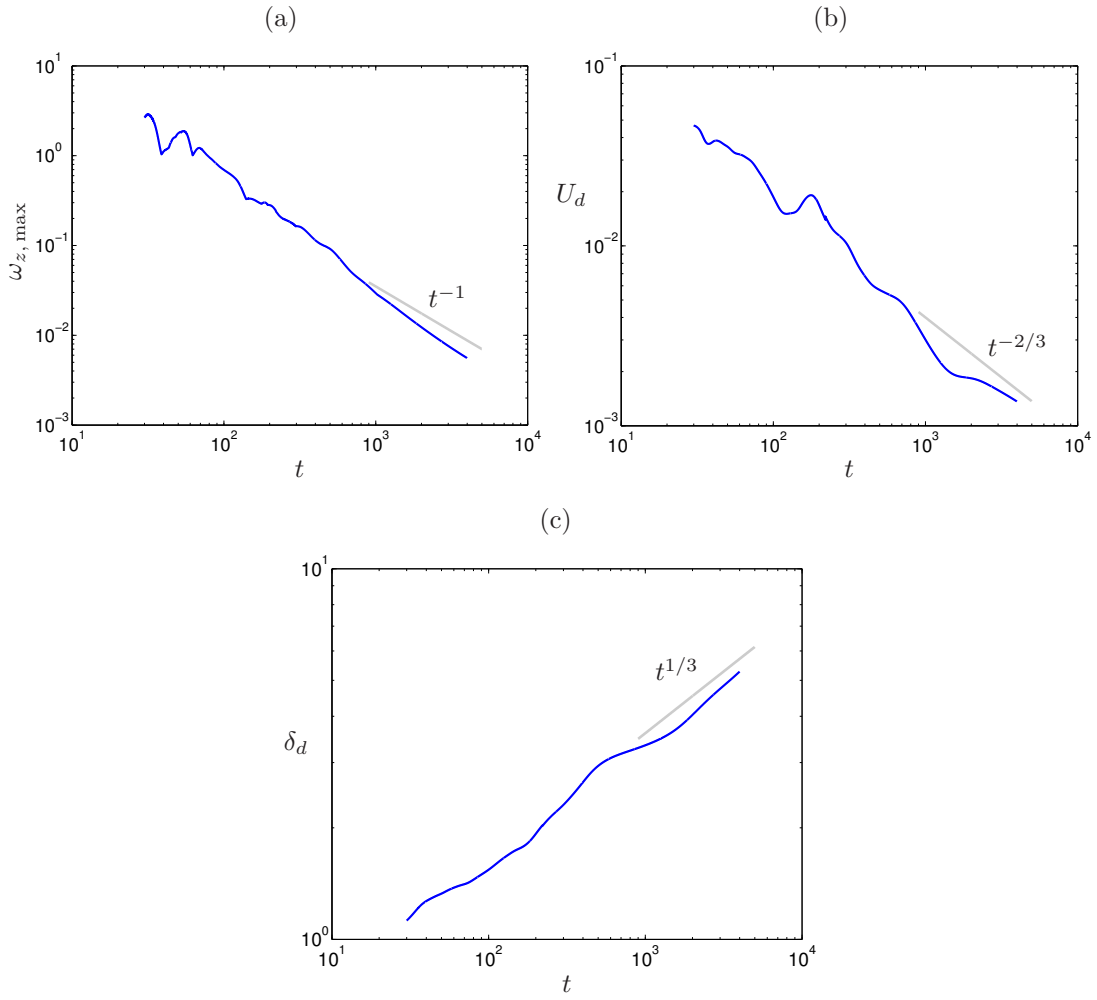

FIGURE 4.14: Histories of characteristics of dipole induced by manoeuvring body. (a) Maximum vertical vorticity at the free surface. (b) Dipole propagation velocity. (c) Dipole size. The computational domain is resized as described in § 2.7 at $t = 200$.

penetrates upward and produces its signature at the free surface at an early time. At this stage the wake signature is not yet in the form of a dipole. With time, the horizontal size of the surface eddy grows as it propagates away from the body, and the wake signature finally transforms into a vortex dipole (Figure 4.13c and 4.13d). The late-time coherent eddy generated by the manoeuvring body is similar to the jet-induced dipole.

The late-time characteristics of the dipole created by the accelerating motion of the body are given in Figure 4.14, along with the theoretical scaling laws. The comparison shows good agreement between the DNS and the power laws. These scaling laws are obtained with the assumption that the impulse of the dipole is conserved (Voropayev *et al.*, 1991, 2008). Based on this assumption, the decay of

Case	Re_j	C	A
JS2	2000	2.0	58.69
JS3a	1250	2.0	41.52
JS4	625	2.0	23.53
Manoeuvring body	785	1.62	21.28

TABLE 4.2: Values of A.

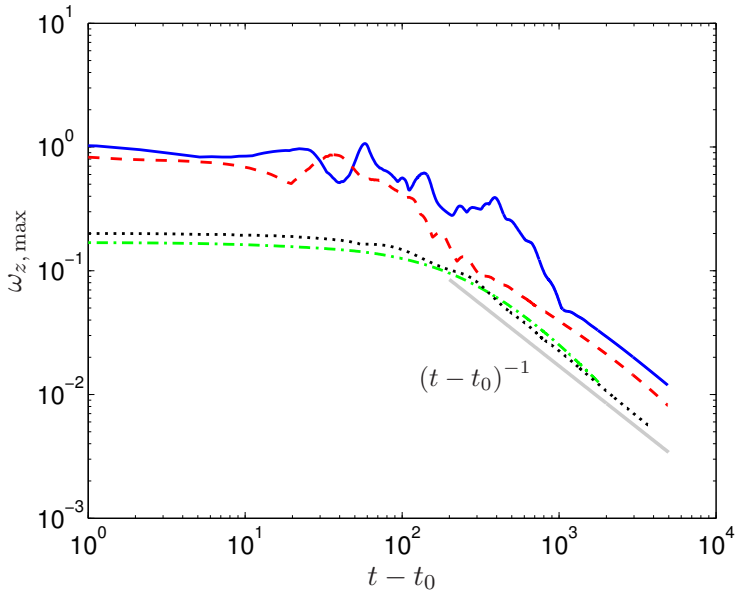

FIGURE 4.15: Histories of maximum vertical vorticity at the free surface: —— Case JS2 ($Re_j = 2000$); - - - - Case JS3a ($Re_j = 1250$); -·-·- Case JS4 ($Re_j = 625$); ····· Manoeuvring body ($Re_j = 785$).

the vertical vorticity is inversely proportional to time, with

$$\omega_{z,\max} = At^{-1}\,, \tag{4.11}$$

where A is an empirical constant. The constant A was determined experimentally by Voropayev *et al.* (2008) to be $A = 17$. In order to check whether or not this constant is universal, we compute A for all four cases (the jet-induced dipole at $Re_j = 625, 1250, 2000$ and the manoeuvring-body wake at $Re_j = 785$) by finding the slope and the virtual orgin of $\omega_{z,\max}^{-1} = (t - t_0)/A$. The resulting values of A from our data are given in Table 4.2, and a plot of $\omega_{z,\max}$ versus $(t-t_0)$ is displayed in Figure 4.15. Although the vorticity at large times decays in a similar manner as $1/(t - t_0)$, a Reynolds-number dependence is indicated, calling the universality of A into question. The consistency of the estimates for A seen in Figure 4.8(a), which shows the decay of $\omega_{z,\max}$ from different realisations, yields a unique value

of A for the jet-induced dipole at $Re_j = 1250$. Note that some difference between numerical and experimental values of A may be expected because the experiments (Voropayev *et al.*, 2008) were conducted in a stratified fluid, while a confined homogeneous fluid is used in the present simulations.

4.3 Chapter Summary

The formation and evolution of the large-scale coherent structure produced by both an impulsive jet and an accelerating self-propelled body have been examined using DNS. It is found that when the vortex is constrained by the stress-free top and bottom layers, a quasi-planar counter-rotating structure is formed. The vortex dipole persists for a longer time than a typical toroidal vortex. The characteristics of the dipole vortices induced by the presence of vertical confinement are similar to those in a stratified fluid. Qualitatively similar pancake-like vortices can be obtained via different initialisations, which support the assumptions made about the self-similarity of a dipole. The expected scaling laws are satisfied although the dipoles appear to possess a Reynolds-number dependence. Next chapter (§ 5) will investigate how the formation of the submerged momentum disturbances is affected by the thickness of the fluid domain. The ability of the confinement number to predict the effect of a submerged coherent vortex on, for example, the free surface will also be explored.

Chapter 5

Evolution of Impulsively Generated Turbulent Patches: II. Effect of Confinement Number

This chapter focuses on formulating the conditions under which an impulsively generated turbulent patch can be transformed to a pancake-like counter-rotating vortex which penetrates and produces a vortex dipole at the free surface and determining the relationship between the characteristics of a surface signature and the input parameters. We first explain the most important external dimensionless parameter, the confinement number, in § 5.1, followed in § 5.2 by the numerical approach employed to compute the evolution of the momentum patch. The simulation parameters are given in § 5.3. The major results from this study are reported in § 5.4. This chapter is then concluded with a brief summary in § 5.5.

5.1 Physical Meaning of the Confinement Number

It was found that the condition under which a three-dimensional vortex can be altered to a vortex dipole and produces a signature at the free surface depends only on the dimensionless parameter called the *confinement number* C (Sous *et al.*, 2004, 2005; Voropayev *et al.*, 2007). The confinement number was first obtained by performing dimensional analysis (Sous *et al.*, 2004) and is defined as

$$C = \frac{J^{1/2}\Delta t_f}{h^2}\,, \tag{5.1}$$

where J is the forcing intensity, Δt_f is the forcing duration and h is the depth of the fluid domain. Voropayev *et al.* (2007) estimated the critical value of the confinement number, and assuming the momentum was provided by a round turbulent jet (the eddy viscosity and the jet's half width provided in Schlichting, 1979) as shown below.

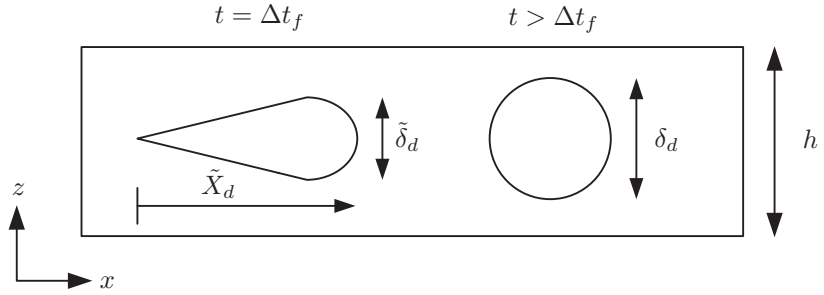

FIGURE 5.1: Schematic of side view of (left) a conical turbulent jet at $t = \Delta t_f$, and (right) a round turbulent patch at $t > \Delta t_f$ (adapted from Voropayev *et al.*, 2007).

After the relatively strong jet ($Re_j \gg 1$) is imparted into the fluid, it generates a conical vortical structure with a spherical vorticity of diameter $\tilde{\delta}_d$, which will grow with time, in the frontal region (see Figure 5.1). The frontal region propagates away from its origin with speed $\tilde{U}$, which is half the local fluid velocity in the trailing jet u_j, behind the front (Stern & Voropayev, 1984)

$$\tilde{U} = \frac{\mathrm{d}\tilde{X}_d}{\mathrm{d}t} = \frac{1}{2} u_j \,, \tag{5.2}$$

where $\tilde{X}_d$ is the distance from the origin. For a circular turbulent jet, the velocity of the jet can be estimated from the eddy viscosity ϵ_o (Schlichting, 1979) as

$$u_j\left(\xi\right) = \frac{3J}{8\pi\epsilon_o \tilde{X}_d} \frac{1}{\left(1 + \frac{1}{4}\xi^2\right)^2} \,, \tag{5.3}$$

where ξ is the radial distance normalised by the jet's half-width $r_{1/2}$. The eddy viscosity is parameterised as $\epsilon_o = 0.0161 J^{1/2}$ (Schlichting, 1979). Thus the jet maximum velocity that occurs at the centreline ($\xi = 0$) is

$$u_j \approx 7.4141 \frac{J^{1/2}}{\tilde{X}_d} \,. \tag{5.4}$$

Substituting u_j into Equation (5.2) and integrating it over the period of the forcing, the distance $\tilde{X}_d$ of the vorticity front at the end of the forcing action ($t = \Delta t_f$) is

$$\int \tilde{X}_d \, \mathrm{d}\tilde{X}_d = \frac{1}{2} \int_0^{\Delta t_f} 7.4141 \, J^{1/2} \, \mathrm{d}t \,,$$

$$\tilde{X}_d \approx 2.7229 \, J^{1/4} \Delta t_f^{1/2} \,. \tag{5.5}$$

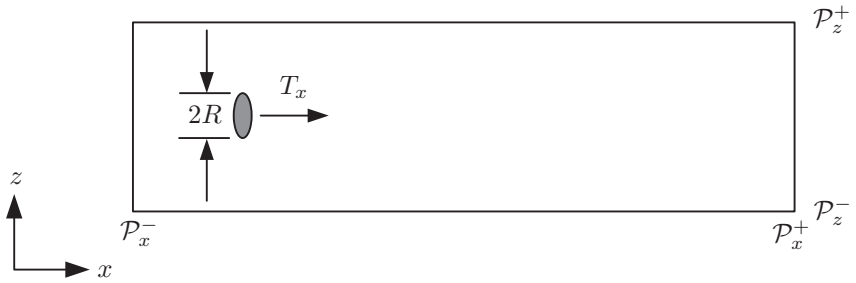

FIGURE 5.2: Schematic of computational domain for a disk-like body force during the forcing period ($t \leqslant \Delta t_f$).

The diameter of the vorticity front $\tilde{\delta}_d$ can be approximated from the half-width of a self-similar turbulent jet, with $r_{1/2} = 0.0848\tilde{X}_d$ (Schlichting, 1979), as

$$\tilde{\delta}_d \approx 2\, r_{1/2} \approx 0.4618\, J^{1/4}\Delta t_f^{1/2}\,. \tag{5.6}$$

After $t > \Delta t_f$, the trailing jet of the conical structure continues to merge into the frontal region (recall that u_j is two times faster than $\tilde{U}$), leading to a nearly spherical turbulent patch of diameter δ_d, which is usually bigger than $\tilde{\delta}_d$ (cf. Figure 5.1). Since a change in the volume of the vortex during this transformation is assumed to be negligible (Voropayev *et al.*, 2007), the size of the patch can be obtained by equating the volume of the patch ($V_p = \pi\delta_d^3/6$) and the conical vortex ($V_c = \pi\tilde{\delta}_d^2\tilde{X}_d/12$),

$$\delta_d \approx 1.4339\,\tilde{\delta}_d \approx 0.6622\, J^{1/4}\Delta t_f^{1/2}\,. \tag{5.7}$$

From this estimation, one can expect that a large-eddy signature will appear at a free surface when $\delta_d \geqslant h$. The critical value of the confinement number C_{cr} can then be obtained by combining the above approximations with the definition of the confinement number and setting $\delta_d = h$, such that

$$\begin{aligned}
\frac{0.6622\, J^{1/4}\Delta t_f^{1/2}}{h} &= 1\,,\\
\frac{J^{1/2}\Delta t_f}{h^2} &= \frac{1^2}{0.6622^2}\,,\\
C_{\mathrm{cr}} &\approx 2.3\,.
\end{aligned} \tag{5.8}$$

Based on this estimation, it can be seen that only the forcing intensity J and forcing period Δt_f control the initial shapes (horizontal length X_d and its size δ_d) of the turbulent patch. Voropayev *et al.* (2007) thus suggested that (the square root of) the confinement number can be interpreted as the ratio of the initial

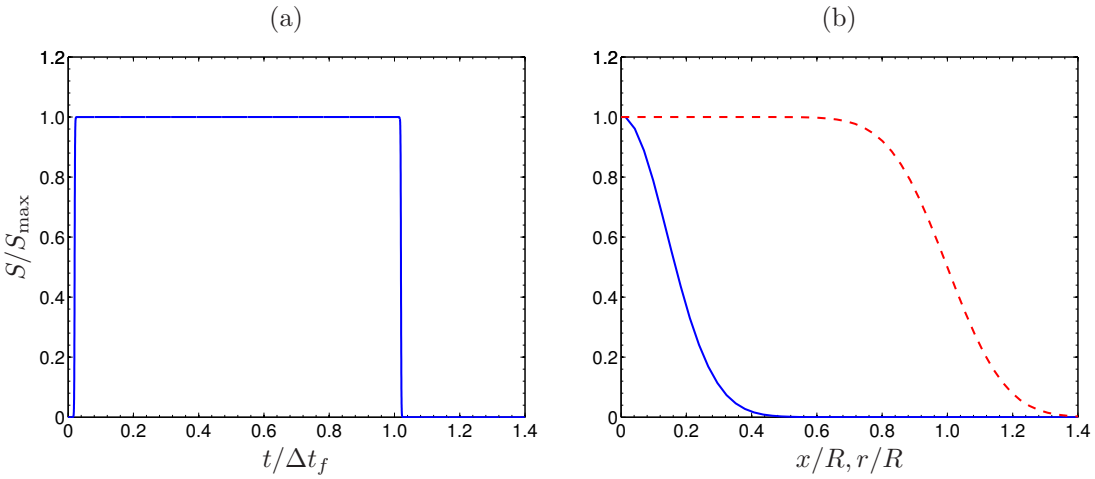

FIGURE 5.3: (a) Time evolution $S(t)$ of the body force. (b) Distribution of the body force in axial $G(x)$ and radial $H(r)$ directions: —— $G/G_{\max}$; ---- $H/H_{\max}$.

size of the patch, defined by J and Δt_f, to the depth of the fluid domain. Once the given initial size is bigger than the domain depth, the vertical growth of the turbulent patch is restricted by the flow geometry and the patch may be altered to a quasi-two-dimensional counter-rotating vortical structure.

5.2 Numerical Approach

The numerical approach used in this chapter is similar to that described in § 2 except that only a stationary impulsive momentum source (an impulsive turbulent jet) is chosen to generate a turbulent patch since it has been shown in § 4 that qualitatively identical quasi-2D counter-rotating coherent structures can be obtained from using either moving (a manoeuvring body) or stationary (an impulsive jet) momentum sources. Hence, the boundary force from a virtual body B_i is not active and the calculations are first performed in a stationary frame of reference during the forcing period ($t \leqslant \Delta t_f$), as illustrated in Figure 5.2. Stress-free boundary conditions are applied in the vertical (z) direction to represent a non-deformable free surface, while periodic boundary conditions are employed in the lateral (y) direction.

Once $t > \Delta t_f$, a co-moving frame of reference attached to a vortex, described in § 2.8, is employed to maintain the position of the turbulent patch (see Figure 2.2). The computational domain is increased several times as the flow develops to accommodate the growth in the sizes of the momentum patch. In brief, the domain length is expanded in the streamwise (x) and lateral (y) directions, while

the resolution in all three directions is reduced to decrease the net computational cost. The reduction in the grid resolution is done without the loss of accuracy, since the Reynolds number of the flow, based on the vortex translation speed U_d and its size δ_d, decreases with time. Details of the domain-resizing technique and its validation are respectively provided in § 2.7 and § 3.3.

An impulsive momentum source $\boldsymbol{T} = (T_x, 0, 0)$, applied directly to the Navier–Stokes equations, is modelled as a thin axisymmetric disk (e.g. see Mohseni *et al.*, 2001) with radius R and has the form

$$T_x(x, y, z, t) = JS(t)G(x)H(r)\,, \tag{5.9}$$

where J is the forcing intensity.

A step function, whose distribution is illustrated in Figure 5.3(a), is used to represent the time evolution $S(t)$ of the body force as

$$S(t) = \frac{1}{2}\left[\tanh\left(\sigma_t\left\{\frac{1}{2}\Delta t_f - \left|t - \frac{1}{2}\Delta t_f - C_t\right|\right\}\right) + 1\right]\,, \tag{5.10}$$

where $C_t = 0.02$ is a time offset to ensure that $S\,(0) = 0$, and $\sigma_t = 16/C_t$ is an inverse of a time scale that controls the smoothness and is set to be compatible with the choice of C_t. The body force is centred at $(x, y, z) = 0$. The functions $G(x)$ and $H(r)$ respectively control the spatial variation of the body force in the streamwise (x) and radial ($r = \sqrt{y^2 + z^2}$) directions and are defined as

$$G(x) = \frac{1}{\sigma_x \pi^{1/2}} \exp\left[-\frac{x^2}{\sigma_x^2}\right]\,, \tag{5.11}$$

$$H(r) = \frac{1}{2C_r}\,\mathrm{erfc}\left(\frac{r - R'}{\sigma_r}\right)\,, \tag{5.12}$$

where $C_r = 0.5R\sigma_r\pi^{1/2}e^{-R^2/\sigma_r^2} + 0.25\pi[\mathrm{erf}(R/\sigma_r) + 1][\sigma_r^2 + 2R^2]$ is a normalisation constant chosen to ensure unit total force; the smoothing coefficients σ_x and σ_r are assigned the value of $0.2R$, which results in the distribution displayed in Figure 5.3(b). Note that Equations (5.11) and (5.12) are determined in such a way that J is equal to the volume integrated force ($J = \int T_x\,\mathrm{d}x\,\mathrm{d}y\,\mathrm{d}z$), such that the total impulse I can be obtained as

$$I = \int J\,\mathrm{d}t = J\Delta t_f\,. \tag{5.13}$$

Azimuthal instability is introduced by adding azimuthal perturbation $g(\theta)$ with amplitude $\varsigma = 5 \times 10^{-3}$ to the body-force radius R, such that

$$R'(\theta) \leftarrow R\left[1 + \varsigma g(\theta)\right] . \tag{5.14}$$

We follow Shariff *et al.* (1994) and Archer *et al.* (2008) by using $g(\theta)$ as the sum of the first 32 Fourier modes, written as

$$g(\theta) = \sum_{n=1}^{32} A_n \cos(n\theta) + B_n \sin(n\theta) , \tag{5.15}$$

where A_n and B_n are random numbers with $A_n^2 + B_n^2 = 1$, and θ is the azimuthal coordinate. Note that the level of the azimuthal perturbation used is higher than that from the numerical error that excites only some particular azimuthal modes. Therefore, the first 32 azimuthal modes each have approximately the same initial level of energy, allowing the flow to naturally select the most dominant azimuthal mode. When the value of ς is too large (greater than about 10^{-2} for this case), the transition to turbulence of a momentum patch bypasses a linear instability stage. The patch thus becomes turbulent only by a nonlinear instability process.

5.3 Simulation Parameters

Numerical simulations were designed to study the effect of the confinement number C on the formation of the turbulent patch by varying the forcing duration Δt_f, which results in a range of C from 0.2 – 6.0, as listed in Table 5.1. The forcing intensity and the domain depth were fixed at $J = 1/16$ and $h = 0.3$ (corresponding to $h/2R = 6$), in units of $\mathcal{U}^2\mathcal{L}^2$ and $\mathcal{L}$, respectively, with $\mathcal{L} = 40R$ and $\mathcal{U} = J^{1/2}/10R$. For all cases, the simulations were conducted at $Re_j = J^{1/2}/\nu = 1250$ and used the time step Δt that provides the maximum Courant–Friedrichs–Lewy (CFL) number, based on local maximum velocity and grid size, well below 0.2. During the forcing duration, the simulations were performed in the finest grid resolution (phase one, labelled as superscript 1 in Table 5.1) to ensure that the smallest scales of the flow are fully resolved (supported by the evidence in Figure 5.4 below). A few times after the forcing stopped, the computational domain was resized and the simulations continued into phase two and phase three, in which a co-moving frame of reference attached to the vortex structure was employed to lock the streamwise position of the turbulent patch. It should be noted that the lateral domain width L_y for the simulations in all phases of each

Case	C	Δt_f	Fn	Domain size						$N_x \times N_y \times N_z$	$\hat{t}/\Delta t_f$
				x_s	x_e	y_s	y_e	z_s	z_e		
C0p2^1	0.2	0.072	8.1	−0.5	1.0	−0.2	0.2	−0.15	0.15	$960 \times 256 \times 192$	4.17
C0p2^2	0.2	0.072	8.1	−1.0	1.6	−0.6	0.6	−0.15	0.15	$832 \times 384 \times 128$	50.0
C0p5^1	0.5	0.18	20.3	−0.5	1.5	−0.3	0.3	−0.15	0.15	$1280 \times 384 \times 192$	4.0
C0p5^2	0.5	0.18	20.3	−1.0	2.4	−0.8	0.8	−0.15	0.15	$1088 \times 512 \times 128$	10.0
C0p5^3	0.5	0.18	20.3	−2.0	3.0	−1.6	1.6	−0.15	0.15	$832 \times 512 \times 64$	50.0
C1p0^1	1.0	0.36	40.6	−0.5	2.0	−0.4	0.4	−0.15	0.15	$1600 \times 512 \times 192$	2.5
C1p0^2	1.0	0.36	40.6	−1.0	3.0	−1.0	1.0	−0.15	0.15	$1280 \times 640 \times 128$	8.34
C1p0^3	1.0	0.36	40.6	−2.0	4.0	−2.4	2.4	−0.15	0.15	$960 \times 768 \times 64$	50.0
C1p5^1	1.5	0.54	60.9	−0.5	2.5	−0.5	0.5	−0.15	0.15	$1920 \times 640 \times 192$	2.22
C1p5^2	1.5	0.54	60.9	−1.0	3.6	−1.2	1.2	−0.15	0.15	$1472 \times 768 \times 128$	6.67
C1p5^3	1.5	0.54	60.9	−2.0	4.8	−2.8	2.8	−0.15	0.15	$1088 \times 896 \times 64$	50.0
C2p0^1	2.0	0.72	81.2	−0.5	2.9	−0.6	0.6	−0.15	0.15	$2176 \times 768 \times 192$	2.08
C2p0^2	2.0	0.72	81.2	−1.0	3.6	−1.4	1.4	−0.15	0.15	$1472 \times 896 \times 128$	6.25
C2p0^3	2.0	0.72	81.2	−2.0	4.8	−3.2	3.2	−0.15	0.15	$1088 \times 1024 \times 64$	50.0
C2p5^1	2.5	0.9	101.6	−0.5	3.1	−0.65	0.65	−0.15	0.15	$2304 \times 832 \times 192$	2.0
C2p5^2	2.5	0.9	101.6	−1.0	4.0	−1.4	1.4	−0.15	0.15	$1600 \times 896 \times 128$	6.0
C2p5^3	2.5	0.9	101.6	−2.0	5.2	−3.2	3.2	−0.15	0.15	$1152 \times 1024 \times 64$	50.0
C4p0^1	4.0	1.44	162.5	−0.5	4.0	−0.8	0.8	−0.15	0.15	$2880 \times 1024 \times 192$	1.46
C4p0^2	4.0	1.44	162.5	−1.0	4.6	−2.0	2.0	−0.15	0.15	$1792 \times 1280 \times 128$	6.25
C4p0^3	4.0	1.44	162.5	−2.0	6.0	−4.0	4.0	−0.15	0.15	$1280 \times 1280 \times 64$	50.0
C6p0^1	6.0	2.16	243.7	−0.5	4.0	−1.0	1.0	−0.15	0.15	$2880 \times 1280 \times 192$	1.25
C6p0^2	6.0	2.16	243.7	−1.0	5.0	−2.0	2.0	−0.15	0.15	$1920 \times 1280 \times 128$	4.63
C6p0^3	6.0	2.16	243.7	−2.0	7.2	−4.0	4.0	−0.15	0.15	$1472 \times 1280 \times 64$	50.0

TABLE 5.1: Run parameters. The superscripts denote the simulations in phase one, phase two and phase three of each case, as described in § 5.3. The formation number Fn is defined at the end of the forcing period (see § 5.4.2). The time $\hat{t}$ denotes the end of each phase of the simulation. All lengths and times listed here are respectively given in units of $\mathcal{L}$ and $\mathcal{L}/\mathcal{U}$, where $\mathcal{L} = 40R$ and $\mathcal{U} = J^{1/2}/10R$.

case was at least three times larger than the lateral size of the turbulent patch, since it has been demonstrated in Figure 4.8 that this value of L_y is sufficiently large that the effects of periodicity can be neglected.

5.4 Results

Below we present DNS results from simulations for a range of C. The adequacy of grid resolution is first verified in § 5.4.1, followed in § 5.4.2 by the early-time development which includes the breakdown process of the elongated momentum

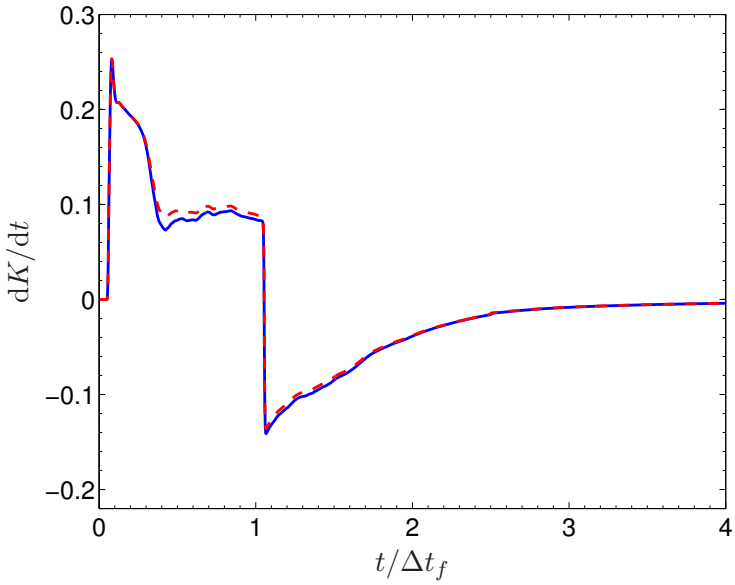

FIGURE 5.4: History of rate of change of volume-integrated kinetic energy $\mathrm{d}K/\mathrm{d}t$ for Case C1p0: —— $\mathrm{d}K/\mathrm{d}t$; ---- $-\epsilon_K - F_K + \int u_i T_i \,\mathrm{d}x\,\mathrm{d}y\,\mathrm{d}z$.

patch. Finally, the effect of the confinement number on the evolution of the patch is explored in § 5.4.3.

5.4.1 Resolution Check

It can be checked whether the grid resolution used is fine enough to capture the smallest turbulence scales by comparing the difference between the rate of change of the volume-integrated instantaneous kinetic energy[1] K and the volume integrated rate of kinetic energy dissipation ϵ_K, together with the net volume-integrated kinetic energy flux F_K and the volume integrated work due to the external force $\int u_i T_i \,\mathrm{d}x\,\mathrm{d}y\,\mathrm{d}z$ (see Equation 4.9), as shown in § 4.2.1. Case C1p0 is used to demonstrate the adequacy of the spatial resolution, since the resolution for all cases is identical during the forcing period. Figure 5.4 displays the history of $\mathrm{d}K/\mathrm{d}t$ versus the RHS of Equation (4.9) during phase 1 (including the forcing duration) and phase 2 of Case C1p0. It was found that the difference was less than 0.26% of the maximum value of $\mathrm{d}K/\mathrm{d}t$ up to the point of transition to turbulence ($t/\Delta t_f < 0.25$, see § 5.4.2 below). During the breakdown to turbulence, the vortex filaments are stretched to fine scale, which results in an enstrophy peak. Even during this most difficult to resolve phase, reasonable accuracy was obtained with the maximum difference of about 5%. After the forcing has stopped, the turbulent

[1]When the co-moving frame of reference is being used, the pseudo force due to the frame acceleration of $-\mathrm{d}U_F/\mathrm{d}t$ must be taken into account, such that $K = \frac{1}{2}\int \left(u_i u_i - U_F^2\right) \,\mathrm{d}x\,\mathrm{d}y\,\mathrm{d}z$.

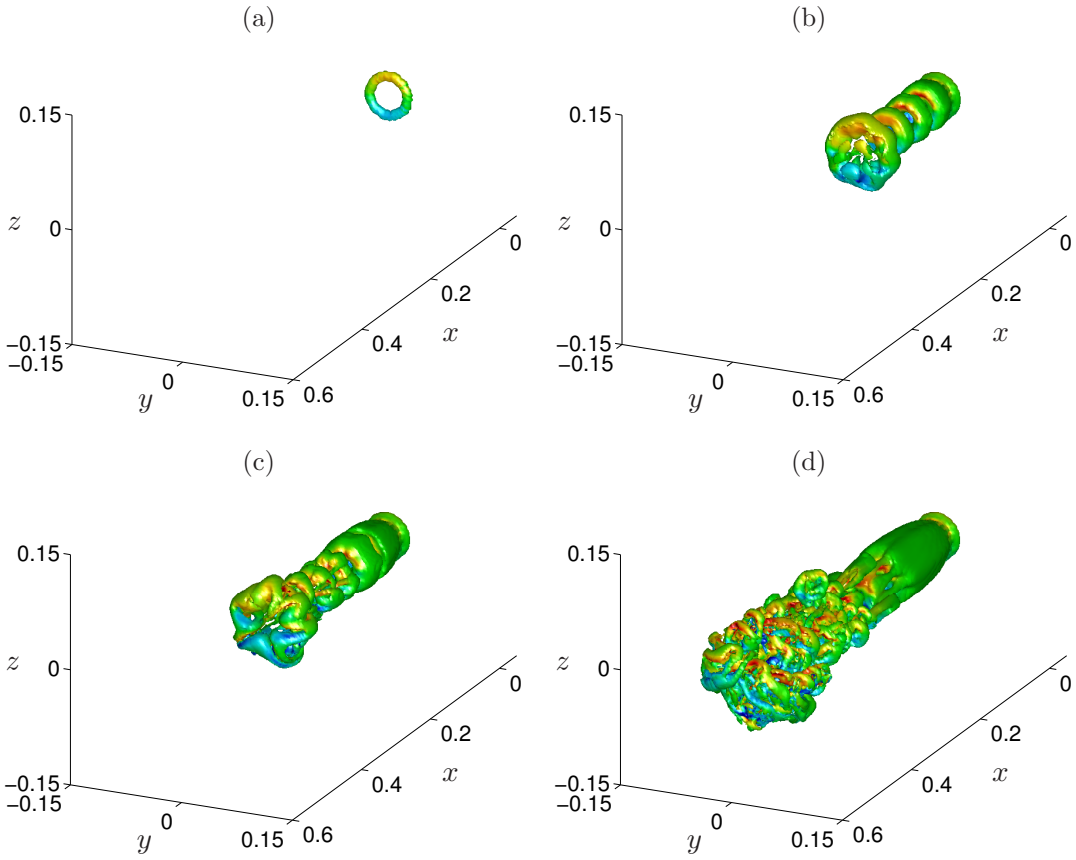

FIGURE 5.5: Isosurfaces of Q, coloured by ω_y, showing the evolution of the momentum patch during the forcing duration for Case C1p0: (a) $t/\Delta t_f = 0.06$, (b) $t/\Delta t_f = 0.25$, (c) $t/\Delta t_f = 0.33$, (d) $t/\Delta t_f = 0.5$. The formation number at each time is: (a) $Fn = 2.26$, (b) $Fn = 10.16$, (c) $Fn = 13.54$, (d) $Fn = 20.31$.

patch starts to decay, leading to a decrease in the error after $t/\Delta t_f > 2$ being less than 0.32%.

5.4.2 Early-Time Characteristics and Breakdown to Turbulence

It is now well known that the formation of a vortical structure generated by an impulsive momentum source can be classified into two regimes depending on the value of the dimensionless *formation number* Fn, defined in experiments of Gharib *et al.* (1998) (who used a round-piston-driven jet nozzle to create a vortex ring), as $Fn = L/D$, where L is the piston stroke and D is the nozzle diameter. They observed that when $Fn \geqslant 4$, the vortex ring does not gain any further circulation and thus disconnects from a portion of vorticity behind it (called a trailing jet). This process is usually referred to as vortex ring *pinch-off*.

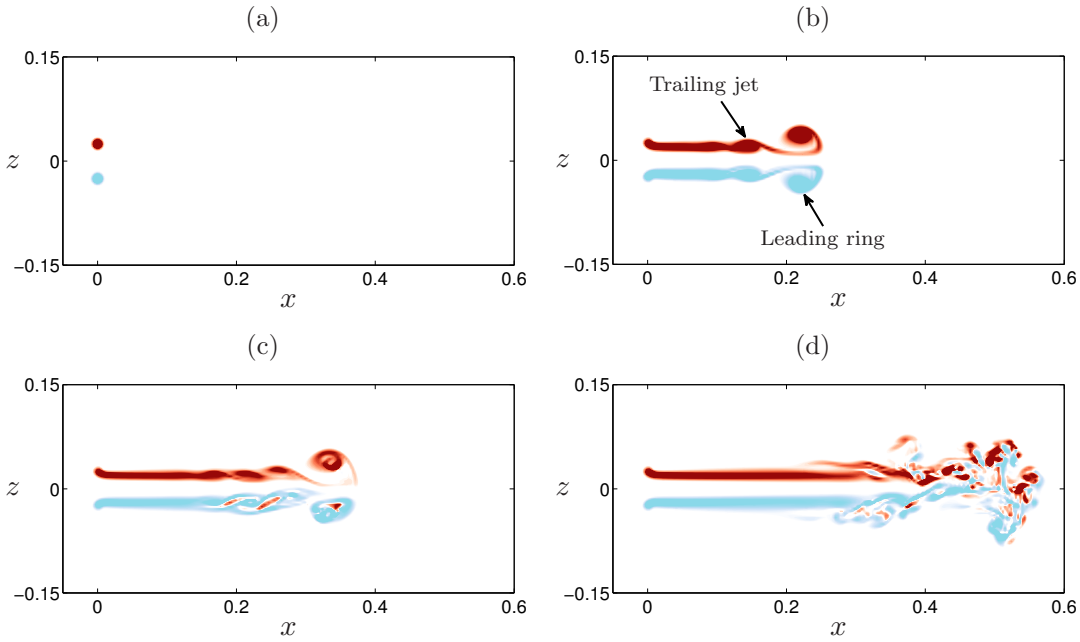

FIGURE 5.6: Side view of contours of ω_y at the centreline ($y = 0$) during the forcing duration for Case C1p0: (a) $t/\Delta t_f = 0.06$, (b) $t/\Delta t_f = 0.25$, (c) $t/\Delta t_f = 0.33$, (d) $t/\Delta t_f = 0.5$. Vorticity varies from $-0.2 < \omega_y/|\omega_y|_{\max} < 0.2$. Blue (light) and red (dark) patches show negative and positive vorticity, respectively. See Figure 5.5 for information regarding the formation number at each time.

To explain the very early-time behaviour of the momentum patch created by the disk-like body force, we can define the equivalent formation number by equating its impulse $I = J\Delta t_f$ (cf. Equation 5.13) with the impulse of the coherent structure induced by the piston mechanism $I_p = \pi D^2 L^2 / 4\Delta t_f$ (Gharib *et al.*, 1998), such that the formation number at the end of the forcing duration can be written as

$$Fn = \frac{2\Delta t_f}{D^2}\left(\frac{J}{\pi}\right)^{1/2} . \tag{5.16}$$

The nozzle diameter is assumed to be equal to the diameter of the body force $D = 2R$. For all cases considered here, the formation number at the end of the forcing period is larger than its critical value $Fn_{\text{cr}} \approx 4$ (see Table 5.1) and the momentum patch becomes fully turbulent before hitting the free surface, such that the evolution of the momentum patch during the forcing period is identical. Hence, Case C1p0 is again selected to explain the evolution of the momentum patch during the forcing duration ($t \leqslant \Delta t_f$), including the breakdown process of the patch.

The development of the momentum patch is visualised by means of the second invariant of the velocity gradient tensor $Q = -0.5 u_{i,j} u_{j,i}$ depicted in Figure 5.5,

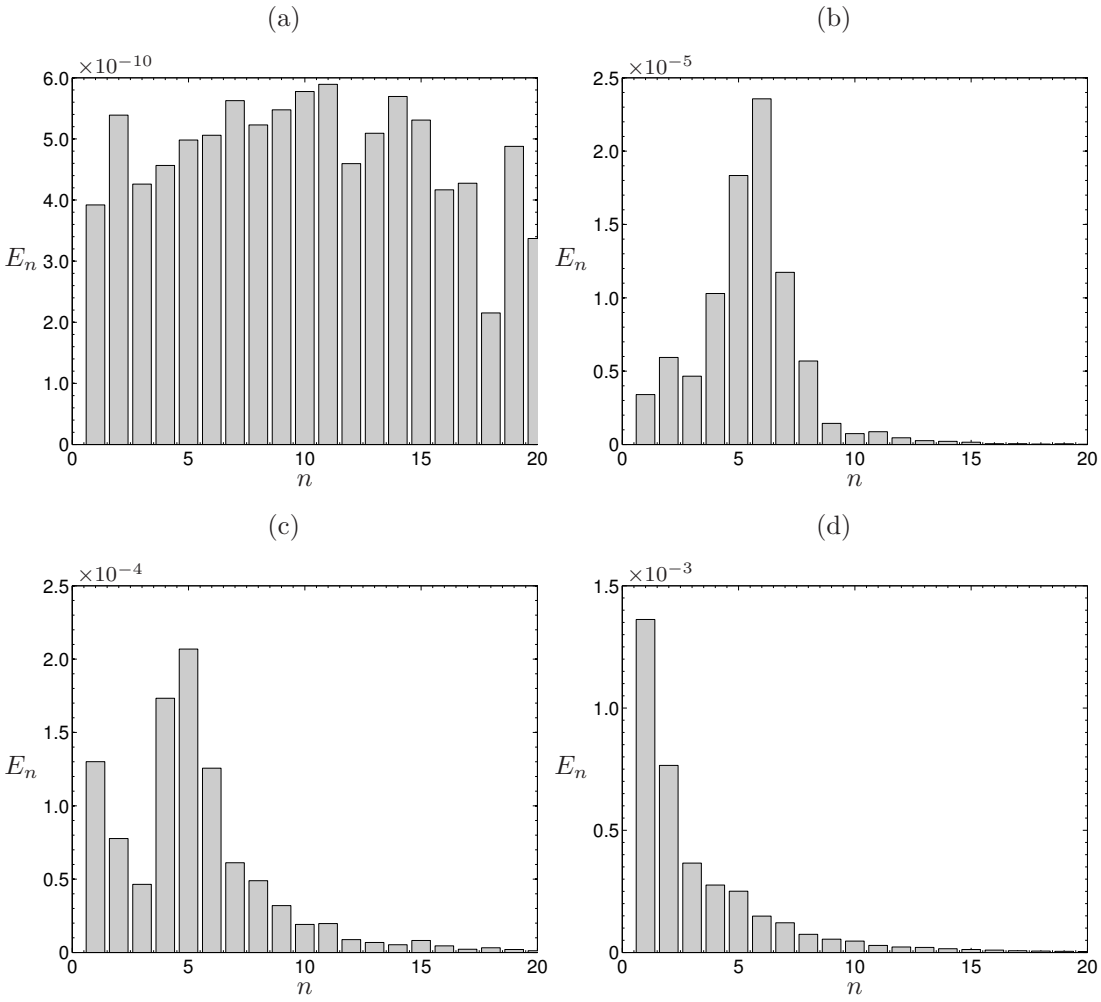

FIGURE 5.7: Azimuthal modal energies for Case C1p0 at selected times: (a) $t/\Delta t_f = 0.06$, (b) $t/\Delta t_f = 0.25$, (c) $t/\Delta t_f = 0.33$, (d) $t/\Delta t_f = 0.5$.

and the contours of the lateral vorticity ω_y at the centreline $y = 0$, illustrated in Figure 5.6. Immediately after the forcing is active, an axisymmetric laminar vortex ring is formed, as displayed in Figures 5.5(a) and 5.6(a). At this time, the momentum flux is still being injected into the fluid while the ring is propagating in the streamwise direction. Once the formation time is larger than its critical value ($Fn_{\mathrm{cr}} \approx 4$), the leading vortex ring begins detaching from its trailing jet, resulting in the roll-up of the trailing vorticity to form a series of vortices similar to the well-known Kelvin–Helmholtz instability. This phenomena can be clearly seen in the plots of vorticity contours (Figures 5.6b and 5.6c).

Since the Reynolds number considered here is high enough, the leading vortex ring and its trailing jet develop three-dimensional instabilities and undergo transition to turbulence. The breakdown mechanism of this elongated vortical structure

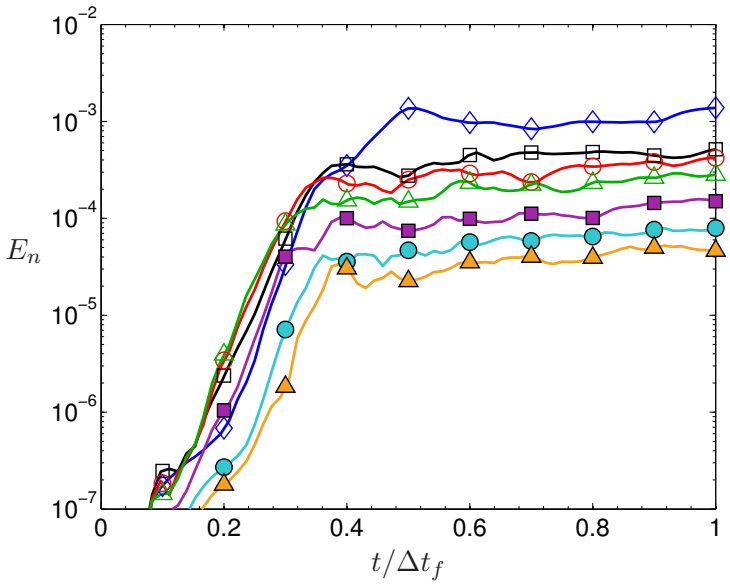

FIGURE 5.8: Evolution of selected azimuthal modal energies for Case C1p0: ◇ $n = 1$; □ $n = 4$; ○ $n = 5$; △ $n = 6$; ■ $n = 8$; ● $n = 10$; ▲ $n = 12$.

is described as follows. While the elongated momentum patch is moving downstream, the leading vortex ring develops an azimuthal instability (often called the *Widnall* instability), which leads to the distortion of the leading ring into stationary waves, of an integer number n, around the ring circumference. As can be seen from Figure 5.5(c), six waves appear around the leading ring, suggesting that $n = 6$ mode is the most dominant azimuthal mode for this part of the flow (details of vortex ring instabilities can be found in, for example, Shariff *et al.*, 1994; Archer *et al.*, 2008). It is of interest to note that while the leading ring breaks down subject to a Widnall-like instability, the trailing jet also becomes turbulent through a classical Kelvin–Helmholtz breakdown, depicted in Figure 5.6(c). At later times, the finer-scale structures develop due to the stretching of the vortex filaments, such that the momentum patch becomes fully turbulent, as illustrated in Figures 5.5(d) and 5.6(d).

To determine the most dominant azimuthal mode (i.e. the mode with the largest growth rate during the linear instability phase) of the elongated vortex, we extracted the modal energy spectrum by performing a Fourier transform in the azimuthal direction. Note that we computed the azimuthal modal energies of the whole momentum patch, not just the leading ring. Note also that, in order to calculate the azimuthal modal energies, the velocity field on the Cartesian grid needs to be interpolated onto cylindrical coordinates. Figure 5.7 shows the modal kinetic energies of the first twenty azimuthal modes, while evolution of some azimuthal modes of the kinetic energy is provided in Figure 5.8. During the initial

α_1	α_2	α_3	α_4	α_5	α_6	α_7	α_8	α_S
32.64	20.34	41.21	44.89	52.44	56.18	46.03	44.62	58.85

TABLE 5.2: Growth rates α_n of selected azimuthal modes together with the viscous predicted growth rate α_S of Shariff *et al.* (1994), applied to the leading ring. Growth rates are given in units of $\mathcal{U}/\mathcal{L}$.

laminar phase, all the azimuthal modes have about the same level of the kinetic energy (Figure 5.7a). This also validates the choice made about the level of the azimuthal perturbation. With time, the kinetic energy of each mode E_n increases individually with different growth rates α_n as shown in Figure 5.8. We determined the growth rate,

$$\alpha_n = \frac{1}{2E_n}\frac{\mathrm{d}E_n}{\mathrm{d}t}\,, \tag{5.17}$$

by averaging it over $0.0417\Delta t_f$ time units centred at $t/\Delta t_f = 0.2083$. The growth rates of some azimuthal modes are reported in Table 5.2. It can be seen that the $n = 6$ mode is still the most amplified mode for the whole elongated vortex over the time window considered, with $\alpha_6 = 56.18$. This mode also has the highest kinetic energy during the linear phase as illustrated in Figure 5.7(b).

The highest growth rate (α_6) is then compared with the estimated growth rate of a single vortex ring, first proposed by Widnall & Tsai (1977) for the inviscid case and modified to account for the effect of viscosity by Shariff *et al.* (1994). The viscous estimated growth rate α_S of Shariff *et al.* (1994) is

$$\alpha_S = \alpha_{WT}\left[1 - \frac{\hat{\alpha}}{Re_S}\right]\,, \tag{5.18}$$

where α_{WT} is the inviscid prediction of Widnall & Tsai (1977), defined as

$$\alpha_{WT} = \frac{\Gamma_r}{4\pi R_r^2}\left[\left\{0.856\ln\left(\frac{8R_r}{a_1}\right) - 0.9102\right\}^2 - 0.4535\right]^{1/2}\,, \tag{5.19}$$

$\hat{\alpha}$ is a non-dimensional coefficient, $Re_S = ea_1^2/\nu$ is the internal Reynolds number, with e the local induced strain field (Saffman, 1978)

$$e = \frac{3\Gamma_r}{16\pi R_r^2}\left[\ln\left(\frac{8R_r}{a_e}\right) - \frac{17}{12}\right]\,; \tag{5.20}$$

Γ_r and R_r are respectively the circulation and radius of the leading ring, $a_1 = 1.1214\sigma_r$ and $a_e = 1.3607\sigma_r$ are measures of the leading ring core radius (Shariff

et al., 1994) and σ_r is the leading ring core thickness. Note that the last coefficient in Equation (5.19) is different from that in Widnall & Tsai (1977) due to the error corrected by Shariff *et al.* (1994). We calculated α_S the same way as Archer *et al.* (2008) did by using the instantaneous Γ_r, R_r, a_1 and a_e at $t/\Delta t_f = 0.2083$ with $\hat{\alpha} = 8$, and found that the relative difference between the present growth rate of the most dominant mode (α_6) and Shariff *et al.*'s (1994) prediction applied to the leading ring (α_S) was about 4.54%. This suggests that the elongated momentum patch breaks down to turbulence due to the azimuthal instability of the leading ring.

During the nonlinear instability phase, the most dominant mode and its neighbouring modes interact nonlinearly with each other resulting in the rapid growth of their harmonics and the lower modes (see Figures 5.7c and 5.8). All of the modes saturate at $t/\Delta_f \approx 0.5$, when the leading ring and its trailing jet become fully turbulent. The spectrum at this time (Figure 5.7d) is consistent with the Kolmogorov turbulence cascade, with energy presumably transferred from larger scales (lower wavenumbers) to smaller scales (higher wavenumbers).

5.4.3 Effect of Confinement Number on the Turbulent Patch

To illustrate the effect of the confinement number, we compare the development of the turbulent patches after the forcing period from Cases C0p2, C1p0, C2p0 and C6p0 by visualising the isosurfaces of the second invariant of the velocity gradient tensor Q, as shown in Figure 5.9. For very low value of C (Case C0p2, Figure 5.9a), the vertical confinement is quite weak, such that both vertical and lateral sizes of the patch grow with time due to entrainment of the surrounding fluid and the patch remains axisymmetric. To explore the axisymmetric nature observed from this case, histories of the ratio of the lateral ℓ_y (Equation 4.5) to the vertical sizes ℓ_z (Equation 4.6) of the patch are displayed in Figure 5.10. It can be seen that ℓ_y/ℓ_z for Case C0p2 is always about unity suggesting that the vertical confinement has very little influence on the vertical development of the patch. Therefore, the fluid layer for this value of C can be considered as *deep*. This also suggests that the turbulent patch will maintain its axisymmetric nature ($\ell_y/\ell_z = 1$) as C approaches zero.

For higher values of C, the vertical confinement influences the evolution of the patch. The vertical growth of the patch is limited by the non-deformable stress-free layers and only the horizontal size of the patch can expand due to lateral entrainment, as depicted in Figure 5.10. If C is not strong enough (e.g. Case

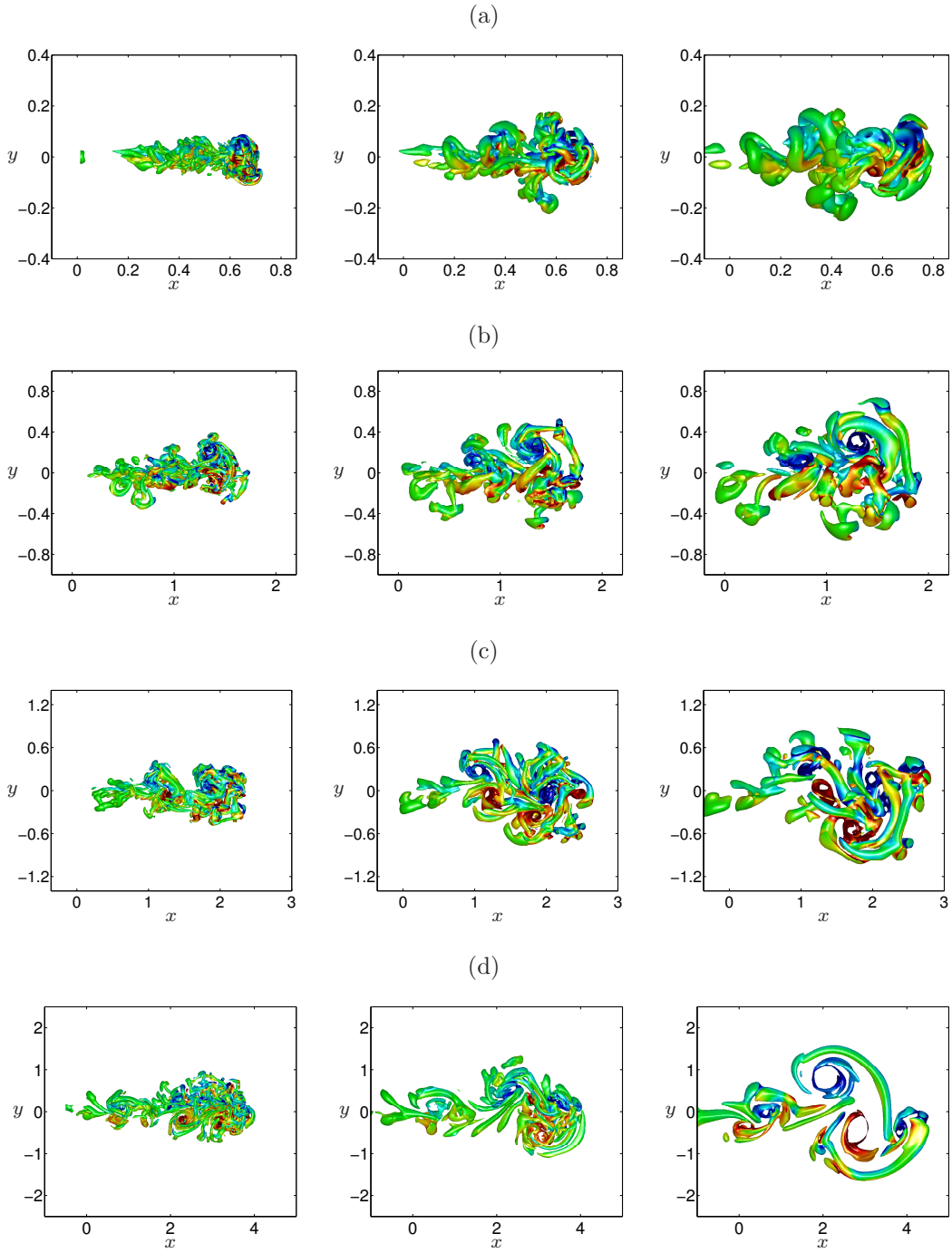

FIGURE 5.9: Top view of isosurfaces of Q, coloured by ω_z, showing the development of the turbulent patch at (left) $t/\Delta t_f = 4$, (middle) $t/\Delta t_f = 10$ and (right) $t/\Delta t_f = 20$: (a) Case C0p2, (b) Case C1p0, (c) Case C2p0, (d) Case C6p0.

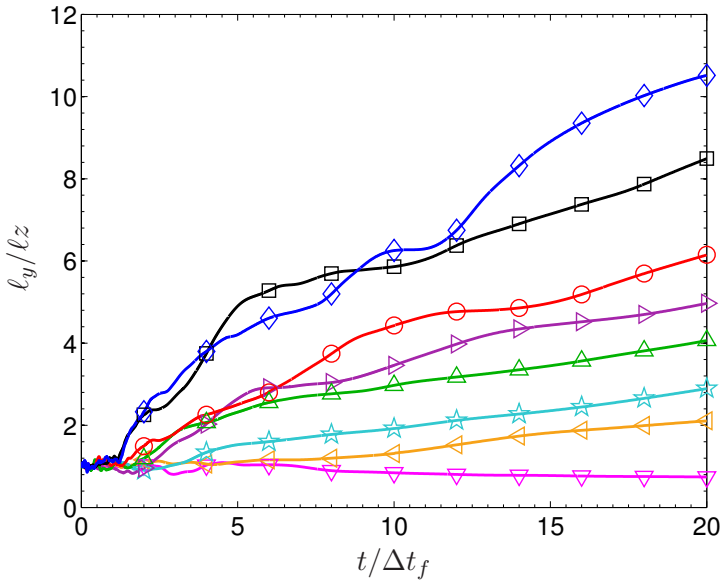

FIGURE 5.10: Histories of the ratio of the lateral to the vertical sizes (ℓ_y/ℓ_z): ◇ Case C6p0; □ Case C4p0; ○ Case C2p5; △ Case C2p0; ▷ Case C1p5; ☆ Case C1p0; ◁ Case C0p5; ▽ Case C0p2.

C1p0), the patch does not form a counter-rotating vortical structure before it is affected significantly by the vertical confinement (Figure 5.9b). When C is about and greater than its estimated critical value (e.g. Cases C2p0 and C6p0), a counter-rotating vortex appears at late time with the lateral length scale much larger than its vertical size (Figures 5.9c and 5.9d). We can then consider that the fluid layer for values of C higher than about unity is *shallow*.

A plot of the size of the turbulent patch δ_d (see Equation 4.1) versus time is given in Figure 5.11(a). Immediately after the forcing ends, δ_d for each case increases rapidly with different growth rates depending on the impulse of the flow. After this phase, the patch reaches its self-similar state and the size of the patch continues to grow with the lower rate. For strong C, the vertical growth of the patch is suppressed by the stress-free layers, so that the patch tends to evolve as a vortex dipole whose δ_d increases with time as $t^{1/3}$ (Voropayev *et al.*, 1991, 2008). On the other hand, when the vertical confinement has little effect on the vertical growth (i.e. as for Cases C0p2 and C0p5), the size of the patch grows as $\delta_d \sim t^{1/4}$, similar to that of a vortex ring (see, e.g., Glezer & Coles, 1990). The late-time histories show that the weakly confined case grows slower than the strongly confined ones do.

As shown in Equation (5.7), the initial size of the patch is governed by the forcing period Δt_f and the forcing intensity J. This led us to use J and Δt_f to normalise the size of the patch. The non-dimensional size δ_d^* is written as

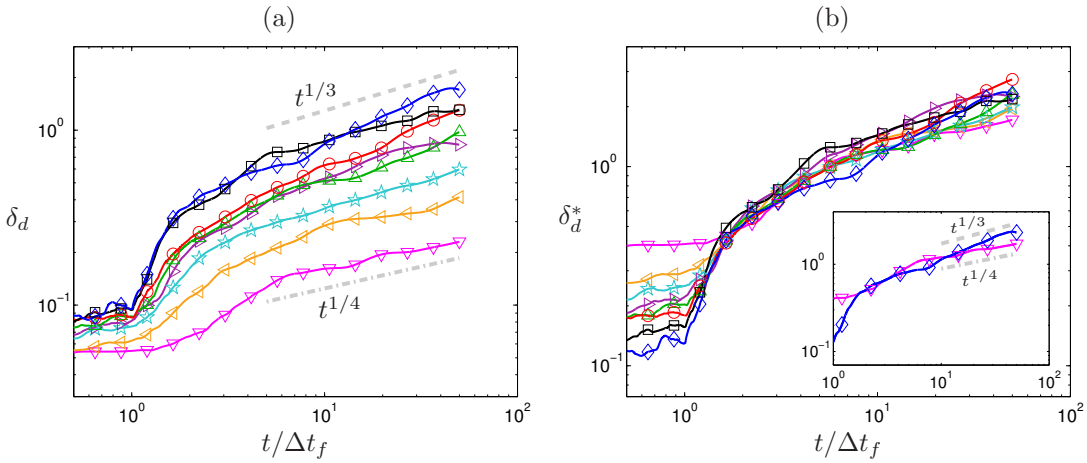

FIGURE 5.11: Histories of (a) size of the patch δ_d and (b) non-dimensional size $\delta_d^* = \delta_d / J^{1/4} \Delta t_f^{1/2}$: ◇ Case C6p0; □ Case C4p0; ○ Case C2p5; △ Case C2p0; ▷ Case C1p5; ☆ Case C1p0; ◁ Case C0p5; ▽ Case C0p2.

$\delta_d^* = \delta_d / J^{1/4} \Delta t_f^{1/2}$. It can be seen from Figure 5.11(b) that δ_d^* from all cases tend to collapse onto one curve up to $t/\Delta t_f \approx 3$. This confirms that the initial size of the turbulent patch which occurs at $t/\Delta t_f \approx \mathcal{O}(1)$ is *universal* when scaled by $J^{1/4} \Delta t_f^{1/2}$, and also supports the physical interpretation of the confinement number. After this time, the effect of the vertical confinement begins to affect the development of the patch, leading to the different growth rate of δ_d at late time, as discussed earlier.

Figure 5.12 depicts the evolution of the surface signatures from different confinement numbers. At each time, different contour values of the non-dimensional vertical vorticity, $\omega_z^* = \omega_z \Delta t_f$, is used to indicate the surface signatures in order to make the pictures more informative since the vortex decays with time. For relatively low duration and intensity of the forcing (e.g. Case C0p2, see Figure 5.12a), no significant signature appears at the free surface at the early times ($t/\Delta t_f \leqslant 10$). Later ($t/\Delta t_f = 20$), the eddy signature is observed at the free surface but is not well structured. At intermediate value of C (Case C1p0, Figure 5.12b), the turbulent patch rapidly penetrates to the surface. The horizontal size of the patch increases with time but it does not transform into a vortex dipole due to the fact that the confinement number is not high enough. When C is higher than 2, the eddy signature is clearly detectable at the beginning ($t/\Delta t_f = 4$) and is still turbulent. At larger times, the small-scale turbulence decays, while the large-scale coherent structure still remains and transforms into a dipole, as illustrated in Figures 5.12(c) and 5.12(d). This indicates that a dipole only forms when C is greater than about unity, even though a surface signature seems to be seen for all the values of C considered here.

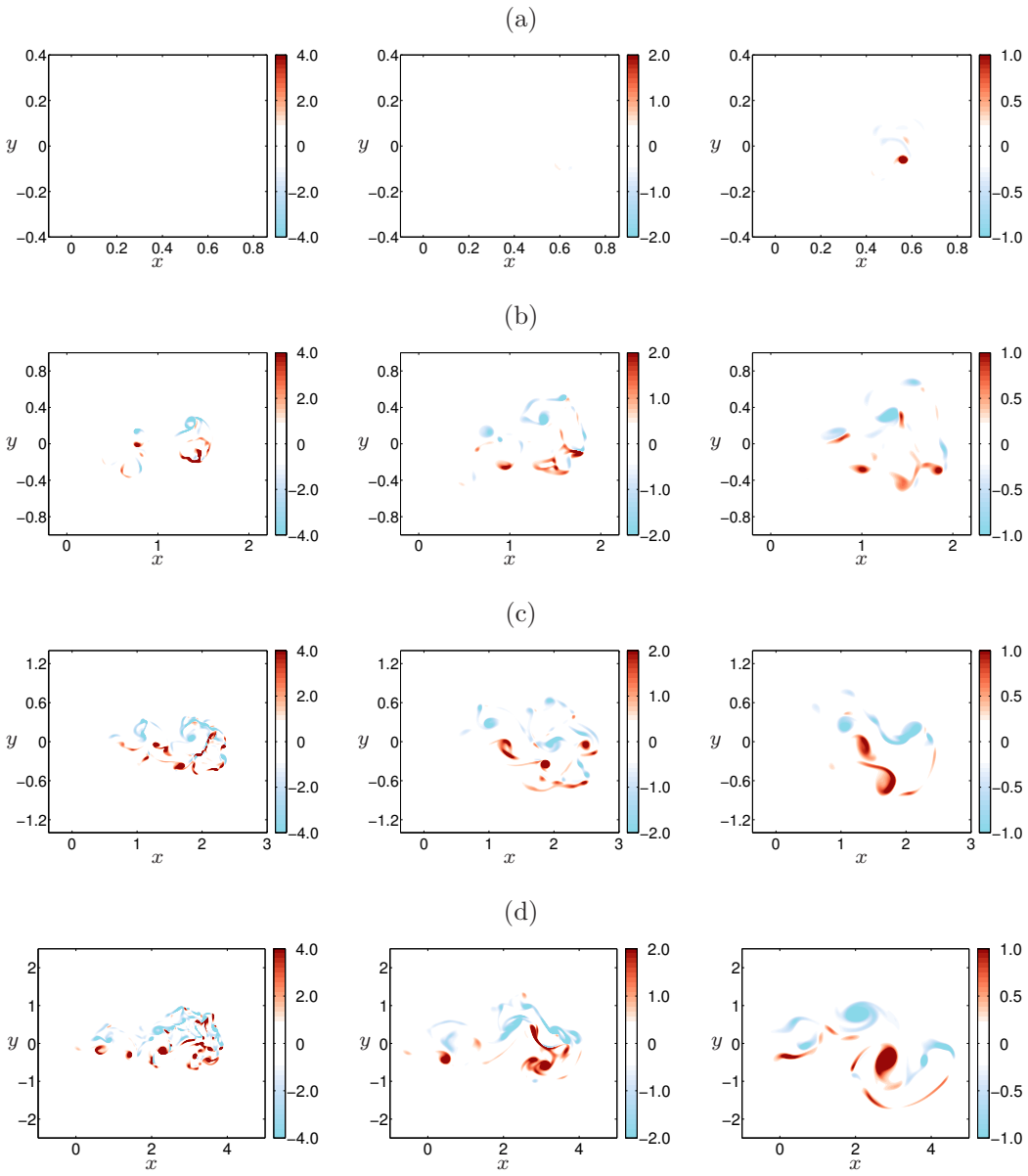

FIGURE 5.12: Contours of ω_z, normalised by Δt_f, at the free surface showing the penetration of the signature at (left) $t/\Delta t_f = 4$, (middle) $t/\Delta t_f = 10$ and (right) $t/\Delta t_f = 20$: (a) Case C0p2, (b) Case C1p0, (c) Case C2p0, (d) Case C6p0. Blue (light) and red (dark) patches show negative and positive vorticity, respectively.

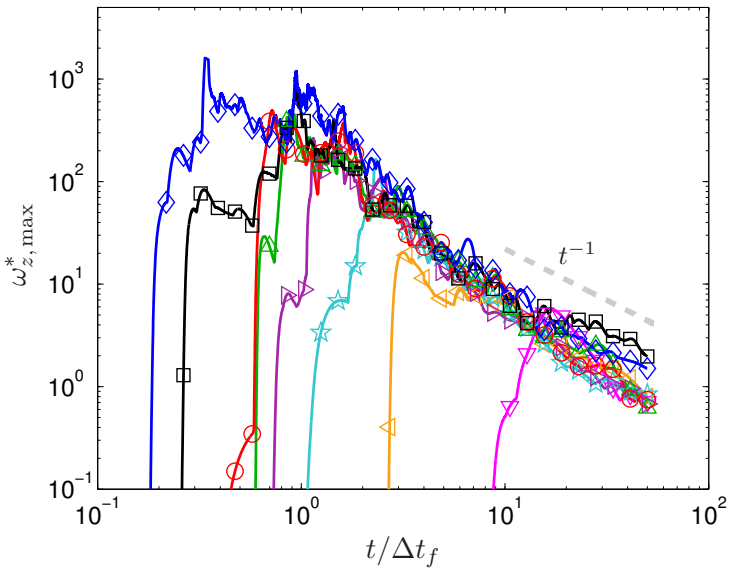

FIGURE 5.13: Decay of maximum value of non-dimensional vertical vorticity, $\omega^*_{z,\max} = \omega_{z,\max}\Delta t_f$, at the free surface: ◇ Case C6p0; □ Case C4p0; ○ Case C2p5; △ Case C2p0; ▷ Case C1p5; ☆ Case C1p0; ◁ Case C0p5; ▽ Case C0p2.

Figure 5.13 displays histories of the maximum value of the non-dimensional vertical vorticity, $\omega^*_{z,\max} = \omega_{z,\max}\Delta t_f$, at the free surface. It can be seen that the turbulent patch for higher confinement number requires shorter time to arrive at the free surface. Once the patch hits the free surface, the vortex filaments reconnect with their image, such that the maximum value of the vorticity at the free surface of each vortex line equals to that within the domain leading to the dramatic rise in the vertical vorticity at the free surface. Since the momentum patch is turbulent, some vortex lines that have lower $\omega^*_{z,\max}$ might encounter the free surface earlier than the others. This results in a staircase-like increase of $\omega^*_{z,\max}$, which can be observed from, for example, Cases C1p0, C1p5 and C4p0. After $\omega^*_{z,\max}$ from each case has reached its maximum value, over time, it tends to collapse onto a single profile and decrease with time. We observed that $\omega^*_{z,\max}$ of the eddy signature in the turbulent regime (i.e. $t/\Delta t_f < 10$) decays faster than that of a laminar eddy, in which $\omega^*_{z,\max}$ decreases as t^{-1} (Voropayev *et al.*, 2007, 2008). Once most of the small-scale structures disappear, the decay rate of $\omega^*_{z,\max}$ reduces to At^{-1}, with $A \approx 47.57$. The value of A from the present calculations is comparable to that of Case JS3a, in which a Gaussian force is used to generate the momentum patch at the same Reynolds number, but with different impulse ($A = 41.52$; see Tables 4.1 and 4.2). This implies that A is independent of the type of the body force and the impulse of the flow, as suggested by Voropayev *et al.* (2008).

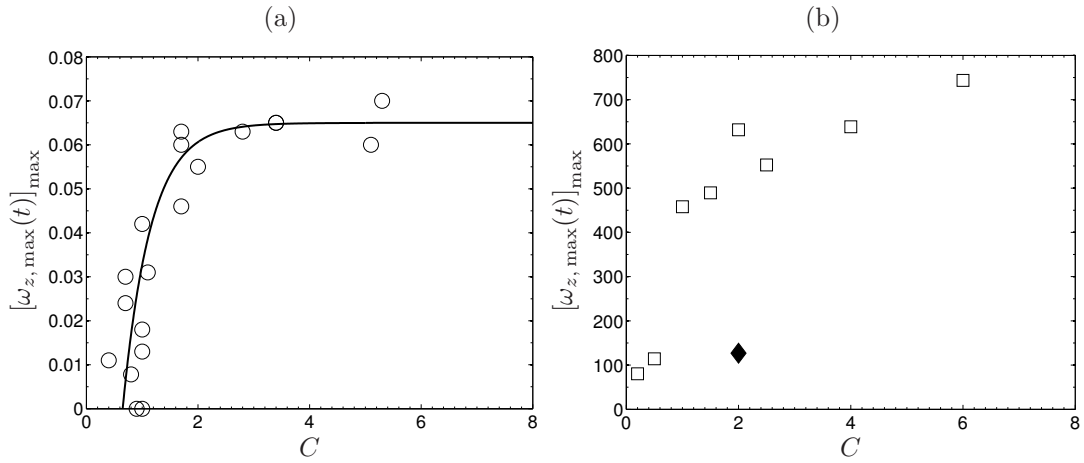

FIGURE 5.14: Surface signature contrast $[\omega_{z,\max}(t)]_{\max}$ versus the confinement number C. (a) Voropayev *et al.*'s (2007) data: ○ PIV measurements; —— Voropayev *et al.*'s (2007) phenomenological model $[\omega_{z,\max}(t)]_{\max} = 0.065\left[1 - \mathrm{e}^{2(0.65-C)}\right]$. (b) DNS results: □ disk-like body force ($J = 1/16$ and $h = 0.3$ for all simulations; cf. Table 5.1); ◆ Gaussian body force at the same Reynolds number but with different forcing intensity and domain depth ($J = 1/4$, $\Delta t_f = 4$, $h = 1$).

In order to determine the relationship between the intensity of a surface signature and the confinement number C, we follow Voropayev *et al.* (2007), who performed Particle Image Velocimetry (PIV) measurements in a two-layer fluid at $Re_j = \mathcal{O}(10000)$, and use the maximum value of $\omega_{z,\max}(t)$, denoted by $[\omega_{z,\max}(t)]_{\max}$, to represent the surface signature contrast. Note that $\omega_{z,\max}$ by itself can be used to represent the contrast number of Voropayev *et al.* (2007) (cf. Equation 1.10) since their rms background vorticity was approximately the same in all of their runs. A plot of the surface signature contrast $[\omega_{z,\max}(t)]_{\max}$ as a function of the confinement number C is illustrated in Figure 5.14. Unlike Voropayev *et al.*'s (2007) finding (Figure 5.14a), the relationship between our signature contrast and the confinement number cannot be characterised by an exponential profile, especially when the data from the Gaussian-force simulation, at the same Reynolds number but with different forcing intensity J and domain depth h, is included (Figure 5.14b). The data from the Gaussian-force simulation lies outside the rest, indicating that no relationship between our $[\omega_{z,\max}(t)]_{\max}$ and C can be characterised.

The collapse of a set of our data can be obtained when normalising $[\omega_{z,\max}(t)]_{\max}$ with the forcing duration Δt_f as illustrated in Figure 5.15(b). This normalisation

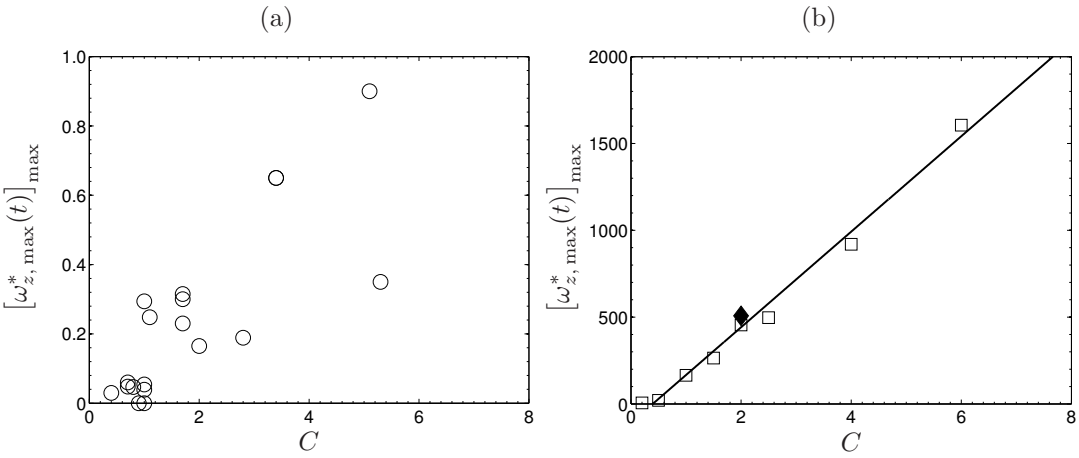

FIGURE 5.15: Maximum value of $\omega^*_{z,\max}(t) = \omega_{z,\max}(t)\Delta t_f$ versus the confinement number C. (a) Voropayev *et al.*'s (2007) PIV data. (b) DNS results: □ disk-like body force ($J = 1/16$ and $h = 0.3$ for all simulations; cf. Table 5.1); ◆ Gaussian body force at the same Reynolds number but with different forcing intensity and domain depth ($J = 1/4$, $\Delta t_f = 4$, $h = 1$); —— $\left[\omega^*_{z,\max}(t)\right]_{\max} = 275.0028C - 108.5455$.

yields a linear relationship between the confinement number and the surface signature contrast. A curve fit to this relationship is

$$\left[\omega^*_{z,\max}(t)\right]_{\max} = 275.0028C - 108.5455\,. \tag{5.21}$$

In contrast to our observation, Figure 5.15(a) shows that the data from Voropayev *et al.*'s (2007) PIV measurements do not collapse when normalised by Δt_f particularly once C is higher than 2, and the amplitude of their $\left[\omega^*_{z,\max}(t)\right]_{\max}$ is much lower (about 1600 times). These discrepancies occur presumably because the small-scale turbulent eddies at the free surface in Voropayev *et al.*'s (2007) experiments are smoothed out due to the low-pass filtering effect of an interrogation window (e.g. see Willert & Gharib, 1991; Eggels *et al.*, 1994). To verify this assumption, we applied low-pass filters to our vertical vorticity at the free surface. Three types of filters are chosen, which are the n$^{\text{th}}$-order low-pass filter G_n, the Gaussian filter G_g and the sharp spectral filter G_s. The filter functions in Fourier space are defined as

$$\widehat{G}_n\left(\kappa_x, \kappa_y\right) = \frac{1}{1 + \left(\kappa/\kappa_c\right)^n}\,, \tag{5.22}$$

$$\widehat{G}_g\left(\kappa_x, \kappa_y\right) = \exp\left[-\frac{\kappa^2}{\kappa_c^2}\right]\,, \tag{5.23}$$

$$\widehat{G}_s\left(\kappa_x, \kappa_y\right) = \frac{1}{2}\,\mathrm{erfc}\left(\frac{\kappa - \kappa_c}{0.01\kappa_c}\right)\,, \tag{5.24}$$

where κ_x and κ_y are respectively the wavenumbers in the streamwise and lateral directions, $\kappa = \sqrt{\kappa_x^2 + \kappa_y^2}$ and κ_c is the cutoff wavenumber.

Figure 5.16(a) depicts the effect of the low-pass filters on the development of the maximum amplitude of the vertical vorticity. It can be seen that all the low-pass filters used here decrease the maximum amplitude of $\omega^*_{z,\max}(t)$ and delay the vorticity peak. In addition, they also reduce both the growth and the decay rates (the development before and after the peak time, respectively) of $\omega^*_{z,\max}$. The peak value and the decay rate depend on the level of the cutoff wavenumber κ_c and are roughly identical at the same level of κ_c. On the other hand, different growth rates are observed when the cutoff wavenumber is lower than a certain value (i.e. $\kappa_c \approx 10$). We then compared the evolution of our filtered $\omega^*_{z,\max}$, obtained from using the fifth-order filter with $\kappa_c = 5$, with the PIV data for a range of C of Voropayev *et al.* (2007). Note that we adapted figure 5 of Voropayev *et al.* (2007), which shows a plot of their contrast number as a function of time, to obtain histories of their $\omega^*_{z,\max}$. As can be seen from Figure 5.16(b), the filtered DNS result is in reasonable agreement with the PIV data.

The effect of a low-pass filter on the small-scale eddies at the free surface can clearly be seen from a contour plot of the filtered vertical vorticity, where the fifth-order filter with $\kappa_c = 5$ was employed. As shown in Figure 5.17(b), all the small-scale turbulent eddies (which can be observed from the unfiltered vorticity, displayed in the left column of Figure 5.12c) are smeared out by the filter, leading to only the appearance of a large-scale counter-rotating vortex pair at the free surface. The low-pass filter gives a surface signature very similar to that observed in Voropayev *et al.*'s (2007) experiments, in which only a vortex dipole appeared at the free surface without any small-scale turbulence although their Reynolds number for this case is approximately 34 times higher than ours (see Figure 5.17a). This suggests that the intensity of the surface signature is set by the small-scale turbulence when the confinement number is strong, and confirms the linear relationship between the surface signature contrast (when it is represented by the non-dimensional vertical vorticity) and the confinement number.

Even though the point measurement (maximum value of $\omega^*_{z,\max}(t)$) can be used to represent the surface signature intensity, this method might not be accurate enough when the surface signature is turbulent. We therefore introduce the intensity of the surface signature in terms of the maximum amplitude of an

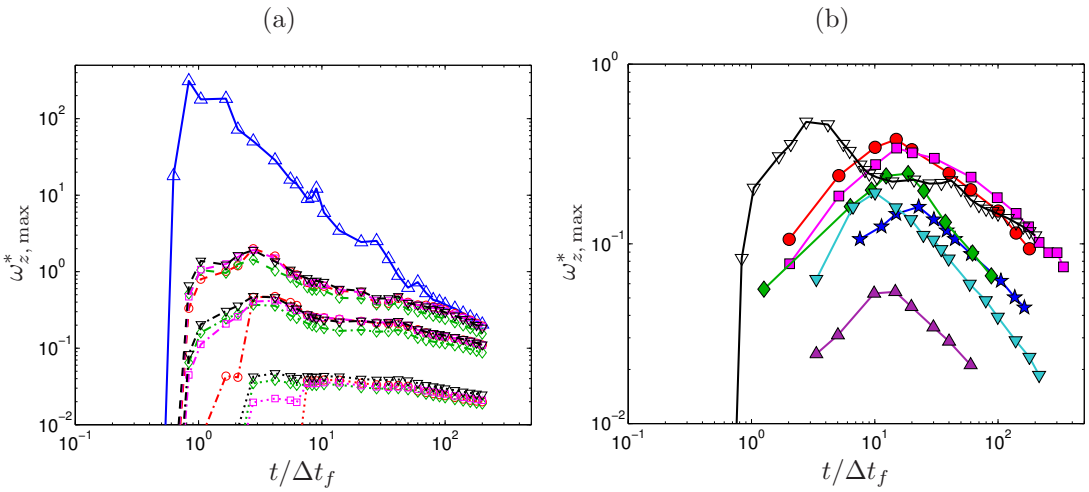

FIGURE 5.16: (a) Effect of low-pass filters on the evolution of the maximum value of the vertical vorticity of Case C2p0. Symbols denote types of filters used, while line styles indicate cutoff wavenumber κ_c: △ Unfiltered data; ○ sharp spectral filter; ◇ Gaussian filter; □ tenth-order filter; ▽ fifth-order filter; - - - - $\kappa_c = 10$; -·-·- $\kappa_c = 5$; ····· $\kappa_c = 2$. (b) History of the maximum amplitude of the filtered vertical vorticity (using fifth-order filter with $\kappa_c = 5$) from the present DNS at $C = 2.0$ (open symbol ▽) compared with the PIV data in a range of C of Voropayev *et al.* (2007) (filled symbol: ■ $C = 5.3$; ▼ $C = 2.8$; ★ $C = 2.0$; ● $C = 1.7$; ◆ $C = 1.1$; ▲ $C = 1.0$).

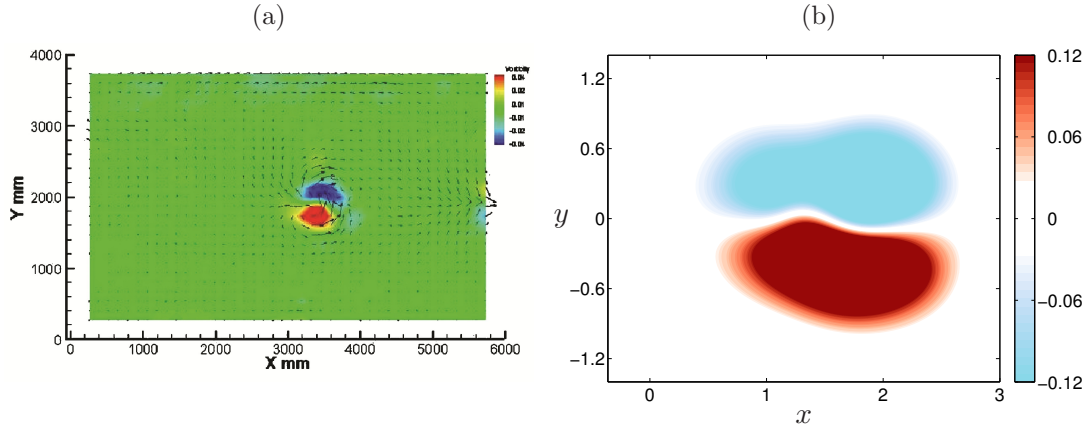

FIGURE 5.17: Contour of (filtered) vertical vorticity ω_z at the free surface at $C = 2.0$: (a) Voropayev *et al.*'s (2007) PIV measurement at $t/\Delta t_f = 3.33$ and $Re_j = 42000$ (their run no. 21); (b) Filtered DNS data of Case C2p0 using a fifth-order low-pass filter with $\kappa_c = 5$ at $t/\Delta t_f = 4$ and $Re_j = 1250$. Vorticity in both pictures is in the range $\omega_z \Delta t_f = \pm 0.12$. The PIV grid spacing is about 0.12 metres (corresponding to $0.34 J^{1/4} \Delta t_f^{1/2}$), while the filter used decreases the DNS resolution to be similar to using the grid spacing of approximately $0.13\mathcal{L}$ (or about $0.3 J^{1/4} \Delta t_f^{1/2}$).

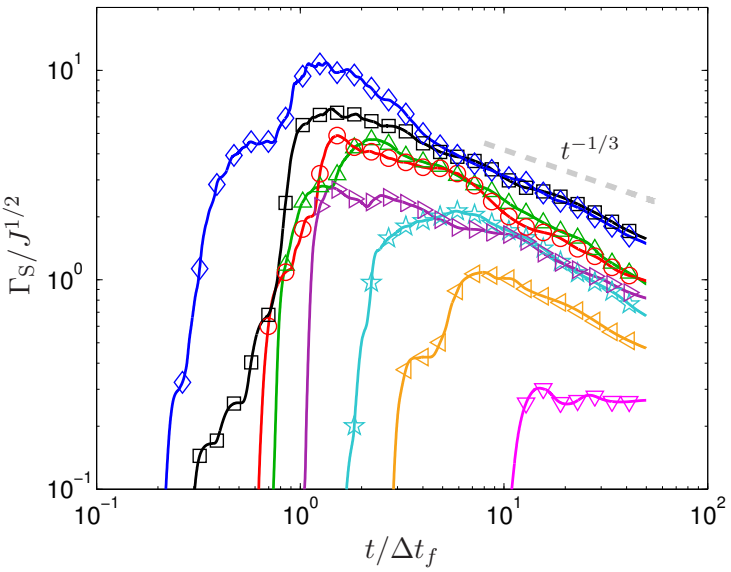

FIGURE 5.18: Histories of non-dimensional eddy strength $\Gamma_S/J^{1/2}$ at the free surface: ◇ Case C6p0; □ Case C4p0; ○ Case C2p5; △ Case C2p0; ▷ Case C1p5; ☆ Case C1p0; ◁ Case C0p5; ▽ Case C0p2.

integral parameter that depicts the strength of the surface eddy, written as

$$\Gamma_S = \frac{1}{2}\int |\omega_z| \, \mathrm{d}x \, \mathrm{d}y \, . \tag{5.25}$$

Although this integral quantity becomes identical to the circulation of the surface dipolar eddy at late time when all the small-scale turbulence decays, it overestimates the circulation at the early time due to the contribution of the opposite-sign small-scale turbulent eddies. An advantage of using this definition is that it can correctly estimate the strength of the surface eddy when the eddy propagates away from the centreline.

Histories of the surface eddy strength Γ_S, normalised by the forcing intensity J, from different values of the confinement number are displayed in Figure 5.18. The evolution of the eddy strength is similar to that of the maximum value of the vertical vorticity except that the eddy strength at the free surface does not collapse when scaled by J. From dimensional arguments, the decay of Γ_S can be written in terms of the eddy size δ_d and the maximum amplitude of the vertical vorticity $\omega_{z,\max}$ as

$$\Gamma_S \sim \omega_{z,\max}\delta_d^2 \, . \tag{5.26}$$

For a laminar dipole, δ_d increases with time as $\sim t^{1/3}$, while $\omega_{z,\max}$ varies as t^{-1} (Voropayev *et al.*, 2008). Substituting these power laws into Equation (5.26) yields

$$\Gamma_S \sim t^{-1/3} \, . \tag{5.27}$$

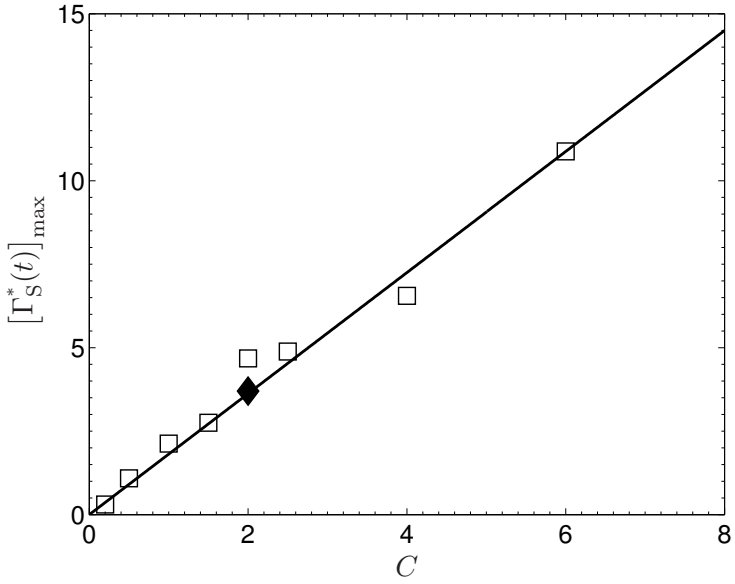

FIGURE 5.19: Peak value of the non-dimensional surface signature strength $\Gamma_S^* = \Gamma_S/J^{1/2}$ versus the confinement number C: □ disk-like body force ($J = 1/16$ and $h = 0.3$ for all simulations; cf. Table 5.1); ◆ Gaussian body force at the same Reynolds number but with different forcing intensity and domain depth ($J = 1/4$, $\Delta t_f = 4$, $h = 1$); —— $\left[\Gamma_S^*(t)\right]_{max} = 1.8129C$.

It is found that the strength of the surface eddy at late time for all cases decreases close to $t^{-1/3}$, except for Case C0p2 for which the eddy strength is approximately constant, presumably because the surface eddy for this case is not yet well organised (cf. Figure 5.12a).

The relationship between the peak value of the non-dimensional surface signature strength $\Gamma_S^* = \Gamma_S J^{-1/2}$ and the confinement number C is displayed in Figure 5.19. The data, including the Gaussian-force simulation, show that the maximum value of Γ_S^* increases linearly with increasing confinement number, approximated as

$$\left[\Gamma_S^*(t)\right]_{max} = 1.8129C\,. \tag{5.28}$$

Combining Equations (5.21) and (5.28) also yields the linear relationship between $[\Gamma_S(t)]_{max}$ and $[\omega_{z,\,max}(t)]_{max}$, as

$$[\Gamma_S(t)]_{max} \sim [\omega_{z,\,max}(t)]_{max}\, J^{1/2}\Delta t_f\,. \tag{5.29}$$

Note that Equation (5.29) also supports the dimensional argument used to estimate the decay rate of the eddy strength (Equations 5.26 – 5.27) since the initial size of the turbulent patch that occurs at $t/\Delta t_f \approx \mathcal{O}(1)$, denoted by $\delta_{d,0}$, are set by J and Δt_f (cf. Figure 5.11b), such that $J^{1/2}\Delta t_f \sim \delta_{d,0}^2$.

5.5 Chapter Summary

Numerical simulations of the effect of the confinement number on the evolution of impulsively generated turbulent patches, induced by an external disk-like body force, have been performed using DNS. The range of the confinement numbers considered here represents the development of the patch in both deep and shallow layers.

Before reaching the free surface, the momentum patches for all cases consist of a vortex ring followed by a trailing jet, since here the formation number is quite large. The momentum patch undergoes transition to turbulence by a Widnall-like instability of the leading ring, although the development of the Kelvin–Helmholtz instability arising in the trailing jet was also observed. The highest growth rate of the azimuthal modal energies of the elongated momentum patch is in close agreement with the estimated growth rate of a viscous vortex ring proposed by Shariff *et al.* (1994).

Nondimensionalising the size of the patch by the forcing intensity and duration leads to a universal history profiles. This confirms that the confinement number can be used to predict the characteristics of the eddy signature at the free surface. When the confinement number is strong enough, the non-deformable stress-free top and bottom layers suppress the vertical growth of the patch leading to, in some cases, the appearance of a quasi-two-dimensional counter-rotating vortex. The patches for all cases penetrate to the free surface but with different intensity and the time required, dependent on the confinement number. For values of C lower than about 1, the surface eddy is not yet in the form of a dipole and might not be detectable since its intensity is relatively low. The contrast ($\omega_{z,\max}$) and strength (Γ_S) of the surface eddy decay according to estimated scaling laws, while both of their maximum amplitude (when normalised by J and Δt_f) increase linearly with an increase in confinement number.

Chapter 6

Concluding Remarks

6.1 Conclusions

A major concern for a manoeuvring self-propelled vehicle is the possible occurrence of a large quasi-planar counter-rotating vortical structure when the vehicle changes its speed or direction. Determining the conditions under which such a coherent structure can appear and understanding its dynamics were the principal motivation of this dissertation. Specifically, the focus is on investigating the evolution of a turbulent patch induced by a submerged self-propelled body starting from rest in the upper ocean, where the patch may be transformed to a pancake-like eddy by the vertical confinement of the free surfaces.

At the beginning of this project, the numerical tools used to represent the manoeuvring body were developed. An accelerating motion of a self-propelled body was successfully emulated by the combination of an immersed boundary (IB) method and an external body force. These tools were employed in an existing in-house DNS code, CgLES, and were separately validated (see § 3). An external body force was validated by performing two-dimensional finite- and zero-momentum wakes. It was found that when the body force is used as a drag in a 2D simulation, it successfully generates a large-scale two-dimensional structure (a Kármán vortex street). On the other hand, the body force produces a wake with fine-scale turbulence, which requires many more grid points to fully capture, for a three-dimensional simulation when the forcing magnitude is strong (i.e. $J_D/0.5\pi\sigma^2 U_\infty^2 > 1$). To eliminate this problem, an immersed boundary method was used to represent a drag from a virtual body. The IB approach was validated with flow past a sphere in a laminar, unsteady planar symmetric regime. Even though only one grid point was placed within the boundary layer of the virtual sphere, the IB approach used provides satisfactory comparison for the Strouhal number, drag and lateral force coefficients.

An accelerating motion of a self-propelled body was first idealised by an impulsive jet, represented by applying an impulsive body force in the positive streamwise direction, to generate a turbulent patch and to study the dynamics of a late-time pancake-like eddy (see § 4). The numerical experiments were conducted in a shallow layer corresponding to the confinement number $C = 2$ for which a vortex dipole was experimentally observed, at different Reynolds numbers. At this value of C the vertical growth of a momentum patch was found to be limited by the non-deformable stress-free top and bottom layers yielding a dipole at the free surface. A dipole was found to persist for a longer time compared to an axisymmetric toroidal vortex in a deep layer. A coherent structure behind the manoeuvring body was then investigated in a shallow layer of the same depth. The vortex penetrated to the free surface and produced a wake signature which was eventually transformed into a dipole. At later time, the dipole vortices from both initialisations (impulsive jet and manoeuvring body) were found to reach a self-similar state and follow the predicted scaling laws, in spite of possessing a Reynolds-number dependence.

The effect of the confinement number on the development of a momentum patch induced by an impulsive jet was examined in § 5. During the forcing period, the patch appeared in the form of a leading vortex ring together with a trailing jet and broke down to turbulence due to an instability very similar to the Widnall instability before appearing at the free surface. Data for the size of the patch were found to collapse when normalised by the forcing duration Δt_f and forcing intensity J. This confirms that the initial shapes of the patch are controlled by J and Δt_f and the confinement number can be used to quantify the intensity and formation of the surface eddy signature. Increasing the confinement number decreases the time required for the patch to hit the free surface. Since the vorticity of the the patch decays inversely proportional to time, the drop in the time required thus results in an increase in the maximum amplitude of the surface signature contrast and the surface eddy strength. Even though the eddy signature was observed to appear at the free surface for all the confinement numbers considered here, the formation of a dipole was found for values of C greater than about 1. For lower values of C, the eddy signature possesses relatively low contrast and strength so that it might be more difficult to be detected, e.g., by remote sensing in presence of background noise.

6.2 Recommendations for Future Work

In future work it would be of interest to investigate the evolution of the momentum patch in more realistic conditions. One of these conditions is to consider the effect of background turbulence in the upper ocean. Another situation of interest is the influence of a surface wave. If strong enough, these conditions could alter the development and formation of the eddy signature. For example, background turbulence is expected to increase the decay rate of the patch, while a surface wave is believed to affect the vortex reconnection process and thus influences the formation and intensity of the surface eddy.

Since this work focused only on a large-scale coherent structure behind a self-propelled body starting from rest, another possible work that can be considered is to investigate the evolution of a wake eddy produced when the body accelerates again after moving at constant speed. The dynamics of the latter momentum patch might be completely different from the starting vortex because the latter coherent structure will interact with a frontal momentumless wake generated when the body moves at constant velocity.

References

Afanasyev, Y. D. 2004 Wakes behind towed and self-propelled bodies: Asymptotic theory. *Phys. Fluids* **16** (8), 3235–3238.

Afanasyev, Y. D. & Korabel, V. N. 2006 Wakes and vortex streets generated by translating force and force doublet: Laboratory experiments. *J. Fluid Mech.* **553**, 119–141.

Afanasyev, Y. D. & Korabel, V. N. 2008 Wakes and vortex streets behind a localized force: Numerical simulations. *Commun. Nonlinear Sci. Numer. Simul.* **13** (6), 1101–1111.

Ahlnäs, K., Royer, T. C. & George, T. H. 1987 Multiple dipole eddies in the Alaska Coastal Current detected with Landsat Thematic Mapper data. *J. Geophys. Res.* **92** (C12), 13041–13047.

Archer, P. J., Thomas, T. G. & Coleman, G. N. 2008 Direct numerical simulation of vortex ring evolution from the laminar to the early turbulent regime. *J. Fluid Mech.* **598**, 201–226.

Archer, P. J., Thomas, T. G. & Coleman, G. N. 2010 The instability of a vortex ring impinging on a free surface. *J. Fluid Mech.* **642**, 79–94.

Branford, S., Coceal, O., Thomas, T. G. & Belcher, S. E. 2011 Dispersion of a point-source release of a passive scalar through an urban-like array for different wind directions. *Bound.-Layer Meteor.* **139** (3), 367–394.

Brucker, K. A. & Sarkar, S. 2010 A comparative study of self-propelled and towed wakes in a stratified fluid. *J. Fluid Mech.* **652**, 373–404.

Cahalan, R. F., Oreopoulos, L., Wen, G., Marshak, A., Tsay, S.-C. & DeFelice, T. 2001 Cloud characterization and clear-sky correction from Landsat-7. *Remote Sens. Environ.* **78** (1–2), 83–98.

Cantwell, B. J. 1986 Viscous starting jets. *J. Fluid Mech.* **173**, 159–189.

Chakraborty, P., Balachandar, S. & Adrain, R. J. 2005 On the relationships between local vortex identification schemes. *J. Fluid Mech.* **535**, 189–214.

Coceal, O., Dobre, A., Thomas, T. G. & Belcher, S. E. 2007 Structure of turbulent flow over regular arrays of cubical roughness. *J. Fluid Mech.* **589**, 375–409.

Coceal, O., Thomas, T. G., Castro, I. P. & Belcher, S. E. 2006 Mean flow and turbulence statistics over groups of urban-like cubical obstacles. *Bound.-Layer Meteor.* **121** (3), 491–519.

Couder, Y. & Basdevant, C. 1986 Experimental and numerical study of vortex couples in two-dimensional flows. *J. Fluid Mech.* **173**, 225–251.

Crow, S. C. 1970 Stability theory for a pair of trailing vortices. *AIAA J.* **8** (12), 2172–2179.

E, W. & Liu, J.-G. 1997 Finite difference methods for 3D viscous incompressible flows in the vorticity–vector potential formulation on nonstaggered grids. *J. Comput. Phys.* **138** (1), 57–82.

Eggels, J. G. M., Unger, F., Weiss, M. H., Westerweel, J., Adrian, R. J., Friedrich, R. & Nieuwstadt, F. T. M. 1994 Fully developed turbulent pipe flow: A comparison between direct numerical simulation and experiment. *J. Fluid Mech.* **268**, 175–210.

Fadlun, E. A., Verzicco, R., Orlandi, P. & Mohd-Yusof, J. 2000 Combined immersed-boundary finite-difference methods for three-dimensional complex flow simulations. *J. Comput. Phys.* **161** (1), 35–60.

Fedorov, K. N. & Ginsburg, A. I. 1989 Mushroom-like currents (vortex dipoles): One of the most widespread forms of non-stationary coherent motions in the ocean. In *Mesoscale/Synoptic Coherent structures in Geophysical Turbulence* (ed. J. C. J. Nihoul & B. M. Jamart), *Elsevier Oceanography Series*, vol. 50, pp. 1–14. Elsevier.

Ferziger, J. H. & Perić, M. 2002 *Computational Methods for Fluid Dynamics*, 3rd edn. Berlin: Springer-Verlag.

Flierl, G. R., Stern, M. E. & Whitehead Jr., J. A. 1983 The physical significance of modons: Laboratory experiments and general integral constraints. *Dyn. Atmos. Oceans* **7** (4), 233–263.

Flór, J. B. & van Heijst, G. J. F. 1994 An experimental study of dipolar vortex structures in a stratified fluid. *J. Fluid Mech.* **279**, 101–133.

Flór, J. B., van Heijst, G. J. F. & Delfos, R. 1995 Decay of dipolar vortex structures in a stratified fluid. *Phys. Fluids* **7** (2), 374–383.

Gharib, M., Rambod, E. & Shariff, K. 1998 A universal time scale for vortex ring formation. *J. Fluid Mech.* **360**, 121–140.

Glezer, A. & Coles, D. 1990 An experimental study of a turbulent vortex ring. *J. Fluid Mech.* **211**, 243–283.

Goldstein, D., Handler, R. & Sirovich, L. 1993 Modeling a no-slip flow boundary with an external force field. *J. Comput. Phys.* **105** (2), 354–366.

van Heijst, G. J. F. & Flór, J. B. 1989 Dipole formation and collisions in a stratified fluid. *Nature* **340** (6230), 212–215.

Hirasaki, G. J. 1967 A general formulation of the boundary conditions on the vector potential in three-dimensional hydrodynamics. PhD thesis, Rice University, Houston, USA.

Hunt, J. C. R., Wray, A. A. & Moin, P. 1988 Eddies, streams, and convergence zones in turbulent flows. In *Proceedings of the 1988 Summer Program*, pp. 193–208. Center for Turbulence Research, Stanford University.

Iaccarino, G. & Verzicco, R. 2003 Immersed boundary technique for turbulent flow simulations. *Appl. Mech. Rev.* **56** (3), 331–347.

Jeong, J. & Hussain, F. 1995 On the identification of a vortex. *J. Fluid Mech.* **285**, 69–94.

Jirka, G. H. 2001 Large scale flow structures and mixing processes in shallow flows. *J. Hydraul. Res.* **39** (6), 567–573.

Johnson, T. A. & Patel, V. C. 1999 Flow past a sphere up to a Reynolds number of 300. *J. Fluid Mech.* **378**, 19–70.

Kim, J., Kim, D. & Choi, H. 2001 An immersed-boundary finite-volume method for simulations of flow in complex geometries. *J. Comput. Phys.* **171** (1), 132–150.

Lin, J. T. & Pao, Y. H. 1979 Wakes in stratified fluids. *Annu. Rev. Fluid Mech.* **11**, 317–338.

Maxey, M. R. & Patel, B. K. 2001 Localized force representations for particles sedimenting in Stokes flow. *Int. J. Multiph. Flow* **27** (9), 1603–1626.

Maxworthy, T. 1977 Some experimental studies of vortex rings. *J. Fluid Mech.* **81**, 465–495.

Mittal, R. & Iaccarino, G. 2005 Immersed boundary methods. *Annu. Rev. Fluid Mech.* **37**, 239–261.

Mohd-Yusof, J. 1997 Combined immersed-boundary/B-spline methods for simulations of flow in complex geometries. *CTR Annual Research Briefs*, NASA Ames/Stanford University.

Mohseni, K., Ran, H. & Colonius, T. 2001 Numerical experiments on vortex ring formation. *J. Fluid Mech.* **430**, 268–282.

Nguyen Duc, J. M. & Sommeria, J. 1988 Experimental characterization of steady two-dimensional vortex couples. *J. Fluid Mech.* **192**, 175–192.

Peskin, C. S. 1972 Flow patterns around heart valves: A numerical method. *J. Comput. Phys.* **10** (2), 252–271.

Peskin, C. S. 2002 The immersed boundary method. *Acta Numerica* **11**, 479–517.

Pinelli, A., Naqavi, I. Z., Piomelli, U. & Favier, J. 2010 Immersed-boundary methods for general finite-difference and finite-volume Navier–Stokes solvers. *J. Comput. Phys.* **229** (24), 9073–9091.

Ploumhans, P., Winckelmans, G. S., Salmon, J. K., Leonard, A. & Warren, M. S. 2002 Vortex methods for direct numerical simulation of three-dimensional bluff body flows: Application to the sphere at Re=300, 500, and 1000. *J. Comput. Phys.* **178** (2), 427–463.

Pope, S. B. 2000 *Turbulent Flows*. Cambridge: Cambridge University Press.

Press, W. H., Teukolsky, S. A., Vetterling, W. T. & Flannery, B. P. 2007 *Numerical Recipes: The Art of Scientific Computing*, 3rd edn. New York, NY: Cambridge University Press.

Ran, H. & Colonius, T. 2009 Numerical simulation of the sound radiated by a turbulent vortex ring. *Int. J. Aeroacoust.* **8** (4), 317–336.

Richardson, S. M. & Cornish, A. R. H. 1977 Solution of three-dimensional incompressible flow problems. *J. Fluid Mech.* **82**, 309–319.

Rojanaratanangkule, W., Thomas, T. G. & Coleman, G. N. 2012 Numerical study of turbulent manoeuvring-body wakes: Interaction with a non-deformable free surface. *J. Turbul.* **13** (N17), 1–22.

Roma, A M., Peskin, C S. & Berger, M J. 1999 An adaptive version of the immersed boundary method. *J. Comput. Phys.* **153** (2), 509–534.

Saffman, P. G. 1970 The velocity of viscous vortex rings. *Stud. Appl. Math.* **49**, 371–380.

Saffman, P. G. 1978 The number of waves on unstable vortex rings. *J. Fluid Mech.* **84**, 625–639.

Saffman, P. G. 1995 *Vortex Dynamics*. Cambridge: Cambridge University Press.

Saiki, E. M. & Biringen, S. 1996 Numerical simulation of a cylinder in uniform flow: Application of a virtual boundary method. *J. Comput. Phys.* **123** (2), 450–465.

Schlichting, H. 1979 *Boundary-Layer Theory*, 7th edn. New York, NY: McGraw-Hill.

Shariff, K., Verzicco, R. & Orlandi, P. 1994 A numerical study of three-dimensional vortex ring instabilities: Viscous corrections and early nonlinear stage. *J. Fluid Mech.* **279**, 351–375.

Sigurdson, L. 1991 Atom bomb/water drop. *Phys. Fluids A* **3** (9), 2034.

Smirnov, S. A. & Voropayev, S. I. 2003 On the asymptotic theory of momentum/zero-momentum wakes. *Phys. Lett. A* **307** (2–3), 148–153.

Sous, D., Bonneton, N. & Sommeria, J. 2004 Turbulent vortex dipoles in a shallow water layer. *Phys. Fluids* **16** (8), 2886–2898.

Sous, D., Bonneton, N. & Sommeria, J. 2005 Transition from deep to shallow water layer: Formation of vortex dipoles. *Eur. J. Mech. B-Fluids* **24** (1), 19–32.

Stern, M E. & Voropayev, S I. 1984 Formation of vorticity fronts in shear flow. *Phys. Fluids* **27** (4), 848–855.

Swearingen, J. D., Crouch, J. D. & Handler, R. A. 1995 Dynamics and stability of a vortex ring impacting a solid boundary. *J. Fluid Mech.* **197**, 1–28.

Tennekes, H. & Lumley, J. L. 1972 *A First Course in Turbulence*. Cambridge, MA: The MIT Press.

Thomas, T. G. & Williams, J. J. R. 1997 Development of a parallel code to simulate skewed flow over a bluff body. *J. Wind Eng. Ind. Aerodyn.* **67–68**, 155–167.

Thomas, T. G. & Williams, J. J. R. 1999 Large eddy simulation of vortex shedding from cubic obstacle. *J. Aerosp. Eng.* **12** (4), 113–121.

Thomas, T. G., Yao, Y. F. & Sandham, N. D. 2003 Structure and energetics of a turbulent trailing edge flow. *Comput. Math. Appl.* **46** (4), 671–680.

Tomboulides, A. G. & Orszag, S. A. 2000 Numerical investigation of transitional and weak turbulent flow past a sphere. *J. Fluid Mech.* **416**, 45–73.

Tutty, O. R. 1986 On vector potential–vorticity methods for incompressible flow problems. *J. Comput. Phys.* **64** (2), 368–379.

Uhlmann, M. 2003 First experiments with the simulation of particulate flows. *Tech. Rep.* 1020. CIEMAT, Madrid, Spain.

Uhlmann, M. 2005 An immersed boundary method with direct forcing for the simulation of particulate flows. *J. Comput. Phys.* **209** (2), 448–476.

Voropayev, S. I., Afanasyev, Y D. & Filippov, I. A. 1991 Horizontal jets and vortex dipoles in a stratified fluid. *J. Fluid Mech.* **227**, 543–566.

Voropayev, S. I., Fernando, H. J. S. & Morrison, R. 2008 Dipolar eddies in a decaying stratified turbulent flow. *Phys. Fluids* **20** (2), 026602.

Voropayev, S. I., Fernando, H. J. S., Smirnov, S. A. & Morrison, R. 2007 On surface signatures generated by submerged momentum sources. *Phys. Fluids* **19** (7), 076603.

Voropayev, S. I., McEachern, G. B., Fernando, H. J. S. & Boyer, D. L. 1999 Large vortex structures behind a maneuvering body in stratified fluids. *Phys. Fluids* **11** (6), 1682–1684.

Voropayev, S. I. & Smirnov, S. A. 2003 Vortex streets generated by a moving momentum source in a stratified fluid. *Phys. Fluids* **15** (3), 618–624.

Voropayev, S. I., Smirnov, S. A. & Brandt, A. 2001 Dipolar eddies in a stratified shear flow. *Phys. Fluids* **13** (12), 3820–3823.

Widnall, S. E. & Tsai, C.-Y. 1977 The instability of the thin vortex ring of constant vorticity. *Phil. Trans. R. Soc. Lond.* **287** (1344), 273–305.

Willert, C. E. & Gharib, M. 1991 Digital particle image velocimetry. *Exp. Fluids* **10** (4), 181–193.

Yakovenko, S. N., Thomas, T. G. & Castro, I. P. 2011 A turbulent patch arising from a breaking internal wave. *J. Fluid Mech.* **677**, 103–133.

Yang, X., Zhang, X., Li, Z. & He, Guo-Wei 2009 A smoothing technique for discrete delta functions with application to immersed boundary method in moving boundary simulations. *J. Comput. Phys.* **228** (20), 7821–7836.

Yao, Y. F., Thomas, T. G., Sandham, N. D. & Williams, J. J. R. 2001 Direct numerical simulation of turbulent flow over a rectangular trailing edge. *Theor. Comput. Fluid Dyn.* **14** (5), 337–358.

Appendix A

Reprint of Published Article

Reprint of Rojanaratanangkule *et al.* (2012)

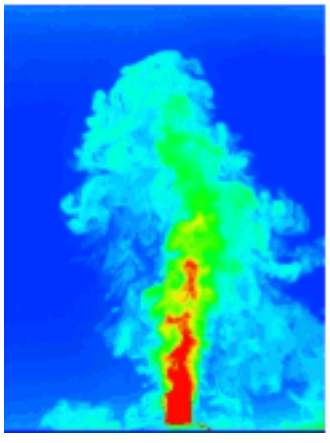

Journal of Turbulence
Publication details, including instructions for authors and subscription information:
http://www.tandfonline.com/loi/tjot20

Numerical study of turbulent manoeuvring-body wakes: Interaction with a non-deformable free surface

Watchapon Rojanaratanangkule [a], T. Glyn Thomas [a] & Gary N. Coleman [a]

[a] Aerodynamics and Flight Mechanics Research Group, Engineering and the Environment, University of Southampton, Southampton SO17 1BJ, UK

Available online: 07 Jun 2012

To cite this article: Watchapon Rojanaratanangkule, T. Glyn Thomas & Gary N. Coleman (2012): Numerical study of turbulent manoeuvring-body wakes: Interaction with a non-deformable free surface, Journal of Turbulence, 13, N17

To link to this article: http://dx.doi.org/10.1080/14685248.2012.680550

Journal of Turbulence
Vol. 13, No. 17, 2012, 1–22

Taylor & Francis
Taylor & Francis Group

Numerical study of turbulent manoeuvring-body wakes: Interaction with a non-deformable free surface

Watchapon Rojanaratanangkule, T. Glyn Thomas and Gary N. Coleman*

Aerodynamics and Flight Mechanics Research Group, Engineering and the Environment, University of Southampton, Southampton SO17 1BJ, UK

(*Received 30 November 2011; final version received 18 March 2012*)

Direct numerical simulation (DNS) is used to investigate the development of a turbulent wake created by an impulsively accelerating axisymmetric self-propelled body below a non-deformable free surface. The manoeuvring body is represented by the combination of an immersed boundary method and a body force. The Reynolds number based on either the diameter of the virtual body or the jet forcing intensity is relatively high (O (1000)), corresponding to the fully turbulent case. The vertical growth of the coherent structure behind the body is restricted by the upper and lower stress-free layers, and the wake signatures are observed to penetrate to the free surface. The late-time behaviour of the dipole induced due to vertical confinement can be predicted by scaling laws, also relevant to a stratified fluid.

Keywords: direct numerical simulation; manoeuvring-body wake; vortex dipole

1. Introduction

Turbulent wakes behind bluff bodies have been investigated both experimentally and numerically by many researchers in order to obtain better understanding of their dynamics. However, almost all of the studies have focused on wakes behind towed or self-propelled objects moving at constant velocity. When a body is towed, it imparts momentum, equal to the drag of the body, to the wake. In contrast, for a constant-speed self-propelled body, the drag is cancelled by the thrust, leading to a zero-momentum wake.

In practice, a submerged vehicle leaves a finite-momentum wake when it accelerates or changes direction, and a momentumless wake only when it moves at constant speed [1]. A manoeuvring-body wake is of interest because it can introduce dynamics that are absent from the constant-velocity case, especially when the wake is influenced by stable stratification or by the presence of an adjacent free surface. For example, dipole vortices produced by the interaction of manoeuvring-body wakes with either stable background density stratification or a free surface can be observed in geophysical flows (see [2–4]). The practical importance of dipole vortices is that they are very large, compared with the size of the body, and long-lived. Voropayev et al. [5] estimate that a coherent kilometre-scale vortical structure that persists for the order of days can be observed behind a typical submarine manoeuvre in the ocean. Moreover, due to the self-induced motion of the dipole

*Corresponding author. Email: g.n.coleman@soton.ac.uk

ISSN: 1468-5248 online only

http://dx.doi.org/10.1080/14685248.2012.680550
http://www.tandfonline.com

vortex, it can transport mass, momentum and other scalar properties, such as heat and salinity.

Generally, when momentum is imparted into a flow, it leads to an isolated region that possesses a high concentration of vorticity and non-zero net linear momentum, often referred to as a turbulent blob. In an unbounded homogeneous fluid, the turbulent blob is fully three-dimensional (3D). While the blob is propagating away from its origin, its vertical and horizontal sizes increase due to the entrainment process of the surrounding fluid and the blob eventually transforms into a toroidal vortical structure [6]. In contrast, when the vertical growth of the blob is confined (e.g. by buoyancy force or flow geometry), only its horizontal size can expand due to lateral entrainment, which leads to a quasi-planar counter-rotating dipole vortex structure.

The formation and evolution of vortex dipoles have been widely studied in a linearly stratified fluid (e.g. see [7–9]), and recently extended to the case of shallow water above a solid no-slip surface, for which the vertical size of a turbulent blob is suppressed by the flow geometry [3, 10, 11]. It was found from the experimental study of Sous et al. [3] that the condition in which the momentum disturbance can coherently penetrate upward and leave its signature at the free surface depends on the *confinement number* $C = J^{1/2}\Delta t_f / h^2$, where J is the forcing intensity, h is the depth of the fluid domain and Δt_f is the forcing interval. The formation and evolution of the vortex dipoles formed in shallow water are similar to those in a stratified fluid except that 3D small-scale turbulence appears at the dipole front. Sous et al. [3] stated that the vertical motion at the frontal region might appear due to the effect of bottom friction.

Voropayev et al. [4] performed experiments in a two-layer fluid, where unstratified water was placed above a layer of salt water, in order to reduce the effect of the bottom surface. Their flow geometry is similar to the real upper ocean (depth 50–100 m), in which denser water rests underneath a nominally constant density gradient. They investigated the intensity of the surface signature in terms of the *contrast number* $Cn = \omega_{z,\,\max}/\omega_{z,\,\mathrm{rms}}$, defined as the ratio of the maximum vertical vorticity $\omega_{z,\,\max}$ of the dipole vortex to the root-mean-square value of the background vertical vorticity $\omega_{z,\,\mathrm{rms}}$, and also defined a relationship between the confinement number and the intensity of the surface signature.

The aim of this work is to investigate the evolution of the impulsively submerged momentum disturbance in the small-scale upper ocean, which is mimicked by stress-free top and bottom layers. Two different types of momentum sources are chosen to investigate the self-similarity of a dipolar vortex created by: (1) an impulsive jet and (2) an accelerating motion of a self-propelled body.

2. Numerical approach

Since the self-propelled body of interest will start from rest, the calculation is performed in a moving reference frame, in order to maintain the location of the body within the computational box. The computational domain for the spatially developing wake is shown in Figure 1. The non-dimensional continuity and incompressible Navier–Stokes equations in a non-inertial moving reference frame can be written in Cartesian tensor notation as

$$\frac{\partial u_i}{\partial x_i} = 0\,, \tag{1}$$

$$\frac{\partial u_i}{\partial t} + u_j \frac{\partial u_i}{\partial x_j} = -\frac{\partial p}{\partial x_i} + \frac{1}{Re_{\mathrm{ref}}} \frac{\partial^2 u_i}{\partial x_j \partial x_j} - \frac{\mathrm{d}U}{\mathrm{d}t}\delta_{1i} + f_i\,, \tag{2}$$

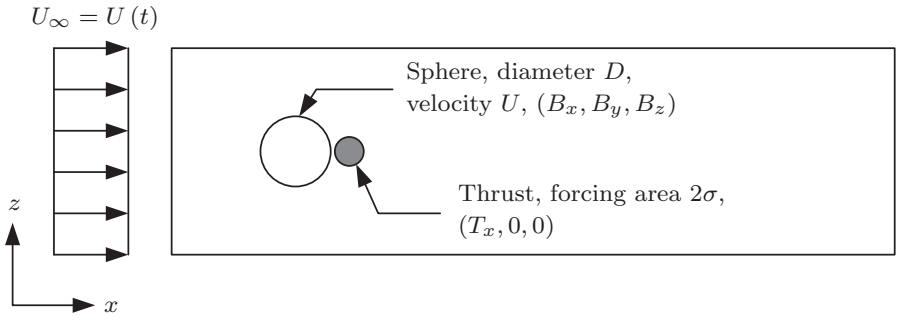

Figure 1. Schematic sketch of geometry of a manoeuvring-body wake.

where $x_i = (x, y, z)$ and $u_i = (u, v, w)$ are, respectively, Cartesian coordinates and the corresponding velocity vector in the streamwise, lateral and vertical directions; t denotes the time; p is the kinematic pressure; U is the velocity of the virtual (wake-generating) body; δ_{ij} is the Kronecker delta and f_i is the external body forces due to the virtual body surface $\mathbf{B} = (B_x, B_y, B_z)$ and/or thrust $\mathbf{T} = (T_x, 0, 0)$. The non-dimensional reference Reynolds number $Re_{\text{ref}} = \mathcal{U}\mathcal{L}/\nu$ is written in terms of the reference length $\mathcal{L}$ and velocity scale $\mathcal{U}$ (which both vary from flow to flow, as illustrated below) and ν is the kinematic viscosity.

The Navier–Stokes equations are advanced in time with the second-order explicit Adams–Bashforth scheme. A second-order central finite-difference scheme is used to discretise the spatial derivatives on a staggered grid, where the velocity components are defined at the cell faces, while the scalar quantity (pressure) is located in the cell centre. The continuity equation is imposed via a standard pressure-correction method. The resulting Poisson equation for the pressure is solved using a parallel multigrid algorithm [12]. Inflow and outflow boundary conditions are employed in the streamwise (x) direction. Additionally, the uniform inflow velocity is set equal to the velocity of the virtual body and is updated every time step. The body is placed midway between an idealised thermocline and a free surface. Stress-free boundary conditions are specified at the top and bottom as an idealisation of the (non-deformable) free surface and the top of a region of a stratified fluid. Periodic conditions are specified in the lateral (y) direction.

In order to embed an axisymmetric body into a computational grid, an immersed boundary technique is employed. The virtual body is mimicked by a set of Lagrangian (virtual surface) points that do not coincide with the Eulerian (computational) points, as shown in Figure 2. The boundary force B_i, which enforces the no-slip boundary condition on the embedded body surface, is calculated directly at the Lagrangian points via a proportional controller, with the proportional gain related to the time step size Δt in such a way that maximises gain while maintaining stability. The boundary force is then transformed into the Eulerian (computational) points by using the three-point discrete delta function proposed by Roma et al. [13].

We emulate the body manoeuvre by imposing a thrust $f_i = T_i = T_x\delta_{1i}$, which is modelled as a jet from the body, as illustrated in Figure 1. The intensity of the thrust is estimated as

$$J_T = u_{\text{jet}} s N \left[u_{\text{jet}} - U(t)\right], \tag{3}$$

where u_{jet} is the jet velocity, s is the area of the nozzle and N is a free parameter used to adjust the jet Reynolds number and the confinement number. A 3D Gaussian function is

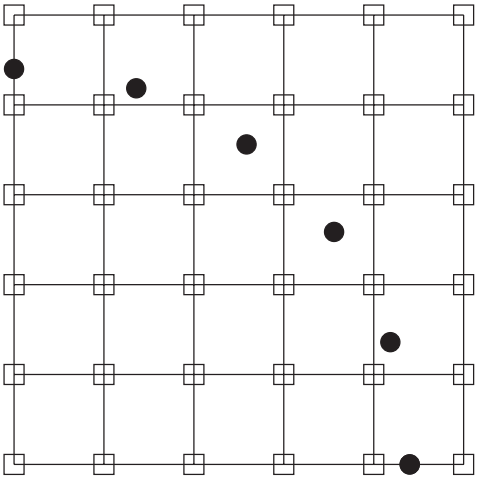

Figure 2. Schemetic sketch showing the locations of the Lagrangian markers (●) and the computational points (□).

used to distribute the intensity of the thrust to the computational grids as

$$T_x = \frac{J_T}{\left(\sigma^2\pi\right)^{3/2}} \exp\left[-\frac{(x-x_0)^2+(y-y_0)^2+(z-z_0)^2}{\sigma^2}\right], \tag{4}$$

where σ is the Gaussian semi-width, and x_0, y_0, z_0 are the centre of the thrust. Note that Equation (4) is determined such that J_T is associated with the total integrated force, not its maximum. The velocity of the body can be found via the balance of momentum between a manoeuvring object and the total force acting on the fluid, with

$$M_{\text{eff}} \frac{\mathrm{d}U}{\mathrm{d}t} = \rho\left(J_T - J_D\right), \tag{5}$$

where M_{eff} is the sum of the actual and added/virtual mass, ρ is the fluid density (taken to be constant) and J_D is the intensity of the drag, which can be calculated from the volume integral of the streamwise boundary force B_x. An explicit Euler method is used to update $U(t)$ at every time step.

3. Validation: 2D zero-momentum wakes

The strategy to impose a force doublet (drag of the body plus thrust) was validated by performing a two-dimensional (2D) simulation of zero-momentum wakes. The results are compared with both an analytical solution [14] and experimental results of Afanasyev and Korabel [15], who used an electromagnetic force to create zero-momentum wakes in a stratified fluid. For the validation, we used a 2D Gaussian function with a Gaussian semi-width σ to distribute the thrust and drag forces. Here, the reference length $\mathcal{L}$ is taken as 5σ, while the reference velocity $\mathcal{U}$ is set to the free-stream velocity U_∞. The drag is applied slightly in front of the thrust. The thrust and drag forces are defined to be of equal magnitude to generate a momentumless wake. The 2D domain size was 96×32, with 3072×1024 grid points in the streamwise and vertical directions, respectively. A uniform velocity of

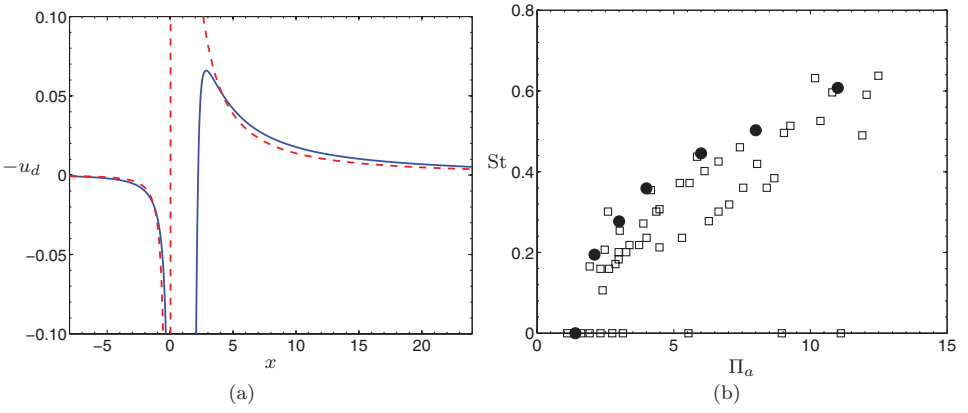

Figure 3. (a) Distribution of the streamwise velocity deficit along its axis of 2D zero-momentum wake at $\Pi_a = 1$ and $\Pi_\nu = 50$: ——— Present, - - - - Theoretical solution [14]. (b) Strouhal number versus Π_a: ●, Present; □, Afanasyev and Korabel [15].

magnitude U_∞ was specified at the inlet, while the velocity convective boundary condition was applied at the outlet. Free-slip boundary conditions were specified in the vertical direction. Figure 3(a) displays the distribution of the streamwise velocity deficit u_d along the axis of the flow for $\Pi_a = \tilde{J}/\sigma U_\infty^2 = 1$ and $\Pi_\nu = \tilde{J}/\nu U_\infty = 50$, where $\tilde{J}$ is the 2D forcing intensity (specific force per unit area), compared with an analytical solution [14]. Away from the expected near-field deviation (due to comparing finite versus singular dipoles), the agreement is satisfactory. For a quantitative comparison with the laboratory experiment [15], the shedding frequency f_s was measured by performing a Fourier transform of the mean value of vorticity at $x = 5$. The Strouhal number $St = f_s \tilde{J}/U_\infty^3$ versus Π_a is displayed in Figure 3(b), showing that the numerical results are in good agreement with the experimental data [15]. The vorticity distribution for $\Pi_a = 11$ and $\Pi_\nu = 230$ is illustrated in Figure 4. The vortex street in this simulation is visually similar to the mushroom-like vortex sheet observed in Afanasyev and Korabel's [15] experiment.

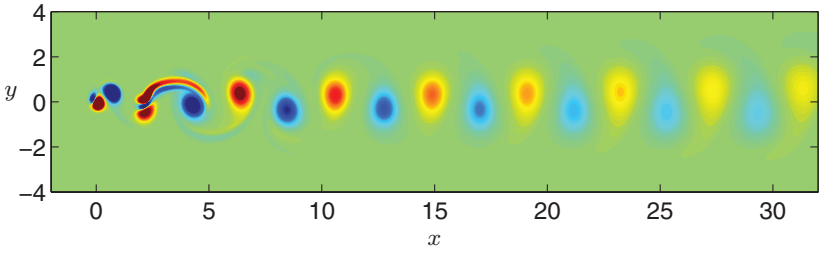

Figure 4. Contours of vorticity of 2D momentumless wake: $\Pi_a = 11$ and $\Pi_\nu = 230$. Vorticity varies from $-0.2 \leq \omega_z/|\omega_z|_{\max} \leq 0.2$. Blue and red patches show negative and positive vorticity, respectively.

4. Jet-induced dipole

We next investigate the evolution and formation of a turbulent blob generated by an impulsive jet as a test case. The jet acts over a short time interval Δt_f with a forcing intensity J_T, distributed to the computational grid via the 3D Gaussian function with semi-width σ. We choose $\Delta t_f = 4$ and $J_T = 1/4$, in units of $\mathcal{L}/\mathcal{U}$ and $\mathcal{U}^2\mathcal{L}^2$, respectively, with $\mathcal{L} = 8\sigma$ (such that $\mathcal{U} = J_T^{1/2}/4\sigma$). When the code described in Section 2 (Equations (1)–(5)) is used to study the evolution of an impulsive jet, the boundary force from the virtual body B_i is not active. Recall that the calculations are carried out in a stationary frame of reference. To study the effect of a (non-deforming) free surface, we consider two distinct canonical flows: an impulsive jet in a deep layer and another in a shallow layer. These are simulated for a jet Reynolds number of 2000 based on the forcing intensity, i.e. $Re_j = J_T^{1/2}/\nu$. Free-slip boundary conditions are applied in the vertical direction for the jet in both deep and shallow layers, while the lateral direction is assumed to be periodic. The main difference between these two cases is that the vertical growth of the vortical structure created by the jet in a deep layer is not confined by the stress-free boundaries. The number of grid cells and the domain size for both cases, labelled as Cases JD and JS1, respectively, are given in Table 1. For the shallow-layer case, the forcing interval and the height of the computational domain were selected to correspond to the confinement number $C = 2$, for which the vortex dipole has been observed at the free surface [4]. Note that the lateral domain width L_y for all cases in this section was chosen to be at least 2.7 times larger than the maximum lateral size ℓ_y of the coherent structure (see Equation (10) below). That this value is sufficient is implied by the agreement of the dipole characteristics for Cases JS3a and JS3LD (which is equivalent to JS3a, apart from using L_y that is twice as large); see Figure 11. However, since the length of the initial momentum-containing region is relatively large, some of the pre-dipole dynamics may be influenced by the lateral domain size. This will be investigated in future studies.

In order to determine the evolution of submersed, impulsive momentum source, the characteristics of the vortical structure, i.e. the dipole propagation velocity and the dipole size, are defined in terms of the integral parameters proposed for vortex-ring geometry by Saffman [16]. The dipole size δ_d and the dipole centroid $\mathbf{X}_d = (X_d, Y_d, Z_d)$ are defined using the first moment of enstrophy via

$$\delta_d = \frac{2}{\Omega} \int r\,|\omega|^2 \,\mathrm{d}x\,\mathrm{d}y\,\mathrm{d}z\,, \tag{6}$$

$$\mathbf{X}_d = \frac{1}{\Omega} \int \mathbf{x}\,|\omega|^2 \,\mathrm{d}x\,\mathrm{d}y\,\mathrm{d}z\,, \tag{7}$$

where $r = \sqrt{y^2 + z^2}$, $|\omega|^2 = \omega_x^2 + \omega_y^2 + \omega_z^2$ and Ω is the total integrated enstrophy, with

$$\Omega = \int |\omega|^2 \,\mathrm{d}x\,\mathrm{d}y\,\mathrm{d}z\,. \tag{8}$$

Thus, the dipole propagation velocity $\mathbf{U}_d = (U_d, V_d, W_d)$ can be obtained as

$$\mathbf{U}_d = \frac{\mathrm{d}\mathbf{X}_d}{\mathrm{d}t}\,. \tag{9}$$

Table 1. Impulsive-jet-induced wake run parameters.

Case	Domain depth (H[a])	Re_j	Domain size	$N_x \times N_y \times N_z$
JD	Deep (4)	2000	$-5 \le x \le 25$, $-4 \le y \le 4$, $-4 \le z \le 4$	$960 \times 256 \times 256$
JS1	Shallow (0.5)	2000	$-5 \le x \le 25$, $-8 \le y \le 8$, $-0.5 \le z \le 0.5$	$960 \times 512 \times 32$
JS2	Shallow (0.5)	2000	$-5 \le x \le 55$, $-8 \le y \le 8$, $-0.5 \le z \le 0.5$	$1920 \times 512 \times 32$
JS3a	Shallow (0.5)	1250	$-5 \le x \le 55$, $-8 \le y \le 8$, $-0.5 \le z \le 0.5$	$1920 \times 512 \times 32$
JS3b[b]	Shallow (0.5)	1250	$-5 \le x \le 55$, $-8 \le y \le 8$, $-0.5 \le z \le 0.5$	$1920 \times 512 \times 32$
JS3LD	Shallow (0.5)	1250	$-5 \le x \le 55$, $-16 \le y \le 16$, $-0.5 \le z \le 0.5$	$1920 \times 1024 \times 32$
JS4	Shallow (0.5)	625	$-5 \le x \le 55$, $-8 \le y \le 8$, $-0.5 \le z \le 0.5$	$1920 \times 512 \times 32$

[a] H is the vertical distance from the centreline of the forcing to the free surface.
[b] This case is equivalent to Case JS3a except that low-level random noise is added to the initial condition.

We also define lateral ℓ_y and vertical ℓ_z length scales of the vortical structure as

$$\ell_y = \frac{2}{\Omega_y} \int_{\mathcal{H}} y|\omega|^2 \, \mathrm{d}x \, \mathrm{d}y \, \mathrm{d}z \,, \tag{10}$$

$$\ell_z = \frac{2}{\Omega_z} \int_{\mathcal{H}} z|\omega|^2 \, \mathrm{d}x \, \mathrm{d}y \, \mathrm{d}z \,, \tag{11}$$

where $\Omega_{y,z} = \int_{\mathcal{H}} |\omega|^2 \, \mathrm{d}x \, \mathrm{d}y \, \mathrm{d}z$ and the subscript $\mathcal{H}$ denotes that the integration is performed over the half-positive y- or z-domain. Note that Equations (6), (10) and (11) all require the origin of the y- and z-axes systems to be in the centre of the computational domain. These definitions give the dipole sizes that are roughly the distance between the vorticity extrema (maximum and minimum) of the dipole [17].

A check of the spatial resolution was performed by comparing the difference between the left- and the right-hand side of the volume-integrated instantaneous kinetic-energy equation, written such that

$$\frac{\mathrm{d}K}{\mathrm{d}t} = -\epsilon_K - F_K + \int u_i T_i \, \mathrm{d}x \, \mathrm{d}y \, \mathrm{d}z \,, \tag{12}$$

where K is the volume-integrated kinetic energy, ϵ_K is the volume-integrated rate of kinetic energy dissipation and F_K is the net volume-integrated kinetic energy flux. This check

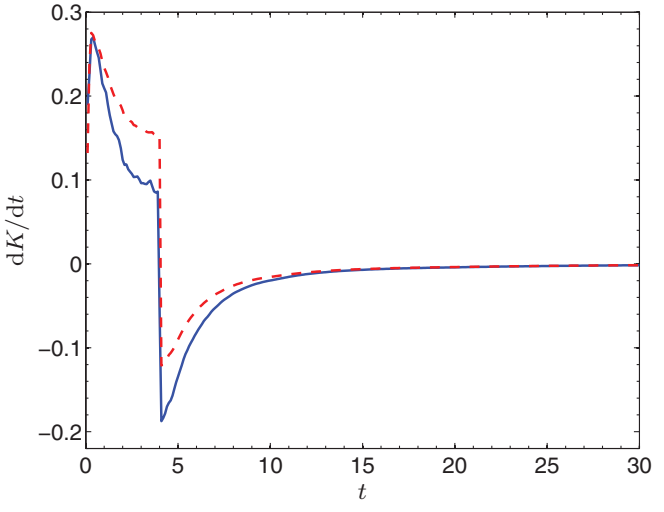

Figure 5. History of rate of change of volume-integrated kinetic energy K for Case JD (jet in deep layer): ——— $\mathrm{d}K/\mathrm{d}t$, - - - - $-\epsilon_K - F_K + \int u_i T_i \,\mathrm{d}x\,\mathrm{d}y\,\mathrm{d}z$.

indicates whether the grid is fine enough to resolve the smallest turbulence scales. History of the rate of change in the volume-integrated kinetic energy is provided in Figure 5. Although the small-scale shear layers (associated with, e.g., the boundary layer on the virtual body) generated by the jet impulse are not well captured before $t \approx 10$, after this time, the flow is fully resolved. For all seven cases in this section, the maximum difference after 10 time units was less than 1.53% of the maximum value of $\mathrm{d}K/\mathrm{d}t$. The early under-resolution (when the calculation was effectively a large-eddy simulation) corresponds to ambiguity of the details of the geometry of the wake-generating body. Since it appears that a vortex dipole is universal, i.e., a self-similar dipole can be obtained naturally from different initial conditions and paths (see Figure 11), a full resolution of the early-time small-scale turbulence is not necessary to obtain the correct long-time behaviour of the dipole.

The development of an impulsive jet in deep and shallow layers is shown in Figure 6 by the second invariant of the velocity gradient tensor $Q = -(u_{i,j}u_{j,i})/2$ (for details, see [18]). After the relatively strong jet ($Re_j \gg 1$) is imparted into the fluid, it generates a vortical structure with azimuthal vorticity in the frontal region. The frontal region propagates away from its origin with speed U_d, which is half the local fluid velocity behind the front [19]. Thus, the jet fluid merges into the vorticity front. At this stage, the ambient fluid is entrained in the frontal region, resulting in increasing the sizes of the coherent structure. When the vertical growth of the turbulent blob is not restricted (as for Case JD), the vertical and horizontal sizes of the blob increase, while decreasing the propagation speed to conserve momentum. With time, the turbulent blob transforms into a toroidal vortex, as shown in Figure 6(e).

When the vertical growth of the turbulent blob is suppressed by the stress-free layers (Case JS1), the frontal region can only expand horizontally due to lateral entrainment (Figure 6(d)). A quasi-2D counter-rotating vortical structure eventually forms at late times, as illustrated in Figure 6(f). A plot of the lateral and vertical vortex sizes (ℓ_y, ℓ_z) versus time for Cases JD and JS1 is displayed in Figure 7. The agreement of the ℓ_y and ℓ_z histories for Case JD underlines the axisymmetric nature of the turbulent blob observed in Figures 6(a), 6(c) and 6(e), throughout the simulation (and indirectly validates the choices made for

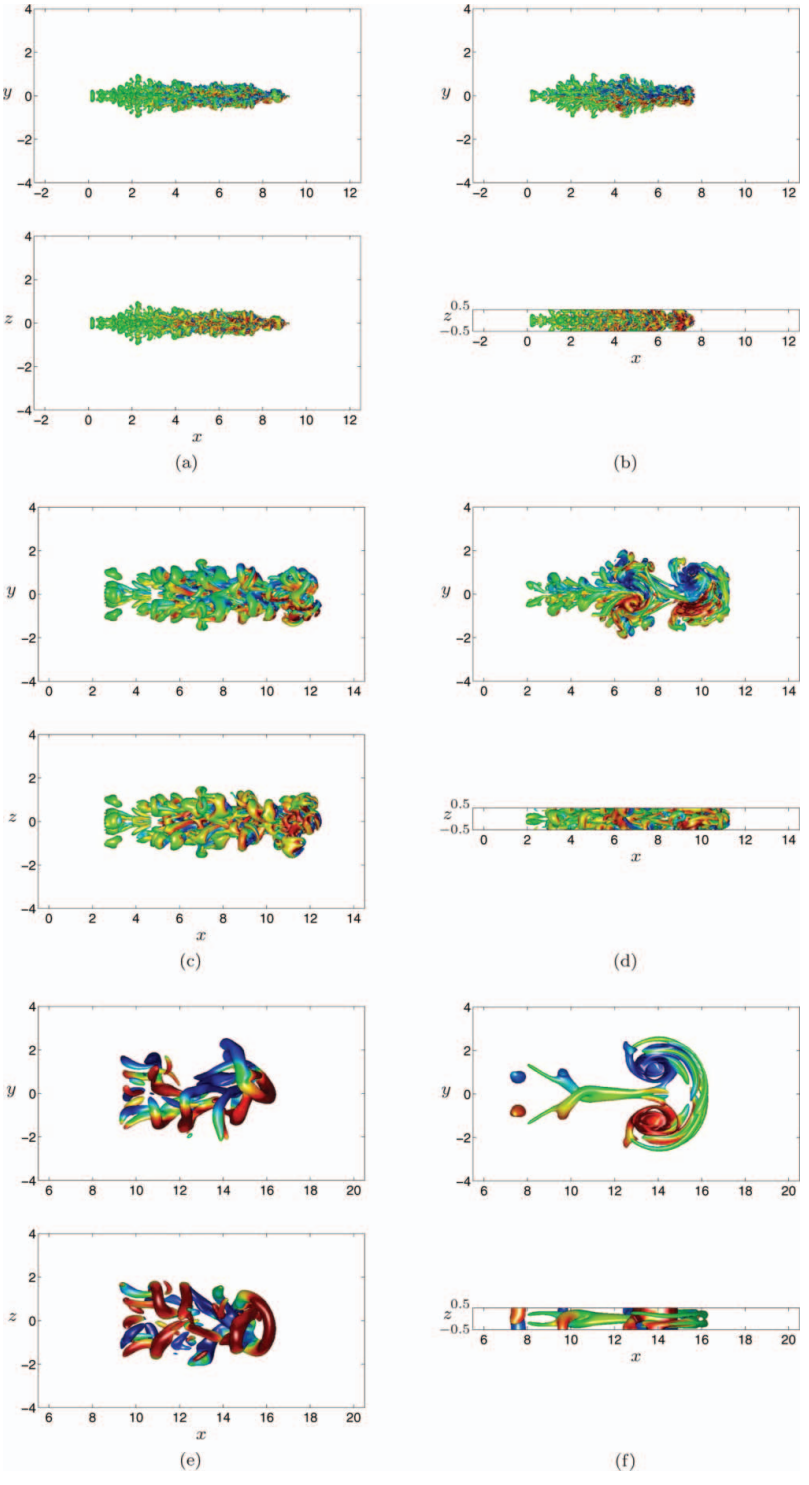

Figure 6. Top and side views (upper and lower part of each picture, respectively) of the vortical structure in (left) a deep layer (Case JD) and (right) a shallow layer (Case JS1) at $Re_j = 2000$ with level $Q = 2.5 \times 10^{-4}$: (a, b) $t = 10$, (c, d) $t = 50$, (e, f) $t = 250$. Isosurfaces of Q are coloured by vertical vorticity componemt ω_z.

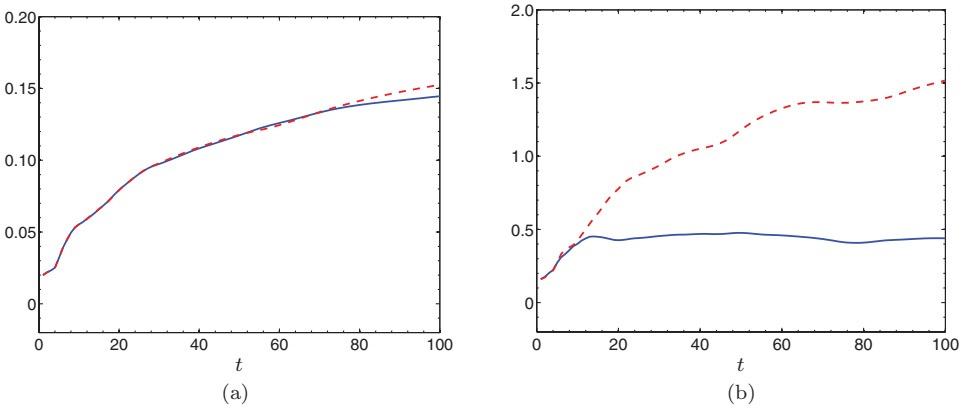

Figure 7. Histories of the lateral (ℓ_y) and vertical (ℓ_z) vortex sizes normalised by the domain depth for impulsive-jet flow in (a) a deep layer (Case JD) and (b) a shallow layer (Case JS1): - - - - ℓ_y/h, —— ℓ_z/h.

the sizes [and boundary condition] for the vertical and lateral domain). For Case JS1, the ℓ_y and ℓ_z histories imply that the turbulent blob is affected by the free-surface confinement for $t > 10$ (see Figures 6(b), 6(d), and 6(f)).

The volume-integrated kinetic energy K of both cases is displayed in Figure 8. The kinetic energy of the vortical structure resulting from the jet in a deep layer decreases faster than the vortex suppressed by a free surface. This suggests that the toroidal vortex decays more rapidly than the vortex dipole, which can be confirmed by the theoretical scaling laws. Based on the ring and the dipole power laws, the volume-integrated kinetic energy of the ring and the dipole decreases with time as $t^{-3/4}$ and $t^{-2/3}$, respectively. Note that most of the kinetic energy of the flow is provided by the large-scale structures; hence, the

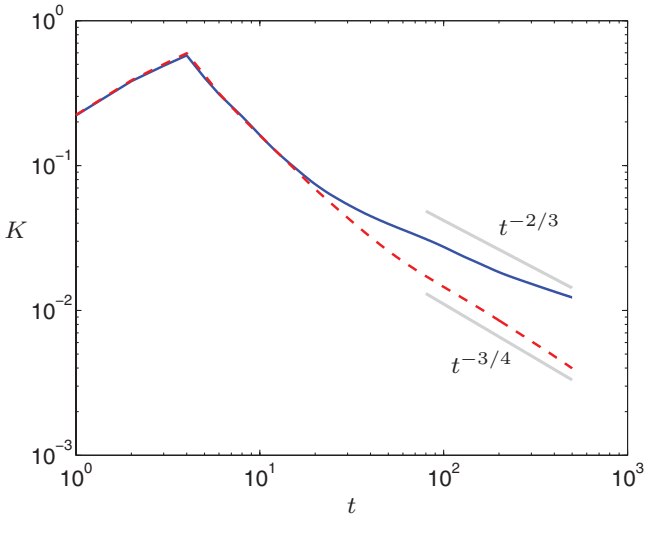

Figure 8. History of the volume-integrated kinetic energy K: - - - - Case JD (deep layer), —— Case JS1 (shallow layer).

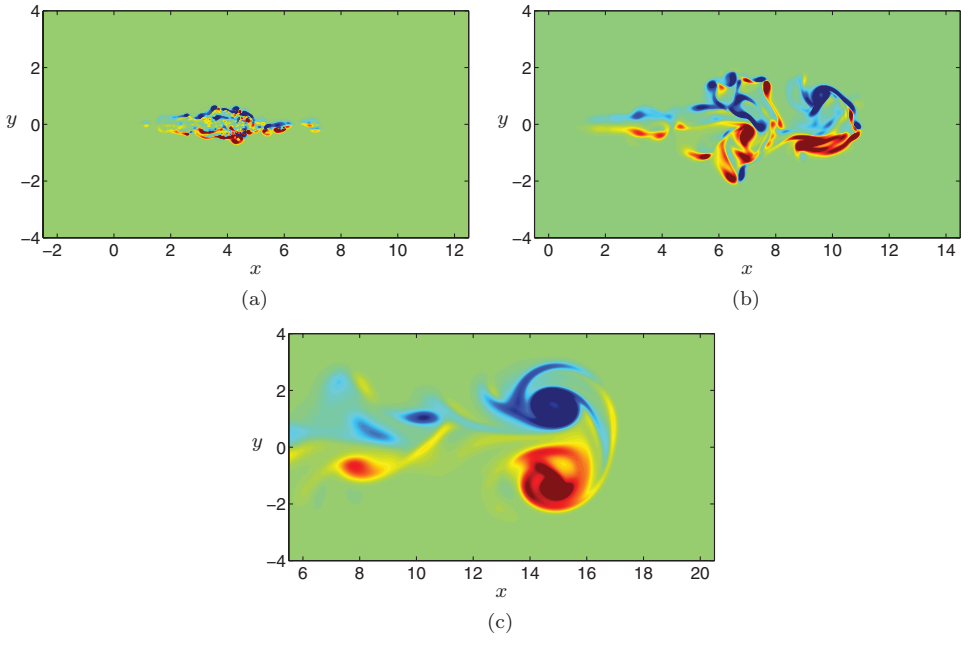

Figure 9. Contours of the vorticity at the free surface showing the penetration of the momentum source created by an impulsive jet at $Re_j = 2000$ (Case JS1): (a) $t = 10$, (b) $t = 50$, (c) $t = 300$. Vorticity varies from $-0.2 \leq \omega_z/|\omega_z|_{\max} \leq 0.2$. Blue and red patches show negative and positive vertical vorticity, respectively.

small scales observed from the ring at $t = 250$ (Figure 6(e)) do not have much effect on the kinetic energy.

Figure 9 illustrates the signature of the momentum disturbance caused by an impulsive jet. Initially, it can be seen from Figure 9(a) that the concentrated momentum disturbance at the free surface does not form a vortex dipole. With time, the blob propagates away from its origin, while increasing its horizontal size and decreasing its propagation speed, transforming into a quasi-planar dipole, as displayed in Figure 9(c). This is consistent with Voropayev et al.'s [4] prediction that a dipole will be visible on the free surface when the confinement number (which for Case JS1 is 2) is greater than 2.2.

To study the self-similar behaviour of the dipole at late time, the simulation at $Re_j = 2000$ was re-computed in a longer streamwise domain to avoid any effect of the outflow boundary condition. The length of the streamwise domain was increased from $L_x = 30$ to $L_x = 60$, with a corresponding increase in the number of grid cells to $N_x = 1920$. In addition, two more Reynolds numbers ($Re_j = 625$ and 1250) were considered (see Table 1). After the dipole is fully formed, Figure 10(a) shows that the intensity of the vertical vorticity at the free surface reduces with time as $\omega_{z,\max} \sim t^{-1}$. The temporal evolution of the dipole propagation velocity U_d and the dipole size δ_d are illustrated in Figures 10(b) and 10(c), respectively. The dipole propagation speed decreases with time as $U_d \sim t^{-2/3}$, while its size increases as $\delta_d \sim t^{1/3}$. The power laws of the dipole in this simulation are the same as those in the previous measurements in a linearly stratified fluid [7] and in a shallow layer [3, 4]. The dipole at a lower Reynolds number requires less time to achieve power-law behaviour. For example, the dipole propagation velocity at $Re_j = 625$ starts to follow $t^{-2/3}$ at $t \approx 150$, while about 500 and 1800 time units are required for the dipoles at $Re_j = 1250$ and 2000,

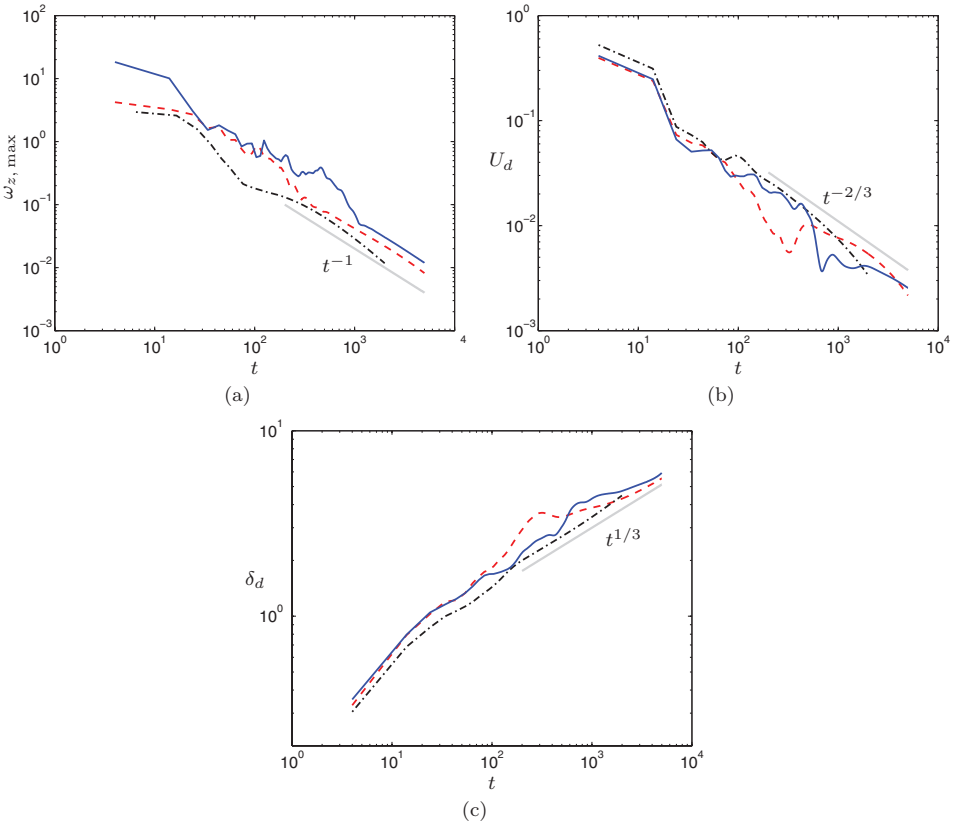

Figure 10. Histories of characteristics of jet-induced dipole: —— $Re_j = 2000$ (Case JS2), - - - - $Re_j = 1250$ (Case JS3a), -·-·- $Re_j = 625$ (Case JS4). (a) Maximum vertical vorticity at the free surface. (b) Dipole propagation velocity. (c) Dipole size.

respectively. It should be noted that the theoretical scaling laws are based on the idea of the flow similarity and they satisfactorily describe the results of experiments and our numerical simulations at intermediate asymptotic stage only – but they are not useful in describing the whole flow evolution. Additionally, using only one realisation might not be enough to obtain close agreement between DNS results and the theoretical scaling laws, especially during the transformation process leading to a dipole. An ensemble of realisations is needed to address this point.

To investigate the sensitivity of the intermediate-time behaviour (about $200 - 500$ time units; see Figure 11) to small changes in the initial conditions and domain size, Case JS3a (jet-induced dipole at $Re_j = 1250$) was repeated, first in the same computational domain but with low-amplitude (maximum value of $10^{-8}\mathcal{U}$) random seeding (Case JS3b), and again, in a two times larger lateral domain (Case JS3LD). Note that the resolution is identical for all three runs. Histories of the dipole characteristics from these three cases are illustrated in Figure 11. Although their initial development is different, all three cases nevertheless converge to very similar dipole flows. This suggests that the dipole is a robust 2D limit that is relatively insensitive to the path taken during its development.

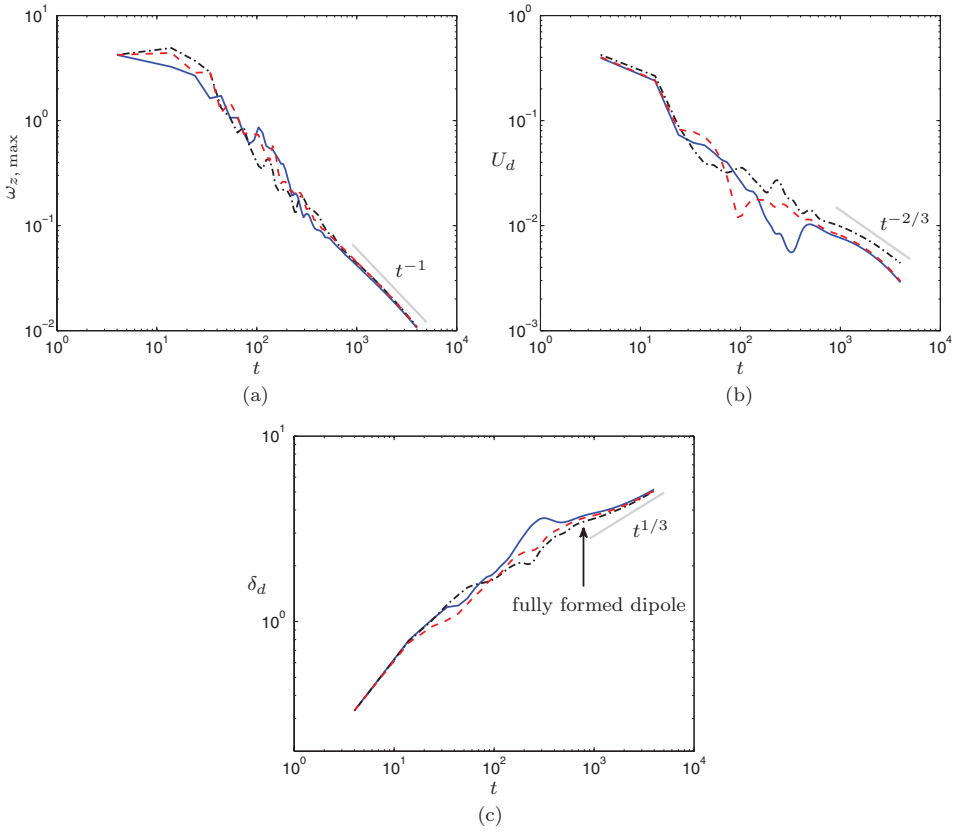

Figure 11. Histories of characteristics of jet-induced dipole at $Re_j = 1250$ from three different realisations: —— Case JS3a, - - - - Case JS3b, –·–·– Case JS3LD. (a) Maximum vertical vorticity at the free surface. (b) Dipole propagation velocity. (c) Dipole size.

5. Manoeuvring-body wake

We limit attention here to wakes in a shallow layer of same depth used for Cases JS1–JS4. In order to capture the entire process of a late wake eddy behind a manoeuvring body, the simulation of a spatially developing wake needs to be performed in a very long domain, which is computationally inefficient. To overcome the problem, the simulation is split into two phases. The first phase of the simulation is concerned with the early-time behaviour of the wake, including both the near-field and the starting vortex, while the final phase contains only the late-time dipole behaviour (see Section 5.2).

5.1. *Early-time behaviour*

We select a sphere with diameter D as the manoeuvring body. The Reynolds number based on the diameter and the terminal velocity U_t of the sphere is $Re_b = U_t D/\nu = 826$. The simulation is performed in the domain given by $-5 \le x \le 30$, $-4 \le y \le 4$ and $-0.5 \le z \le 0.5$, with $2240 \times 512 \times 64$ grid cells. Here, the reference length $\mathcal{L}$ is $2.5D$ and the reference velocity $\mathcal{U}$ is $2.05U_t$.

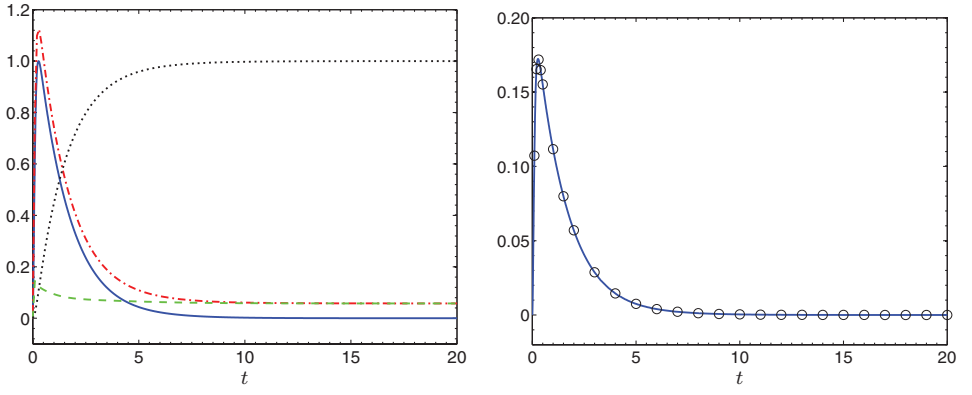

Figure 12. (a) Histories of the momentum flux, thrust, drag and speed of the body for manoeuvring-body wake: —— $F/F_{\max}$, -·-·- Thrust$/F_{\max}$, - - - - Drag$/F_{\max}$, ····· U/U_t. (b) History of the volume-integrated streamwise momentum flux: —— F_M, ○ $\int(-\partial u/\partial t + B_x + T_x - \mathrm{d}U/\mathrm{d}t)\,\mathrm{d}x\,\mathrm{d}y\,\mathrm{d}z$. The simulation parameters for this case are $Re_b = U_t D/\nu = 826$, $Re_j = J^{1/2}/\nu = 785$ and $C = J^{1/2}\Delta t_f/h^2 = 1.62$.

At $t = 0$, the body accelerates from rest. The forcing time scale in Equation (5) was chosen such that the density of the object associated with M_{eff} is 552 times that of the fluid. (Smaller values, corresponding to more physically relevant bodies, will be considered in the future.) At this stage, the thrust is greater than the drag, leading to a momentum flux F being transported to the fluid. After some time, the body reaches and maintains its terminal speed. Histories of the momentum flux, the thrust, the drag and the velocity of the body are displayed in Figure 12(a). The jet Reynolds number Re_j and the confinement number C for this case are 785 and 1.62, respectively. Note that we do not fully resolve the boundary layers of the sphere because we assume that the dipole will eventually become self-similar, such that the late-time characteristics of the dipole do not depend critically on the near-field wake (supported by the evidence in Figure 11) and only a momentum flux imparted into the fluid is important (compare comments following Equation (12)). Thus, it is necessary to check if the net volume-integrated momentum flux F_M, which is the difference between the momentum, pressure and viscous fluxes at the inlet and outlet planes, is balanced by the forces added to the Navier–Stokes equations. The streamwise momentum balance in the non-inertial moving reference frame can be written such that

$$F_M = \int \left(-\frac{\partial u}{\partial t} + B_x + T_x - \frac{\mathrm{d}U}{\mathrm{d}t} \right) \mathrm{d}x\,\mathrm{d}y\,\mathrm{d}z\,. \tag{13}$$

A plot of the balance of the volume-integrated streamwise momentum flux versus time is displayed in Figure 12(b), showing good agreement between the flux terms F_M and the external force. The difference is less than 0.11% of the maximum value of F_M during the acceleration period ($t < 9$), and less than 2×10^{-3}% when the body moves at its terminal speed. The adequacy of the spatial resolution was also checked in the same way as described in Section 4. It was found that the error remaining after five time units was lower than 0.12% of the maximum value of $\mathrm{d}K/\mathrm{d}t$.

The second invariant of the velocity gradient tensor Q is again used to visualise the vortical structure of the manoeuvring-body wake, as displayed in Figure 13. It is found

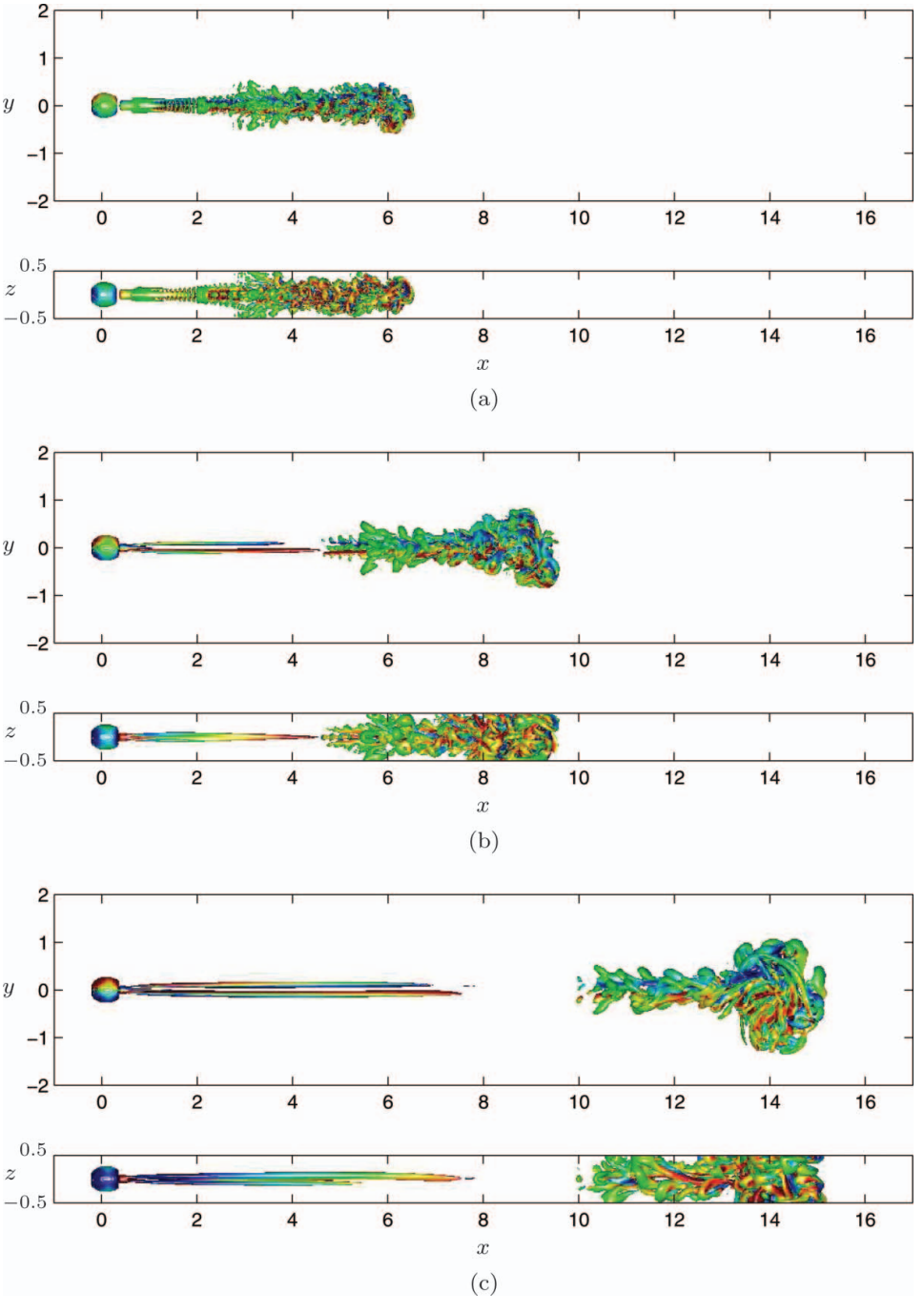

Figure 13. Top and side views (upper and lower part of each picture, respectively) of the vortical structure of a manoeuvring-body wake with level $Q = 2.5 \times 10^{-4}$: (a) $t = 5$, (b) $t = 10$, (c) $t = 20$. Isosurfaces of Q are coloured by vertical vorticity componemt ω_z.

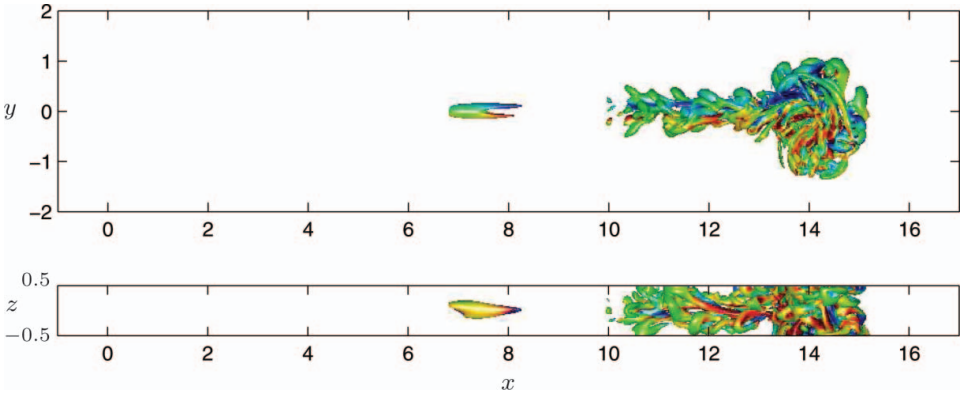

Figure 14. The projected vortical structure with the window function at $t = 20$: (upper) top view, (lower) side view.

that a large-scale vortical structure, resulting from the acceleration of the body, appears in the late wake. The horizontal size of this vortical structure increases with time, due to lateral entrainment, while the vertical growth is restricted by the top and bottom free-slip walls. When the body is moving at its terminal velocity, a momentumless wake is observed in the near-field region. The zero-momentum wake decays very quickly without the formation of any coherent vortical structures. Note that the momentumless wake at the early time is still laminar, despite the relatively high Reynolds number, because the near-field wake is *convectively* unstable, i.e. has no strong reversed-flow region. Hence, this flow compares to that over a streamlined body in which no flow separation occurs, and it thus needs a very long time to become turbulent. If we were to use a high-intensity body force (i.e. $J_D/0.5\pi\sigma^2 U_t > 1$) to represent the drag instead of the virtual body, the instability of the near-field wake would change to an absolute-type instability and would thus quickly break down to turbulence with a lot of small-scale eddies, which require very fine grid resolutions to fully resolve them. We did not follow that strategy, since the objective of this work is to study the characteristics of the late-wake eddy.

5.2. *Late-time behaviour*

After the body has reached its terminal velocity (at $t = 20$), the vorticity field was projected to a smaller computation domain using a streamwise windowing function f_w, defined as

$$f_w(x) = 0.5 \times (\tanh(1.5x - 10) + 1). \tag{14}$$

The objective of using the window function is to remove a portion of the near-field wake illustrated in Figure 14, allowing computational resources to capture only the far-field wake portion of the flow. Note that the removal of the momentum source does not affect the formation and evolution of the late-wake eddy because negligible net momentum is imparted into the flow by the self-propelled body after it has achieved its terminal speed, when the drag is practically cancelled by the thrust. In order to obtain the new velocity field, we first solve the Poisson equation for the vector stream function $\boldsymbol{\psi} = (\psi_x, \psi_y, \psi_z)$

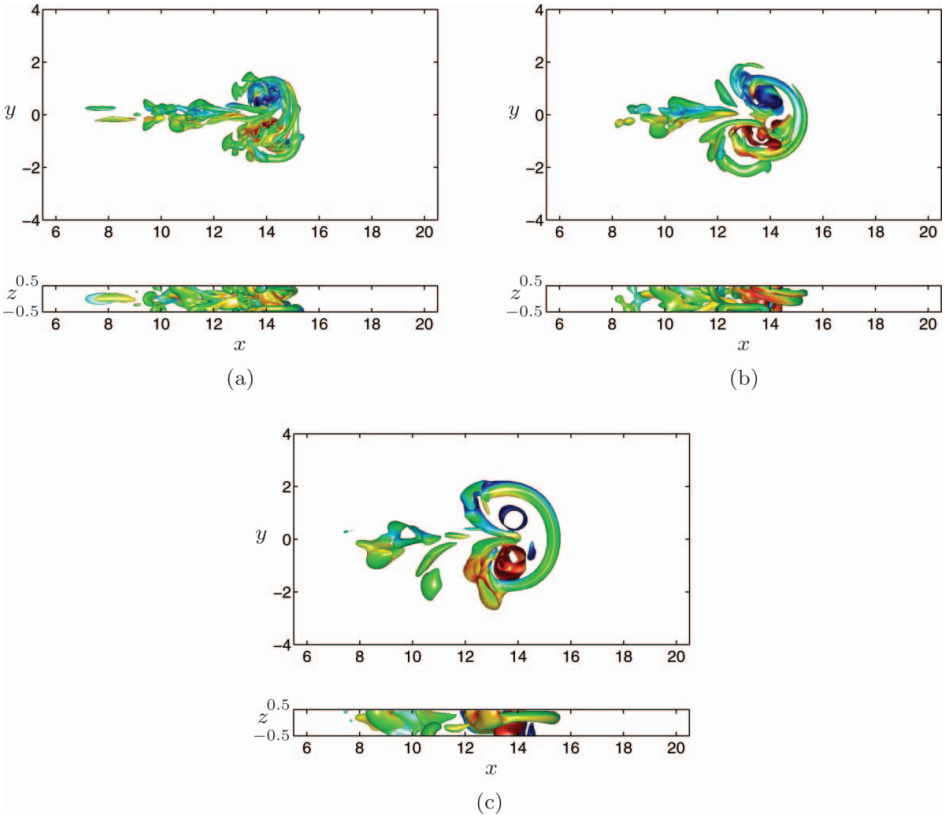

Figure 15. Top (upper) and side (lower) views of isosurfaces of Q showing the evolution of the vortical structure generated by the manoeuvring body at late time: (a) $t = 50$, (b) $t = 100$, (c) $t = 200$. Isosurfaces of Q are coloured by ω_z and the surface level is $Q = 2.5 \times 10^{-6}$.

whose source term is the projected vorticity field $\boldsymbol{\omega} = (\omega_x, \omega_y, \omega_z)$,

$$\nabla^2 \boldsymbol{\psi} = -\boldsymbol{\omega}\,. \tag{15}$$

The new velocity field can then be obtained directly by taking the curl of the vector stream function as

$$\mathbf{u} = \nabla \times \boldsymbol{\psi}\,. \tag{16}$$

The simulation in this phase is first carried out in a domain of size $4 \leq x \leq 24$, $-8 \leq y \leq 8$ and $-0.5 \leq z \leq 0.5$, with $1280 \times 1024 \times 64$ grid cells. Since the coherent structure propagates in the positive x-direction and could leave the domain if the domain length in that direction is not long enough, we employ a PID (proportional–integral–derivative) controller, described in Archer et al. [20], to keep the vortical structure at a fixed streamwise location within the domain. This also significantly reduces the computational cost. The PID controller locates the vortex dipole to within 10^{-4} of the desired location by 20 time units. We allow the wake shed from the vortex to go out of the computational domain

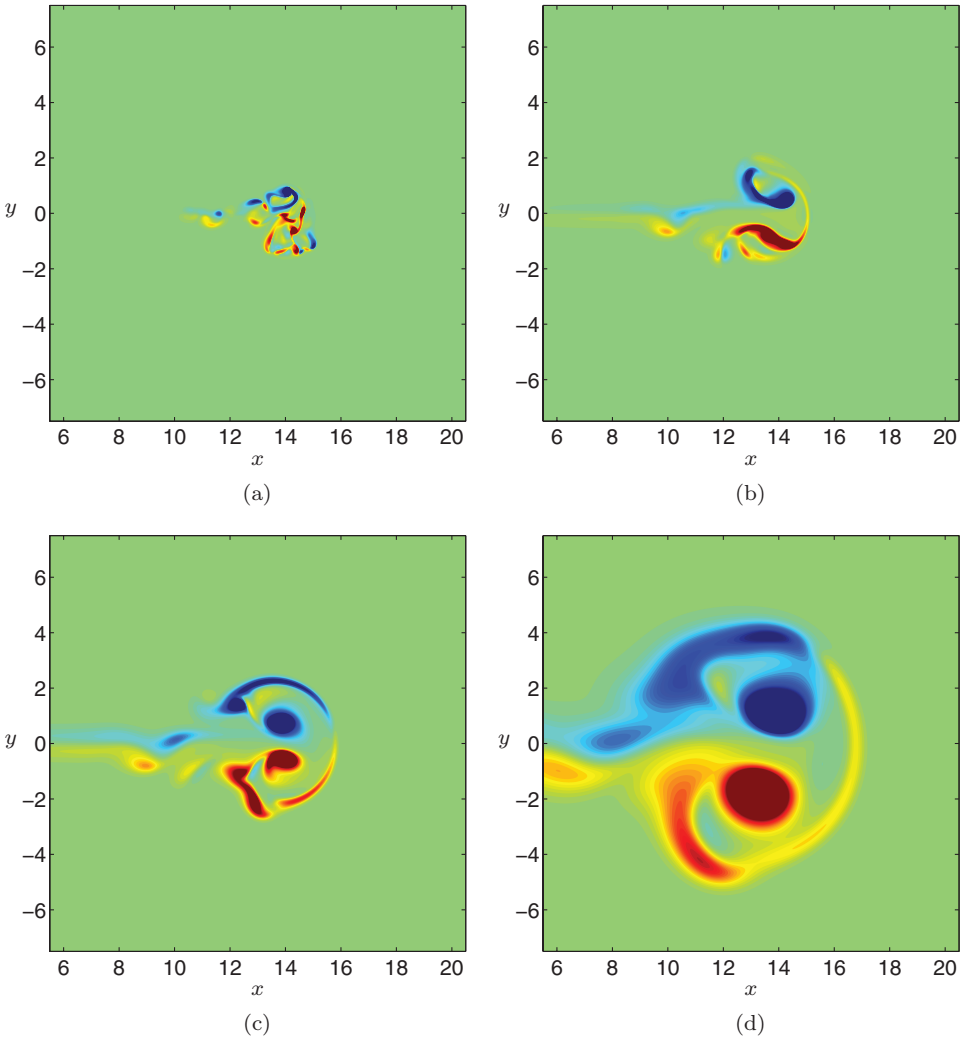

Figure 16. Contours of vorticity at free surface showing the penetration of wake signature of a manoeuvring self-propelled body: (a) $t = 30$, (b) $t = 100$, (c) $t = 200$ (the computational domain is regridded as described in Section 5.2), (d) $t = 1000$. Vorticity varies from $-0.2 \leq \omega_z/|\omega_z|_{\max} \leq 0.2$. Blue and red patches show negative and positive vertical vorticity, respectively.

in the negative (outflow) x-direction (note that in the frame of reference attached to the vortex/dipole structure, the inflow boundary is at $x = 24$ and the outflow at $x = 4$), since its effect on the dipole dynamics is assumed to be negligible. At very late time, high resolution is no longer required, since the global Reynolds number, based on the dipole translation speed U_d and the dipole size δ_d, decreases as $t^{-1/3}$ [5], but the size of the domain has to be increased to capture the dipole as its lateral size increases. Thus, the computational domain was expanded at $t = 200$, with $-2 \leq x \leq 30$, $-16 \leq y \leq 16$ and $-0.5 \leq z \leq 0.5$, and the resolution reduced to $1024 \times 1024 \times 32$ grid cells. Note that during the entire simulation, the lateral domain width L_y is at least six times larger than the lateral size of the coherent structure created by the manoeuvring body.

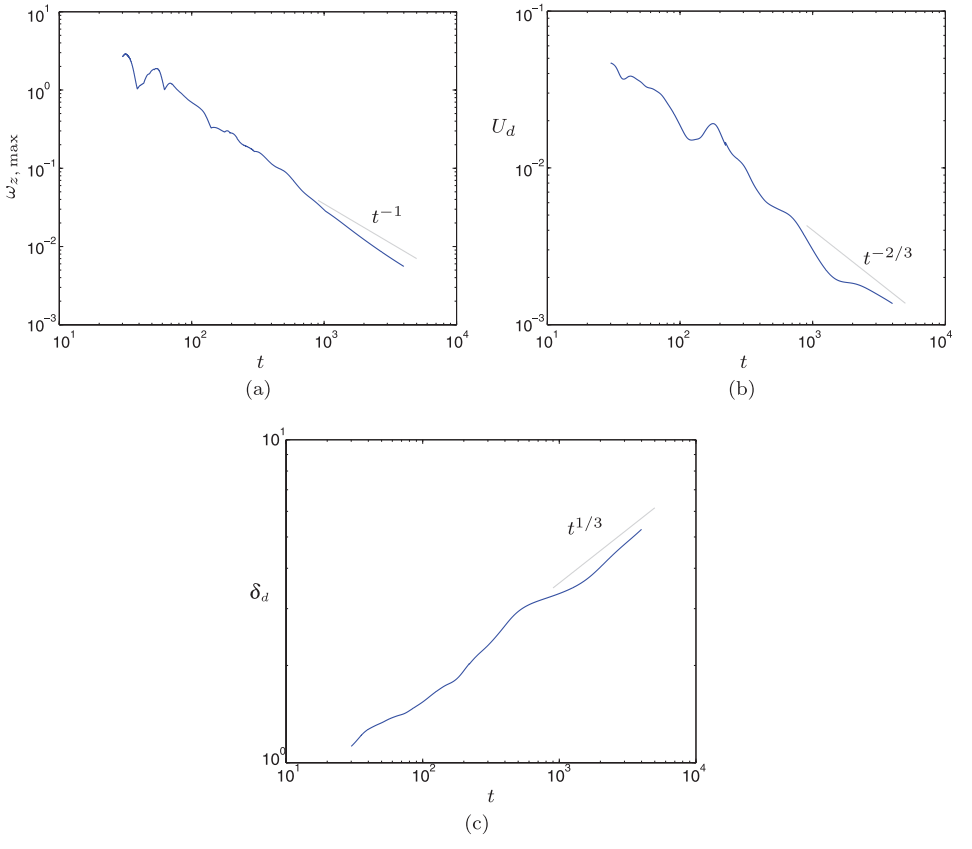

Figure 17. Histories of characteristics of dipole induced by manoeuvring body. (a) Maximum vertical vorticity at the free surface. (b) Dipole propagation velocity. (c) Dipole size. The computational domain is regridded as described in Section 5.2 at $t = 200$.

The isosurfaces of Q displayed in Figure 15 show the evolution of the vortical structure. Only the horizontal size of the late-wake eddy can expand, yielding a coherent structure in the form of two patches of opposite-signed vortices, as shown in Figure 15(c). The evolution of the vortical structure at the free surface is displayed in Figure 16. Figure 16(a) shows that the momentum disturbance penetrates upward and produces its signature at the free surface at an early time. At this stage, the wake signature is not yet in the form of a dipole. With time, the horizontal eddy grows as it propagates away from the body, and the wake

Table 2. Values of A.

Case	Re_j	C	A
JS2	2000	2.0	58.69
JS3a	1250	2.0	41.52
JS4	625	2.0	23.53
Manoeuvring body	785	1.62	21.28

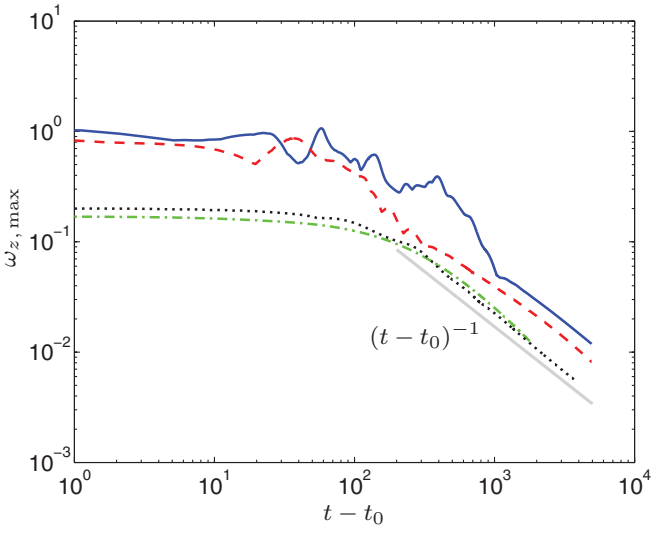

Figure 18. Histories of maximum vertical vorticity at the free surface: —— Case JS2 ($Re_j = 2000$), - - - - Case JS3a ($Re_j = 1250$), -·-·- Case JS4 ($Re_j = 625$), ····· Manoeuvring body ($Re_j = 785$).

signature finally transforms into a vortex dipole (Figures 16(c) and 16(d)). The late-time coherent eddy generated by the manoeuvring body is similar to the jet-induced dipole.

The late-time characteristics of the dipole created by the accelerating motion of the body are given in Figure 17, along with the theoretical scaling laws. The comparison shows good agreement between the DNS and the power laws. These scaling laws are obtained with the assumption that the impulse of the dipole is conserved [7, 21]. Based on this assumption, the decay of the vertical vorticity is inversely proportional to time, with

$$\omega_{z,\,\max} = At^{-1}\,, \tag{17}$$

where A is an empirical constant. The constant A was determined experimentally by Voropayev et al. [21] to be $A = 17$. In order to check whether or not this constant is universal, we compute A for all four cases (the jet-induced dipole at $Re_j = 625, 1250, 2000$ and the manoeuvring-body wake at $Re_j = 785$) by finding the slope and the virtual origin of $\omega_{z,\,\max}^{-1} = (t - t_0)/A$. The resulting values of A from our data are given in Table 2, and a plot of $\omega_{z,\,\max}$ versus $(t - t_0)$ is displayed in Figure 18. Although the vorticity at large times decays in a similar manner as $1/(t - t_0)$, a Reynolds number dependence is indicated, calling the universality of A into question. The consistency of the estimates for A seen in Figure 11(a), which shows the decay of $\omega_{z,\,\max}$ from different realisations, yields a unique value of A for the jet-induced dipole at $Re_j = 1250$. Note that some difference between numerical and experimental values of A may be expected because experiments were conducted in a stratified fluid, while a confined homogeneous fluid is used in the present simulations.

6. Summary

The formation and evolution of the large-scale coherent structure produced by both an impulsive jet and an accelerating self-propelled body have been examined using DNS. It is found that when the vortex is constrained by the stress-free top and bottom layers, a quasi-planar counter-rotating structure is formed. The vortex dipole persists for a longer time than a typical toroidal vortex. The characteristics of the dipole vortices induced due to vertical confinement are similar to those in a stratified fluid. Qualitatively similar pancake-like vortices can be obtained via different initialisations, which support the assumptions made about the self-similarity of a dipole. The expected scaling laws are satisfied, although the dipoles appear to possess a Reynolds number dependence. Future work will investigate how the formation of the submerged momentum disturbances is affected by the thickness of the fluid domain. The ability of the confinement number to predict the effect of a submerged coherent vortex on, e.g., the free surface will also be explored.

Acknowledgements

The authors gratefully acknowledge Prof. Sergey Voropayev for his invaluable comments and suggestions. This work was funded by the UK Engineering and Physical Sciences Research Council (EPSRC) (grant EP/G05035X), as part of the UK Turbulence Consortium (grant EP/G069581/1). The simulations were run on the University of Southampton Iridis 3 cluster and HECToR, the UK's national high-performance computing service, which is provided by UoE HPCx Ltd at the University of Edinburgh, Cray Inc. and NAG Ltd, and funded by the Office of Science and Technology through EPSRC's High End Computing programme.

References

[1] H. Tennekes and J.L. Lumley, *A First Course in Turbulence*, MIT Press, Cambridge, MA, 1972.
[2] K. Ahlnäs, T.C. Royer, and T.H. George, *Multiple dipole eddies in the Alaska coastal current detected with Landsat thematic mapper data*, J. Geophys. Res. 92 (1987), pp. 13041–13047.
[3] D. Sous, N. Bonneton, and J. Sommeria, *Turbulent vortex dipoles in a shallow water layer*, Phys. Fluids 16 (2004), pp. 2886–2898.
[4] S.I. Voropayev, H.J.S. Fernando, S.A. Smirnov, and R. Morrison, *On surface signatures generated by submerged momentum sources*, Phys. Fluids 19 (2007), 076603.
[5] S.I. Voropayev, G.B. McEachern, H.J.S. Fernando, and D.L. Boyer, *Large vortex structures behind a maneuvering body in stratified fluids*, Phys. Fluids 11 (1999), pp. 1682–1684.
[6] T. Maxworthy, *Some experimental studies of vortex rings*, J. Fluid Mech. 81 (1977), pp. 465–495.
[7] S.I. Voropayev, Y.D. Afanasyev, and I.A. Filippov, *Horizontal jets and vortex dipoles in a stratified fluid*, J. Fluid Mech. 227 (1991), pp. 543–566.
[8] J.B. Flór and G.J.F. van Heijst, *An experimental study of dipolar vortex structures in a stratified fluid*, J. Fluid Mech. 279 (1994), pp. 101–133.
[9] J.B. Flór, G.J.F. van Heijst, and R. Delfos, *Decay of dipolar vortex structures in a stratified fluid*, Phys. Fluids 7 (1995), pp. 374–383.
[10] D. Sous, N. Bonneton, and J. Sommeria, *Transition from deep to shallow water layer: Formation of vortex dipoles*, Eur. J. Mech. B-Fluids 24 (2005), pp. 19–32.
[11] R.A.D. Akkermans, A.R. Cieslik, L.P.J. Kamp, R.R. Trieling, H.J.H. Clercx, and G.J.F. van Heijst, *The three-dimensional structure of an electromagnetically generated dipolar vortex in a shallow fluid layer*, Phys. Fluids 20 (2008), 116601.
[12] T.G. Thomas and J.J.R. Williams, *Development of a parallel code to simulate skewed flow over a bluff body*, J. Wind Eng. Ind. Aerodyn. 67–68 (1997), pp. 155–167.
[13] A.M. Roma, C.S. Peskin, and M.J. Berger, *An adaptive version of the immersed boundary method*, J. Comput. Phys. 153 (1999), pp. 509–534.
[14] Y.D. Afanasyev, *Wakes behind towed and self-propelled bodies: Asymptotic theory*, Phys. Fluids 16 (2004), pp. 3235–3238.

[15] Y.D. Afanasyev and V.N. Korabel, *Wakes and vortex streets generated by translating force and force doublet: Laboratory experiments*, J. Fluid Mech. 553 (2006), pp. 119–141.
[16] P.G. Saffman, *The velocity of viscous vortex rings*, Stud. Appl. Math. 49 (1970), pp. 371–380.
[17] P.G. Saffman, *Vortex Dynamics*, Cambridge University Press, Cambridge, 1995.
[18] J. Jeong and F. Hussain, *On the identification of a vortex*, J. Fluid Mech. 285 (1995), pp. 69–94.
[19] M.E. Stern and S.I. Voropayev, *Formation of vorticity fronts in shear flow*, Phys. Fluids 27 (1984), pp. 848–855.
[20] P.J. Archer, T.G. Thomas, and G.N. Coleman, *Direct numerical simulation of vortex ring evolution from the laminar to the early turbulent regime*, J. Fluid Mech. 598 (2008), pp. 201–226.
[21] S.I. Voropayev, H.J.S. Fernando, and R. Morrison, *Dipolar eddies in a decaying stratified turbulent flow*, Phys. Fluids 20 (2008), 026602.